REPORT DOCUMENTATION PAGE

Form Approved
OMB No. 0704-0188

Public reporting burden for this collection of information is estimated to average 1 hour per response, including the time for reviewing instructions, searching existing data sources, gathering and maintaining the data needed, and completing and reviewing the collection of information. Send comments regarding this burden estimate or any other aspect of this collection of information, including suggestions for reducing this burden, to Washington Headquarters Services, Directorate for Information Operations and Reports, 1215 Jefferson Davis Highway, Suite 1204, Arlington, VA 22202-4302, and to the Office of Management and Budget, Paperwork Reduction Project (0704-0188), Washington, DC 20503.

AD-A275 384

1. AGENCY USE ONLY *(Leave blank)*

2. REPORT DATE 12-30-93

3. REPORT TYPE AND DATES COVERED Final 10/1/90 - 10/14/93

4. TITLE AND SUBTITLE
Focused Ion Beam Fabrication of Microelectronic Structures

5. FUNDING NUMBERS
DAAL03-90-G-0223

DTIC ELECTE FEB 9 1994 S C D

6. AUTHOR(S)
Dr. John Melngailis

7. PERFORMING ORGANIZATION NAME(S) AND ADDRESS(ES)
Research Laboratory of Electronics
Massachusetts Institute of Technology
77 Massachusetts Avenue
Cambridge, MA 02139

8. PERFORMING ORGANIZATION REPORT NUMBER

94-04290

9. SPONSORING/MONITORING AGENCY NAME(S) AND ADDRESS(ES)
U.S. Army Research Office
P.O. Box 12211
Research Triangle Park, NC 27709-2211

10. SPONSORING/MONITORING AGENCY REPORT NUMBER
ARO 28345.5-EL

11. SUPPLEMENTARY NOTES
The view, opinions and/or findings contained in this report are those of the author(s) and should not be construed as an official Department of the Army position, policy, or decision, unless so designated by other documentation.

12a. DISTRIBUTION/AVAILABILITY STATEMENT
Approved for public release; distribution unlimited.

12b. DISTRIBUTION CODE

13. ABSTRACT *(Maximum 200 words)*

One of the most successful applications of focused ion beams has been the deposition of submicrometer conductors for integrated circuits. Our work has concentrated on demonstrating new materials and on studying the fundamental mechanisms of the deposition and milling processes. One of the important results has been the first demonstration of ion induced copper deposition from a new precursor gas. Copper is being considered a successor to aluminum in integrated circuits, and our copper had the lowest resistivity (50 micro ohm cm) of any material produced by room temperature focused ion beam deposition. We have also studied the ion induced deposition of gold and tungsten as a function of angle of incidence as well as the milling of Si, SiO_2, W, and Au. These processes are also important for the repair of lithography masks. A Monte Carlo model based on collision cascades has been developed for the fundamental mechanism for ion induced deposition and tested against measurements of deposition yield of Au for various ion energies and noble gas ion species. The deposition appears to be substrate mediated and fits the collision cascade model. The dependence of milling and deposition as a function of ion incidence also appears to fit this model.

94 2 08 018

14. SUBJECT TERMS

15. NUMBER OF PAGES

16. PRICE CODE

17. SECURITY CLASSIFICATION OF REPORT	18. SECURITY CLASSIFICATION OF THIS PAGE	19. SECURITY CLASSIFICATION OF ABSTRACT	20. LIMITATION OF ABSTRACT
UNCLASSIFIED	UNCLASSIFIED	UNCLASSIFIED	UL

NSN 7540-01-280-5500

Standard Form 298 (Rev. 2-89)
Prescribed by ANSI Std Z39-18
298-102

Best
Available
Copy

GENERAL INSTRUCTIONS FOR COMPLETING SF 298

The Report Documentation Page (RDP) is used in announcing and cataloging reports. It is important that this information be consistent with the rest of the report, particularly the cover and title page. Instructions for filling in each block of the form follow. It is important to *stay within the lines* to meet *optical scanning requirements*.

Block 1. Agency Use Only *(Leave blank)*.

Block 2. Report Date. Full publication date including day, month, and year, if available (e.g. 1 Jan 88). Must cite at least the year.

Block 3. Type of Report and Dates Covered. State whether report is interim, final, etc. If applicable, enter inclusive report dates (e.g. 10 Jun 87 - 30 Jun 88).

Block 4. Title and Subtitle. A title is taken from the part of the report that provides the most meaningful and complete information. When a report is prepared in more than one volume, repeat the primary title, add volume number, and include subtitle for the specific volume. On classified documents enter the title classification in parentheses.

Block 5. Funding Numbers. To include contract and grant numbers; may include program element number(s), project number(s), task number(s), and work unit number(s). Use the following labels:

C	- Contract	PR	- Project
G	- Grant	TA	- Task
PE	- Program Element	WU	- Work Unit Accession No.

Block 6. Author(s). Name(s) of person(s) responsible for writing the report, performing the research, or credited with the content of the report. If editor or compiler, this should follow the name(s).

Block 7. Performing Organization Name(s) and Address(es). Self-explanatory.

Block 8. Performing Organization Report Number. Enter the unique alphanumeric report number(s) assigned by the organization performing the report.

Block 9. Sponsoring/Monitoring Agency Name(s) and Address(es). Self-explanatory.

Block 10. Sponsoring/Monitoring Agency Report Number. *(If known)*

Block 11. Supplementary Notes. Enter information not included elsewhere such as: Prepared in cooperation with...; Trans. of...; To be published in.... When a report is revised, include a statement whether the new report supersedes or supplements the older report.

Block 12a. Distribution/Availability Statement. Denotes public availability or limitations. Cite any availability to the public. Enter additional limitations or special markings in all capitals (e.g. NOFORN, REL, ITAR).

DOD - See DoDD 5230.24, "Distribution Statements on Technical Documents."
DOE - See authorities.
NASA - See Handbook NHB 2200.2.
NTIS - Leave blank.

Block 12b. Distribution Code.

DOD - Leave blank.
DOE - Enter DOE distribution categories from the Standard Distribution for Unclassified Scientific and Technical Reports.
NASA - Leave blank.
NTIS - Leave blank.

Block 13. Abstract. Include a brief *(Maximum 200 words)* factual summary of the most significant information contained in the report.

Block 14. Subject Terms. Keywords or phrases identifying major subjects in the report.

Block 15. Number of Pages. Enter the total number of pages.

Block 16. Price Code. Enter appropriate price code *(NTIS only)*.

Blocks 17. - 19. Security Classifications. Self-explanatory. Enter U.S. Security Classification in accordance with U.S. Security Regulations (i.e., UNCLASSIFIED). If form contains classified information, stamp classification on the top and bottom of the page.

Block 20. Limitation of Abstract. This block must be completed to assign a limitation to the abstract. Enter either UL (unlimited) or SAR (same as report). An entry in this block is necessary if the abstract is to be limited. If blank, the abstract is assumed to be unlimited.

FINAL REPORT

Submitted To

U.S. ARMY RESEARCH OFFICE

on

"FOCUSED ION BEAM FABRICATION OF MICROELECTRONIC STRUCTURES"

by

John Melngailis
Research Laboratory of Electronics
Massachusetts Institute of Technology

(at the University of Maryland as of Oct. 1, 1993)

Contract No. DAAL 03-90-G0223

Accesion For
NTIS CRA&I
DTIC TAB
Unannounced
Justification
By
Distribution /
Availability Codes
Dist | Avail and / or Special
A-1

DTIC QUALITY INSPECTED 1

Participating Scientific Personnel:

A. D. DellaRatta MS Degree in Materials Science and Engineering MIT 1993

J. S. Ro PhD Degree in Materials Science and Engineering MIT 1991

X. Xu Post Doctoral Associate

C. V. Thompson Professor, Materials Science and Engineering

J. Melngailis, Senior Research Scientist MIT (as of 10/93 Professor of Electrical Engineering University of Maryland)

Publications

A. D. DellaRatta, J. Melngailis, and C. V. Thompson "Focused Ion Induced Deposition of Copper" J. Vacuum Science and Technol. to be published Nov/Dec 1993 (Presented at International Symp. on Electron Ion and Photon Beam Technology, San Diego, May 1993)

X. Xu and J. Melngailis "Quasi-Periodic Nano Structures in Focused Ion Beam Deposited Tungsten at High Angles of Incidence"J. Vacuum Science and Technol. to be published Nov/Dec 1993 (Presented at International Symp. on Electron Ion and Photon Beam Technology, San Diego, May 1993)

X. Xu, A. D. DellaRatta, J. Sosonkina, and J. Melngailis "Focused Ion Beam Induced Deposition and Ion Milling as a Function of Angle of Ion Incidence" J. Vac. Sci. Technol. B10, 2675, (1992) (Presented at International Symposium on Electron Ion and Photon Beam Technology. Orlando,May, 1992)

J. S. Ro, C. V Thompson, and J. Melngailis "Mechanism of Ion Induced Deposition of Gold" To be published J. Vac. Sci. Technol. 1994

J. S. Ro, C. V. Thompson, and J. Melngailis "Microstructure of Gold Grown by Ion Induced Deposition" Submitted to Thin Solid Films.

J. Melngailis "Focused Ion Beam Induced Deposition- a Review" (invited paper) SPIE Symp. on Electron Beam, X-Ray, and Ion Beam Submicrometer Lithographies for Manufacturing Vol. 1465, p.36 (1991)

J. Melngailis "Materials Issues in X-Ray Mask Repair by Focused Ion Beams" Invited paper, to be published MRS Symp. Proc. "Materials Aspects of X-Ray Lithography" (Spring Meeting, San Francisco, 1993)

INTRODUCTION

The focused ion beam has become an important tool in the microelectronics industry with a number of different uses. Integrated circuits can be locally rewired or repaired by using focused ion beam milling to cut conductors and focused ion beam induced deposition from a precursor gas to deposit new conductors and make new connections. This capability is particularly important in the prototyping phase when an integrated circuit can be repaired, altered and tested without the time consuming process of fabricating a new circuit. Similarly the masks used in integrated circuit fabrication can be locally repaired by focused ion beams. This is also a procedure used regularly in the IC industry. Namely a mask is inspected by an automated process and the defective sites are located. This information is then transmitted along with the mask to the focused ion beam machine where the defects are inspected and repaired. The process has been widely used for optical lithography masks and is also being developed for x-ray lithography masks and ion lithography stencil masks. Another important area of application is integrated circuit cross sectioning for defect analysis and process diagnosis. Here trenches are locally cut into integrated circuits at specific sites to see defective circuit parts in cross section, by either scanning electron microscopy or by scanning ion microscopy directly in the cutting tool. Another potentially important application in materials science is the use of scanning ion microscopy to observe crystal grain structure in a surface. When a polycrystalline surface is imaged in the scanning ion microscope mode, then each grain will appear with a different brightness on the screen. This is due to the fact that the secondary electron yield is a strong function of the crystal symmetry axis orientation with respect to the ion beam incidence direction. Alternate materials science methods for viewing grains can be much more clummsy such as sample thinning combined with transmission in electron microscope viewing or preferential etching combined with optical microscopy. These numerous applications have led to two US companies, FEI and Micrion, to manufacture focused ion beam equipment for industrial users.

Our research at MIT (largely ARO supported) has contributed to the development of this technology. We were the first to demonstrate some of the metal deposition processes used and have developed models for the ion induced deposition process and ion milling and deposition as a function of angle of ion beam incidence. More details and background information is given in two review articles, Appendices A and B.

MAIN RESULTS OF RESEARCH

Our work on the application of focused in beams to microelectronic devices has been in four areas: developing a model for the fundamental mechanism of ion induced deposition, measuring and modeling milling and deposition as a function of angle of ion beam incidence, studying the microstructure of deposition films, and developing the deposition of copper.

A. Mechanism of Ion Beam Induced Deposition of Gold

In the process of ion induced deposition a precursor gas, such as a metal organic or a cabronyl e.g. $W(CO)_6$, adsorbs on the surface. The gas is provided by a capillary feed which creates a local ambient in the 10^{-3} Torr range while the rest of the chamber is in the 10^{-6} Torr range. An incident ion dissociates a large number of molecules, 50-100 in some cases. Since the gas is usually adsorbed as a monolayer, molecules 5-10 nm from the point of ion incidence are dissociated. What is the mechanism? Direct ion molecule collisions seem to be ruled out. To understand this process we measured the dissociation yield for dimetylgold hexafluoroacetylacetonate for a variety of noble gas ion species from He to Xe at 50 and 100 keV. The deposition is a competition between dissociation and ion milling, i.e. the net deposition yield, Y_N is the difference between the dissociation yield Y_D and the sputter yield Y_S, or $Y_N = Y_D - Y_S$. We measured Y_N and Y_S, thus determining Y_D. The dependence of Y_D on energy and ion mass does not correlate with the ion energy loss to electrons but does correlate with the ion energy loss to the substrate atom nuclei, the so called nuclear stopping power. Monte Carlo simulation of the ion collision cascades was used to calculate the energy imparted to adsorbed surface atoms per incident ion. This model correlated well with the measured results. Details are given in the Ph.D. Thesis of J.S. Ro and in Appendix C.

B. Deposition and Milling at Non-Normal Incidence

In many of the applications of focused ion beam milling and deposition complex surface topography is encountered. Thus an understanding of the processes as a function of ion beam incidence angle is needed. Accordingly we have measured the milling yield of Si, SiO_2, Au, and W as a function of angle of incidence and fitted the results with a Monte-Carlo–collision cascade model. For Si the fit is quite good while for W the fit is qualitative. In both the measurements and the theory the milling yield increases as the angle of incidence moves from normal toward grazing and drops sharply as grazing incidence is approached. This is true for all of the materials measured.

In ion induced deposition also the dissociation yield increases as the angle of incidence goes from normal toward grazing. However, as grazing incidence is approached the deposit becomes discontinuous, often consisting of a grid of periodic fin-like protrusions. We have measured the dependence of the period on beam energy and angle of incidence. The period is found to increase with angle and with beam energy but to be independent of current density. Details are given in Appendices D & E.

C. Microstructure of Ion Deposited Films

All of the metal films grown by ion induced deposition contain carbon, due to the carbon containing precursor gases used. As a result the resistivity of the films is usually 30 to 100 times higher than that of pure metal. We have previously observed that the resistivity of gold drops sharply if the substrate is above room temperature during deposition. For example above 100°C the resistivity is nearly that of pure metal. The carbon concentration decreases much more slowly and monotomically. Change in resistivity, we believe, is largely due to a change in microstructure. Therefore, using transmission electron microscopy we have examined the microstructure of gold and copper deposited under various conditions. The structure changes with deposition rate and substrate temperature during deposition. The results are summarized in Fig. 1. Room temperature, high current density deposition results in granular, high resistivity films, (i.e. grains of gold in background of carbon.) In intermediate conditions the growth becomes columnar, while at higher temperature $\sim$ 100°C and low current density the film becomes polycrystaline and of low resistivity. Preliminary results for copper indicate similiar behavior. The results are presented in more detail in Appendices F and G.

D. Ion Induced Deposition of Copper

Copper is being seriously considered in industry for integrated circuit interconnect metal as a replacement for Al. Accordingly we sought to demonstrate focused ion beam induced deposition of copper as a compatible repair process. We succeeded in doing this with the precursor gas compound, copper (+1) hexafluoroacetylacetonate trimethylvinylsilane. We obtained resistivities as low as 50 $\mu\Omega cm$. This is the lowest value reported for deposition at room temperature. As the temperature of the substrate during deposition is raised above 67°C the resistivity of the copper film drops to near the bulk value. The yield was measured to be 14 copper atoms per incident Ga^+ ion. High aspect ratio deposits were also demonstrated (linewidth of 0.25 μm and an aspect ratio of 5.4 to 1). Compared to other metals used in integrated circuit repair such as W or Pt, Cu has higher figure of merit. More details are given in Appendix G.

Thesis

J.S. Ro, "Microstructure and Mechanism of Gold Films Grown by Ion Beam Induced Deposition," Ph.D. Thesis Dept. of Materials Science and Engineering, MIT (1991).

A.D. DellaRatta, "Focused Ion Beam Induced Deposition of Copper," M.S. Thesis Dept. of Materials Science and Enginereing, MIT (1993).

"Focused ion beam induced deposition - a review"

John Melngailis

Massachusetts Institute of Technology
Cambridge, Massachusetts 02139

ABSTRACT

Focused ion beam induced deposition complements the process of material removal by focused ion beam milling. Together these two techniques are being used commercially for photomask repair and for repair or restructuring of integrated circuits and are being developed for the repair of x-ray lithography masks. This microsurgery of masks and circuits can be carried out with a precision determined by the minimum diameters of the ion beams which are now approaching 0.05 μm.

In ion induced deposition a local gas ambient in the millitorr range is created on the surface around the point of ion incidence, usually by aiming a miniature gas nozzle at the surface. Incident ions break up the gas molecules that are adsorbed on the surface. The precursor gas is usually an organometallic or a metal halide. Deposits of W, Au, Al, Cr, Ta, and Pt have been produced. Often these deposits have high concentrations of impurities, particularly carbon if organometallics are used, and sometimes also oxygen. The resistivities of the "metal" films fall in the 70-1000 μΩcm range rather than the 2.5-10 μΩcm one would expect for pure metals. Nevertheless, even at these resistivities useful conducting connections can be made for integrated circuit repair. Under special circumstances resistivities approaching the pure metal values have also been demonstrated. For x-ray mask repair high aspect ratio (e.g. 0.25 μm wide by 0.4 to 0.7 μm high) deposits of a high Z material such as Au, W or Pt are needed. We will review the considerable body of experience in this field and examine also the theoretical models of the process.

2. INTRODUCTION

Microelectronic devices are universally built from patterned thin films or patterned substrate materials. The patterning is usually produced by exposing and developing resist on the surface and then altering the surface that is exposed and not altering the surface that is protected by the resist. In this way the substrate may be implanted, oxide films may be defined, and conducting films laid down to interconnect the devices. Entire wafers or chips are treated in a single step thus permitting millions of devices to be fabricated cheaply. With the focused ion beam most of these microfabrication steps can be performed locally without the use of mask or resist. This provides unprecedented flexibility by sacrificing fabrication speed.(1) For example, transistors can be implanted, point-by-point, to produce gradients of doping or to produce transistors side-by-side which have different doping concentrations. This kind of very customized processing may be useful for device prototyping and for the fabrication of special, high performance devices in limited locations on a chip. The steps carried out by the focused ion beam can be aligned within a tolerance of ± 0.1 μm to existing structures on a wafer by using the scanning ion microscope mode to locate alignment masks. The potential applications of focused ion beams for direct implantation are being explored, and numerous devices with unique or superior characteristics have been demonstrated.(2) On the other hand the widely accepted applications of focused ion beams so far are in areas of local repair or of sectioning of integrated circuits for diagnosis.

SPIE Vol. 1465 Electron-Beam, X Ray, and Ion-Beam Submicrometer Lithographies for Manufacturing. p 36, 1991.

In the repair processes of both masks and circuits the focused ion beam is used in its micromilling mode to sputter off material with better than 0.1 μm resolution. Thus unwanted chromium (or other absorber) on a photomask can be milled off or an electrical short on an integrated circuit can be cut. In fact, because of the ability of the focused ion beams to mill deep relatively narrow trenches, these conductors can be cut even if they are covered by substantial layers of oxide. The complimentary process of material addition is also being developed and is the subject of this review.(3)

A schematic of focused ion beam induced deposition is shown in Fig. 1(a). A focused ion beam column is mounted on a vacuum chamber so that the ion beam is incident on a sample. The system configuration externally looks like a scanning electron microscope or an electron beam lithography machine. An added feature is the gas feed consisting of a fine capillary tube which is pointed at the surface where the ion beam is incident. This creates a local gas ambient in the range of 1 to 10 mTorr over an area of the surface which is usually larger than the field scanned by the ion beam, see Fig. 1(b). The sample is on an externally driven x-y stage for addressing large areas. The vacuum chamber is pumped so that the pressure away from the gas feed is typically in the 10^{-6} Torr range. Usually the ion column is pumped separately.

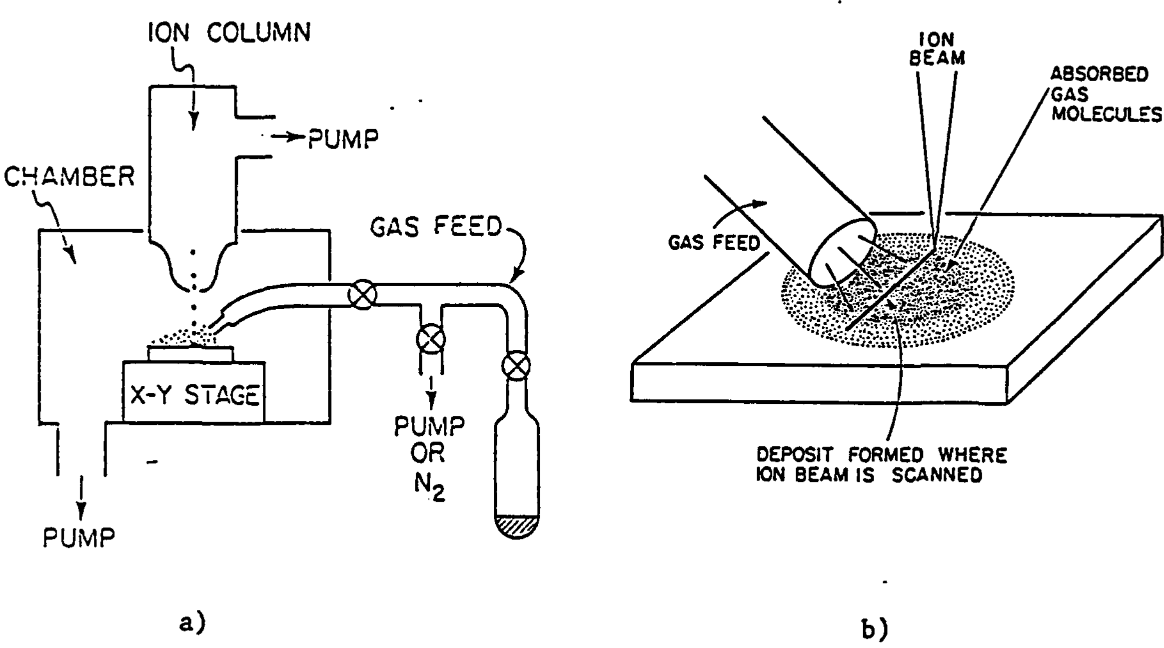

Fig. 1. a) Schematic of the apparatus used for focused ion beam induced deposition. The gas feed creates a local gas ambient on the sample area which is scanned by the ion beam. For low vapor pressure gases such as $W(CO)_6$ the entire gas feed system may need to be heated.

b) the deposition area shown schematically close-up.

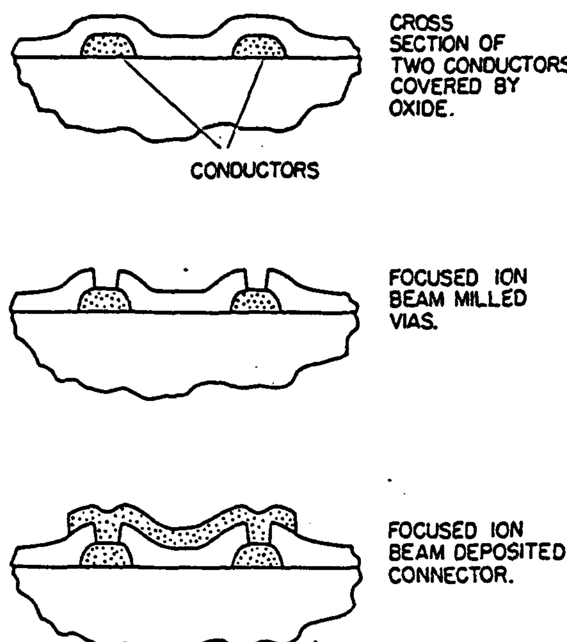

Fig. 2 Schematic of circuit repair of restructuring. Two parallel conductors shown in top sketch in cross section need to be connected electrically. Vias are first milled with the focused ion beam by scanning small rectangles over the passivation until the metal is exposed, as shown in the middle. Imaging in the scanning ion microscope mode can be used for end point detection since the secondary electron yield of the metal is usually higher than that of the passivating oxide. Finally (botton) a metal connector is made by focused ion beam induced depositon.

In ion induced deposition for photomask repair what is needed is an optically opaque film which will hold up to the cleaning and handling. Frequently carbon has been used. In the repair of integrated circuits, on the other hand, the films need to be conducting. A typical sequence for connecting two conductors is shown in Fig. 2. With the gas turned off vias are first milled through the passivation layer to the underlying conductors. Then the gas is turned on and metal is deposited to short together the conductors.(4) (5) If two intersecting but unconnected metal lines need to be connected, a via can simply be milled through the upper metal to the lower one and then filled with a metal plug.(5)

In x-ray mask repair the challenge is the deposition (and milling) of high aspect ratio structures. Masks with minimum dimensions of 0.25 μm and metal thickness in the range of 0.4 to 0.8 μm may be needed for the future generations of devices.(6)

Patterned maskless deposition of material can also be carried out with lasers(7) or with electron beams.(8-12) Laser deposition is being used, for example, for circuit modification and repair, but the submicrometer dimensions often needed in modern integrated circuits cannot be achieved. Electron beam induced deposition can achieve submicrometer dimensions, but the removal of material is more complicated if the same tool is to be used. An etching gas can be used(13) but this process is likely to be selective. Thus for controlled submicrometer repair processes at submicrometer dimensions focused ion beam induced deposition appears to be the preferred technique.

In this review we will briefly discuss the results that have been obtained with focused ion beam induced deposition and present some of the models of the process.

Table 1. Ion Induced Deposition Characteristics

Gas (Reference)	Ion, Energy	"Yield" (atoms/ion)	Deposit Composition	Resistivity ($\mu\Omega cm$)
Styrene (1)	Ga^+ 20 keV	3.6	C:O 65:30	
WF_6 (2), (9)	Ar^+ 500 eV & 2 keV		W:F:C 93.3:4.4:2.3	15
$W(CO)_6$ (3)	Ga^+ 25 keV	2	W:C:Ga:O 75:10:10:5	150 - 225
$W(CO)_6$ (4) (40^oC)	Ga/In/Sn 16 keV		W:C:O 50:40:10	100
$C_7H_7F_6O_2Au$ (5)	Ga^+ 40 keV (room T)	3-8	Au:C:Ga 50:35:15	500-1500 (Bulk Au = 2.44)
$C_7H_7F_6O_2Au$ (6)	Ga^+ 40 keV at 120^oC	3	Au:C:Ga 80:10:10	3-10
$C_9H_{17}Pt$ (7)	Ga^+ 35 keV	0.2-30	Pt:C:Ga:O 45:24:28:3 24:55:19:2	70-700 (Bulk Pt = 10.4)
$(CH_3)_3NAlH_3$ (10)	Ga^+ 20 keV	4-6	Al:Ga:C:N	900 $\mu\Omega cm$
$Si(OCH_3)_4$ + O_2 (8)	Si^{++} 60 keV	1 (molecule/ion)	SiO_x (no carbon)	2.5 ($M\Omega cm$)

(1) L.R. Harriott and J. Vasile, J. Vac. Sci. Technol. 36, 1037 (1988).
(2) Z. Xu T. Kosugi, K. Gamo, and S. Namba, J. Vac. Sci. Technol. B7, 1959 (1989).
(3) D.K. Stewart, L.A. Stern, and J.C. Morgan, SPIE (1989).
(4) Y. Madokoro, T. Ohnishi, and T. Ishitani, Riken Conf., Mar. 1989.
(5) P.G. Blauner, J.S. Ro, Y. Butt, and J. Melngailis, J. Vac. Sci. Technol. B7, 609 (1989).
(6) P.G. Blauner, Y. Butt, J.S. Ro, C.V. Thompson, and J. Melngailis, J. Vac. Sci. Technol. B7, 1816 (1989).
(7) T. Tao, J. Melngailis, Z. Xue, and H.D. Kaesz, EIPB 1990 and to be published J. Vac. Sci. Technol. (1990).
(8) H. Komano, Y. Ogawa, and T. Takigawa, Japn. J. Appl. Phys. 28, 2372 (1989).
(9) K. Gamo and S. Namba, Proc. 1989 Intern. Symp. on MicroProcess Conf. p. 293
(10) M.E. Gross, L.R. Harriott and R.L. Opila, J. Appl. Phys. 68, 4820 (1990).

3. RESULTS REPORTED

In the earlier reports of ion induced deposition from metal bearing precursor gases such as Al $(CH_3)_3$ (Ref. 14) Ta $(OC_2H_5)_5$ (Ref. 15) and Co $(CO)_6$, (Ref. 16) the concentration of impurities such as carbon and oxygen were high and generally no resistivity values were reported. Resistivity values of 500 $\mu\Omega$cm and higher were reported for gold deposition from $C_7H_7F_6O_2Au$ (Ref. 17). The characteristics of the films grown which are of interest in the application of focused ion beam induced deposition are: composition, microstructure, resistivity, yield (number of atoms deposited per incident ion), adhesion, damage, and minimum dimensions. We will address each of these aspects in turn, but first, the properties of some of the films recently deposited by the ion induced process are summarized in Table I.

A. Properties of the deposited films

1. Composition. The purity of films grown by ion induced deposition has been an important issue, and in almost all investigations Auger analysis has been used to measure composition. The factors which determine the composition of the film are: a) the composition of the precursor gas, b) the background gas in the vacuum chamber, c) the ion species used, and d) the process parameters, such as ion energy, current density, pressure and temperature.

   In ion induced deposition the precursor gas molecules adsorb on the surface (often in a monolayer) where the incident ions produce dissociation. The precursor gas molecule contains the desired atom, say a metal, which ideally remains on the surface while the other constituents of the molecule are volatile and are pumped away. For example, WF_6 might fit this model, and indeed as can be seen from Table I some of the purest, lowest resistivity films have been deposited from WF_6. (Unfortunately, WF_6 has a tendency to produce etching of the substrate rather than deposition in some cases.[18] So far, relatively pure deposits have been reported from WF_6 only with low energy ions, i.e. below 2 keV, Ref. 19 & 20). Most of the films deposited from metal organic compound[3] contain high concentrations of carbon. This is presumed to be due to the non-volatility of the reaction products. In the case of gold deposition from dimethylgold hexafuoroacetylacetonate heating the substrate during deposition to 120°C produced higher purity films.[21] This is thought to be due to the fact that the higher temperature causes reaction products to desorb more readily. Because of the high energy of the incident ions compared to the energy needed to break the bonds in the precursor gas molecule, the detailed nature of the chemical reaction on the surface is complicated and has so far no been studied in detail.

   The background gas in a vacuum system may contribute impurities if the pressure is not sufficiently low. The maximum average growth rate of films by ion induced deposition has been determined to be about 10Å/sec for gold at room temperature and 10mTorr of precursor gas pressure.[22] At a background pressure of 10^{-6} torr a monolayer forms in one second, which is comparable to the growth rate. Indeed, some of the earliest reported depositions from $Al(CH_3)_3$ (Ref. 14) and WF_6 (Ref. 15) contained substantial quantities of oxygen which were attributed to the background. Films of W grown later in better vacuum conditions showed much lower concentrations of oxygen.[19] [20]

In the practical applications Ga or other metal ions are usually used in ion induced deposition. These ions will, of necessity, implant the growing film. Clearly the higher the yield the lower will be the concentration of the Ga atoms in the film. Ga impurities in a metal film will likely increase the resistivity by less than a factor of 10, and so in practical applications of repair of conductors on integrated circuits it may not be an impediment. The carbon content of films, however, is important for applications of focused ion beam deposited films for the repair of x-ray lithography masks. As expected films containing about 50% carbon are only half as absorbing to x-rays as pure gold.[6] Some of the effects of process parameters on film composition will be discussed in conjunction with the microstructure.

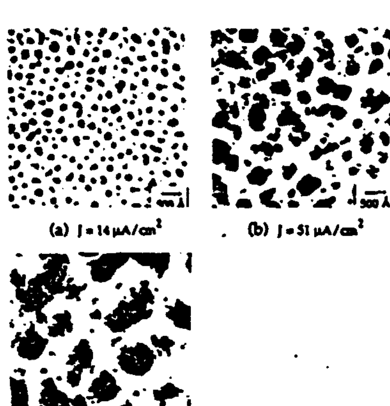

Fig. 3. From Ref. 24. Plan view TEM of ~1000Å thick films deposited with different current densities. The pressure of dimethylgold hexafluoroacetylacetonate was kept at 10 mTorr. The beam was 0.1 µm diameter with 100 pA of current scanned at 35 cm/sec with 0.05 µm spacing between raster lines.

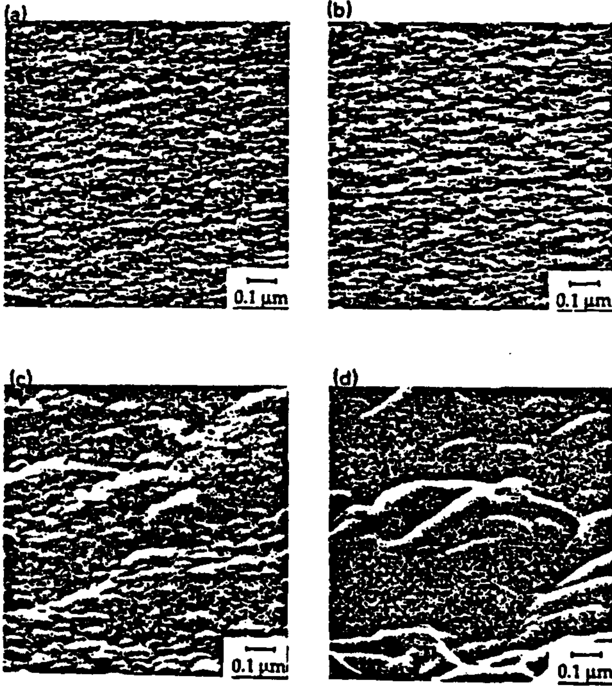

Fig. 4. From Ref. 22. SEM of films (> 500Å thick) deposited at various time averaged current densities (J), in the same condition as in Fig. 3. Y is the deposition yield uncorrected for Au composition. (a) $Y=8 \pm 1$ atoms/ion, $J=14\ \mu A/cm^2$, (b) $Y=6.7 \pm 0.4$ atoms/ion, $J=51\ \mu A/cm^2$; (c) $Y=3.9 \pm 0.3$ atoms/ion,[36] $J=217\ \mu A/cm^2$; and (d) $Y=0.2 \pm 0.2$ atoms/ion,[36] $J=865\ \mu A/cm^2$.

2. Microstructure. The detailed structure of the film can best be examined by transmission electron microscopy (TEM) or by scanning electron microcopy (SEM). So far, only gold has been studies extensively, [22] [23] [24] The films deposited at room temperature generally consist of crystalline islands in a background of carbon. Early stages of growth can be examined by TEM through a thin membrane of SiO_2. The results are shown in new line Fig. 3. The nominal thickness of the film is ~ 50 nm and if it were grown by standard electron beam evaporation or by sputtering it would be continuous and polycrystalline. Electron diffraction patterns indicate that the crystal structure of the islands is that of gold.[23] As seen in Fig. 3 the size of the islands depends on the average Ga ion current density. The coarsening of the film at higher current density can also be seen by SEM. Fig. 4. Higher current density seems also to lead to lower carbon content. Similarly lower pressure at constant current density yields coarser films and lower carbon content.[22] [24] As might be expected the initial island structure becomes a columnar structure as the films thickness is increased. This has been studies by cross sectional TEM. (Ref. 23) Since gold is a relatively non-reactive element, its behavior may not be typical of other metals. For example, the only other results on films produced by ion induced deposition are for platinum. As in the case of gold the films contains high concentrations of carbon, but TEM examinations show them to be amorphous, and the films are also observed to be very smooth by SEM.[18]

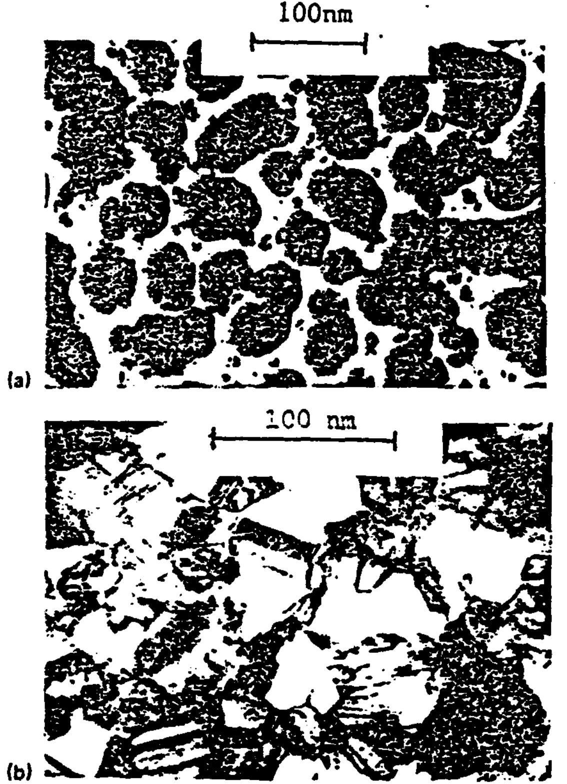

Fig. 5 From Ref. 23. Transmission electron micrographys of gold films grown by ion induced deposition at two substrate temperatures using a broad ion beam of 70 keV Ar^+ at 0.7 $\mu A/cm^2$ (a) Room temperature, nominal thickness 60 nm, total dose $1x10^{16}/cm^2$. Film is seen to be made up of unconnected gold islands. This discontinuous columnar structure was observed by cross sectional TM to persist even to 250 nm thicknesses. (b) 160°C, otherwise same conditions, thickness 100 nm. Film is seen to be continuous and has the microstructure typical of conventionally evaporated films.

As can be seen in Table I the purity of gold can be increased and the resistivity decreased if the ion induced deposition is carried out at temperatures above about 100°C. (Ref. 21 & 23) The microstructure of the gold film is found to be polycrystalline and continuous, as shown in Fig. 5, i.e. very much like that of e-beam evaporated films.

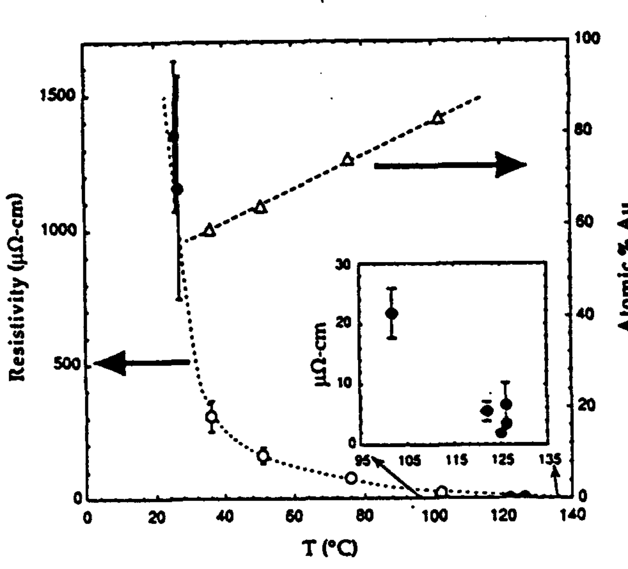

Fig. 6 From Ref. 21. The resistivity and gold content of lines as a function of substrate temperature during film growth. The closed circles represent values associated with deposits under 0.1 μm width, where compositional analysis was not possible. The open circles represent values associated with 1.2 μm wide lines from which both resistance and composition were measured. The inset shows the high-temperature region in more detail. The bulk resistivity of Au is 2.44 μΩcm. The uncertainties in the resistivity data correspond primarily to uncertainties in estimating the cross sections of the lines. Ga^+ ions at 40 keV and 20 to 100 pA beam currents were used.

3. Resistivity of films grown by focused ion beam induced deposition can be easily measured by depositing a line on an insulating substrate across metal fingers which are connected to probe pads.[22] The values reported for various materials are shown in Table I. They range over almost 2 orders of magnitude for the "metals", clearly the high resistivities reported are largely due to the impurities in the film. In the case of gold the microstructure is also believed to play a role since the rapid drop in resistivity with substrate temperature (Fig. 6) correlates also with a change in microstructure as discussed above. For applications to circuit restructuring and repair low resistivity is, of course, desirable. However, in many cases resistivities in the 100 μΩcm range can also be used if the connection is over relatively short distances. This range is comparable to the resistivity of the standard polysilicon conductors.

If more elaborate circuit restructuring is to be considered than the case shown in Fig. 2, then the ability to deposit an insulating film is useful. Deposition of an oxide of silicon with a resistivity of 2.5 MΩcm has been reported.[25] (See also Table I) This has been used to make a connection to a lower metal conductor through a metal film at a higher level.[26] The higher level metal exposed by milling down to the lower level metal was first covered by an oxide produced locally by focused ion beam induced deposition and then a metal was deposited to connect to the lower level.

4. The Deposition Yield is defined as the number of atoms deposited per incident ion. The film that is growing is of course also being simultaneously sputtered by the incident ions. Thus the deposition yield is the difference between the dissociation yield, i.e. the number of molecules dissociated per incident ion (assuming each molecule leaves one atom behind) and the sputter yield.[22] [27] The sputter yield can, of course, be easily measured by turning off the gas feed (Fig. 1) and observing the rate of material removal.

Values of deposition yield for numerous films have been reported and some are listed in Table I. Yields of several thousand have been reported for tungsten from WF_6 on cooled substrates,[15] and under some circumstances yield of about 100 have been reported for gold[16]

Table II Time to deposit 1 μm^3
(or $5x10^{10}$atoms)

Beam Current (nA)	Beam Diameter (Assuming $4A/Cm^2$) (μm)	Yield (atoms/ion)	Time (sec)
0.1	0.06	3	28
0.1	0.06	10	8.3
0.1	0.06	100	0.83
1.0	0.18	3	2.8
1.0	0.18	10	0.83
1.0	0.18	100	0.083

The yield is, of course, important in determining the film growth rate. The times needed to deposit a cubic micron for various conditions are listed in Table II. In some cases a cube of materials 1 µm on a side could not be deposited at this rate because the focused ion beam, if scanned over limited area, depletes the adsorbed gas and sputtering overtakes deposition.[17] [28] The numbers given in the table should be appropriate for films over large areas.

5. Adhesion of films grown by focused ion beam induced deposition has to our knowledge not been systematically studied. As a result of ion bombardment some mixing of the interface between the film and the substrate is expected to occur. This would no doubt promote adhesion. In the films used for photomask repair no adhesion problems have been reported. The gold films produced by ion induced deposition also seem to adhere well,[29] while e-beam evaporated films of gold usually require a thin adhesion promoting layer such as Cr.

6. Damage to the substrate is expected to occur for the same reason as enhanced adhesion, i.e., ion bombardment. This is of interest primarily if one wishes to consider making contacts directly on a semiconductor such as GaAs by ion induced deposition. Such contacts may be compatible with in-situ processing and may be useful for substrates which are degraded by exposure to the atmosphere. Unfortunately, in most cases annealing at temperatures high enough to remove the damage is not practical. Attempts to deposit Au directly on GaAs with 40keV and 10keV yielded poor quality Schottky characteristics.[30] However, tungsten contacts on GaAs formed by 0.5 and 2 keV ions have been reported to have good Schottky type characteristics after annealing at 350°C Ref. 20.

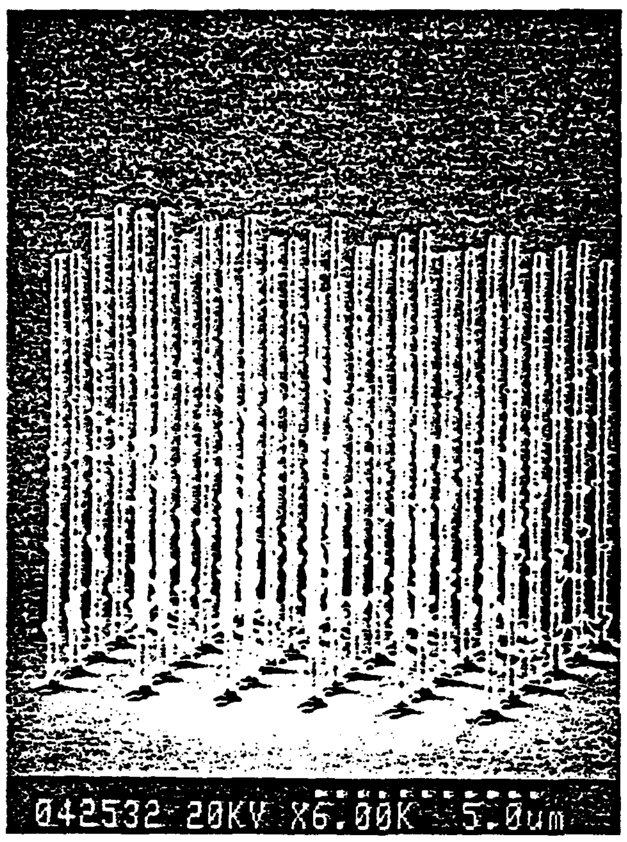

(a)

Fig. 7 From Ref. 6. An array of gold pillars grown using a 100 keV Ga ion beam at 13 pA. The pillars are approximately 0.15 μm diameter and 10 μm high.

7. The minimum dimensions of structures grown by focused ion beam induced deposition depend largely on the diameter of the beam used. Line widths of gold down to 0.1 μm have been reported.(22) The focused ion beam profile is generally Gaussian and the profile of lines whose thickness is of order the width also show a Gaussian shaped cross section. However, when thick films are deposited remarkably high aspect ratios have been observed,(6) as shown in Fig. 7. Why the Gaussian profile is not preserved in this case is not clear. No doubt, the deposition rate as a function of angle of incidence and the sputtering rate as a function of angle of incidence must be central to the explanation. Deposition yield as a function of angle of incidence has been measured for platinum.(18) It increases sharply as one approaches grazing incidence. The explanation for the remarkably high aspect ratio structures in Fig. 7 may lie in the supposition that sputtering yield increases faster as grazing incidence is approached than does deposition yield.

B. Models of ion induced deposition

As discussed above the body of experience in ion induced deposition permits some understanding of the process to be formed. This understanding can be at two levels, macroscopic and microscopic.

1. Macroscopic models of ion induced deposition describe the process in terms of the external parameters such as incident gas flux, incident ion flux, sputter yield, and resultant growth rate. The growth rate is determined by the deposition yield, Y_D, which is the difference between the total dissociation yield and the sputter yield, Y_s. The total dissociation yield can in turn be expressed as the product of the surface overage by the adsorbate, N (molecules/cm^2) and the dissociation cross section σ (cm^2). (Refs. 22 & 27). Thus

$$Y_D = N\sigma - Y_s$$

This equation has been verified in detail for gold deposition with 5 keV Ar ions incident on a quartz crystal microbalance.[27] The microbalance could be used to measure the surface coverage, N, of the precursor gas with no ions incident as well as the deposition rate when the beam is turned on, and also the sputter yield with gold film on the surface but no gas flux.

Following earlier work on electron beam induced deposition[10] expressions have been derived for the surface coverage, N, as a function of gas flux, sticking coefficient, and ion flux.[22] [31] When inserted to the expression above for Y_D, one should be able to predict the deposition rate for various conditions. Although these predictions have the general qualitative features expected, detailed fits of experimental data have not been carried out. One of the observations is that as the ion current density increases the yield decreases. In the case of focused ion beams one needs to distinguish between the instantaneous ion current density under the beam and the time averaged current density for a beam that is rapidly and repeatedly scanned over a surface.[17] [28] Conceptually the simplest regime in which to make measurements is with a focused ion beam which is scanned rapidly enough so that deposition is independent of scan speed.[22] In this regime, for example, the maximum deposition rate for gold is about 10Å/sec for an average current density of 200 $\mu A/cm^2$ at a precursor gas pressure of 10 mTorr. If the average current density is increased above this value the deposition rate falls rapidly because the precursor gas on the surface is depleted. Of course the precursor gas can be depleted and the etch rate can fall also if the scan speed is reduced by the beam being kept stationary.[28] With these considerations in mind one can find the optimum operating conditions in any practical situation .

2. Microscopic models of focused ion beam deposition seek to explain at an atomic level how the energy from the incoming ion is transferred to the adsorbed molecules. In many cases the substrate is covered by a monolayer of the precursor gas so that from the dissociation yield one can compute the average area surrounding the point of ion incidence in which the adsorbate molecules are broken up. The diameter of this area is typically of order 100Å.

After considerable experimentation and analysis[27] [32] [33] The picture that emerges is that the process is substrate mediated, i.e. the energy lost by the incoming ion excites the substrate locally surrounding the point of incidence and the substrate in turn causes the adsorbed molecules to break up.

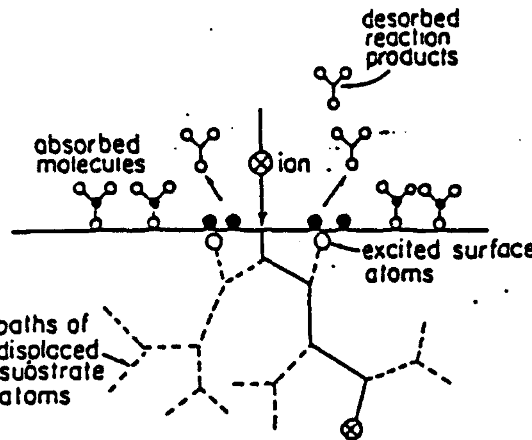

Fig. 8 A schematic of the collision cascade model. the incident ion (path represented by sold line) collides with host lattice atoms displacing them through the lattice (dotted paths). These displaced atoms collide in-turn with other lattice atoms. Some of these collision cascades reach the surface causing sputtering, if enough energy is transferred, or causing dissociation of adsorbed molecules, if the energy is above a lower threshold value.

The substrate excitation has been modelled[32] [33] both as a thermal spike and as a collision cascade. The latter model which is based on a Monte Carlo calculation using the TRIM-TC simulation program[34] appears to fit the data better than the thermal spike. A schematic of the collision cascade process is shown in Fig. 8. The incident ion scatters and displaces lattice atoms, some of them with sufficient energy to in turn displace other atoms, forming the, so called, collision cascades. When these collison cascades intersect the surface, surface atoms acquire energy. If this energy is above the sputtering threshold (typically several eV), then the surface atoms are removed. If the energy is above a lower threshold (0.95 eV for the gold precursor) then the adsorbate molecules may be dissociated.

This collision cascade model successfully predicts the sputtering yields and was found also to predict the dissociation yields for gold deposition using noble gas ions in the range of 2 to 10 keV (Ref. 32 & 33). We are in the process of extending these results to the 50 to 100 keV range.[23] [35]

4. SUMMARY

Focused ion beam induced deposition is an accepted microfabrication technique for local mask and circuit repair processes. Many materials have been deposited. The minimum dimensions of order 0.1 μm and high aspect ratios have been reported for gold deposits. Although in most instances the deposited films contain high concentrations of impurities, relatively pure films of Au and W have been reported under special conditions. The resistivities of the purer films are near those of ideal pure metals, while the more usual impure films have resistivities 20 to 100 higher than pure metals. Even at these resistivities the films are usable for local rewiring of integrated circuits.

The main outstanding challenges of ion induced deposition are the control of the impurities, the development of new and better precursor gases, and the increase of the deposition rate. A better understanding of the chemistry of the reaction which leads to deposition may help with these challenges, particularly the first two.

6. ACKNOWLEDGEMENTS

The author wishes to thank his co-workers who have shared their efforts to develop and understand ion induced deposition, particularly, Patricia G. Blauner, Andy D. Dubner, Jae Sang Ro, Carl V. Thompson, Al Wagner, and Tao Tao. Although the writing of this review paper has not been directly sponsored, the authors' work on ion induced deposition at MIT is supported by the Army Research Office, Contract No. DAAL-03-87-K-0126, by the Naval Research Laboratory Contract No. N00014-89-2238 under a subcontract from Micrion Corp. and by the IBM Corp.

7. REFERENCES

1. For recent reviews of the focused ion beam field see for example: L.R. Harriott, Applied Surface Science 36, 432 (1989). S. Namba, Nucl. Instr. and Methods in Physics Research B39, 504 (1989), J. Melngailis. J. Vac. Sci. Technol. B5, 469 (1987). J. Melngailis, Chapter in "Handbook of VLSI Microlithography" ed. W. Glendinning and J. Helbert, (Noyce Publishers 1991).
2. Two examples, are a) Illustrating the systematic variation of threshold voltage of 32 transistors: R.H. Walden, A.E. Schmitz, L.E. Larson, A.R. Kramer and J. Pasiecznik Proceedings of IEEE 1988 Custom Integrated Circuits Conference p. 18.7.1. b) High speed long channel CCD's with implanted doping gradients: J.E. Murguia, M.I. Shepard, J. Melngailis, A.L. Lattes, and S.C. Munroe Second Japan/US Seminar on Focused Ion Beams and Applications, Portland OR (Dec. 3-6, 1990) and to be published J. Vac. Sci. Technol. B
3. For an earlier review of ion induced deposition and references to the applications see J. Melngailis and P.G. Blauner Mat. Research Soc. Proceedings Vol. 147, p. 137 (1989).
4. D.K. Stewart, L.A. Stern, and J.C. Morgan S.P.I.E. Symp. Proc. "Electron Beam X-ray and Ion Beam Technologies: Submicrometer Lithographies VIII" (Mar. 1989) Vol. 1089, p. 18.
5. T.Tao, W. Wilkinson, and J. Melngailis, J. Vac. Sci. Technol. B (to be published).
6. A. Wagner, J.P. Levin, J.L. Mauer, P.G. Blauner, S.J. Kirch, and P. Longo, J. Vac. Sci. Technol. B (Nov/Dec 1990). To be published.
7. For reviews of laser-microchemical processing see, for example, D.J. Ehrlich and J.Y. Tsao, J. Vac. Sci. Technol. B4, 299 (1986) or D. Bauerle, Chemical Processing with Lasers (Springer, Berlin 1986).
8. S. Matsui and K. Mori, Japan J. Appl. Phys. 23, L706 (1986).
9. S. Matsui and K. Mori, J. Vac. Sci. Technol. B4, 299 (1986).
10. H.W.P. Koops, R. Weiel, D.P. Kern and T.H. Baum, J. Vac. Sci. Technol. B6, 477 (1988).
11. R.R. Kunz and T.M. Mayer, Appl. Phys. Lett. 50, 962 (1987).
12. W. Brünger, Microcircuit Engineering 9, 171 (1989).
13. S. Matsui and K. Mori, Appl. Phys. Lett. 51, 1498 (1987).
14. K Gamo, N. Takakura, N. Samoto, R. Shiminzu and S. Namura, Japan Journal of Physics 23, L293 (1984).
15. K. Gamo, Takehara, Y. Hamamura, M. Torita, and S. Namura, Microcircuit Engineering 5, 163 (1986).
16. W.P. Robinson, S.P.I.E. Symp. Proceedings "Electron Beam X-ray and Ion Beam Technologies: Submicrometer Lithographies VIII" Vol. 1089, p. 228 (1989).
17. G.N. Shedd, A.D. Dubner, H. Lezec, and J. Melngailis, Appl. Phys. Lett. 49, 1584 (1986).
18. T. Tao, J.S. Ro, J. Melngailis, Z. Xue, and H. Kaesz, J. Vac. Sci. Technol. B (Nov/Dec 1990). Also T. Tao private communication.
19. Z. Xu, T. Kosugi, K. Gamo, and S. Namba, J. Vac. Sci. Technol. B7, 1959 (1989).

20. K. Gamo and S. Namba, Proc. of 1989 Intern. Smyp. on MicroProcess Conf. p. 293.
21. P.G. Blauner, Y. Butt, J.S. Ro, C.V. Thompson, and J. Melngailis, J. Vac. Sci. Technol. B7, 1816 (1989).
22. P.G. Blauner, J.S. Ro, Y. Butt, and J. Melngailis, J. Vac. Sci. Technol. B7, 609 (1989).
23. J.S. Ro, A.D. Dubner, C.V. Thompson, J. Melngailis, Mat. Research Soc. Symp. Proc. Vol. 101 P. 255 (MRS 1988).
24. P.G. Blauner, J.S. Ro, Y. Butt, C.V. Thompson and J. Melngailis, Mat. Res. Symp. Proc. Vol. 129, p. 483 (1989).
25. H. Komano, Y. Ogawa, and T. Takigewa, Japan J. Appl. Phys. 28, 2372 (1989).
26. H. Komano and H.. Nakamura, "Second Japan/US Seminar on Focused Ion Beams and Applications", Portland, Oregon Dec. 3-6, 1990 and to be published J. Vac. Sci. Technol. B
27. A.D. Dubner, and A. Wagner, J. Appl. Phys. 66, 870 (1989).
28. P. Levin, P.G. Blauner, and A. Wagner, SPIE Symp. Proc. "Electron Beam, X-ray, and Ion Beam Technologies: Submicrometer Lithographies IX", Vol. 1263, p. 2 (1990).
29. J.S. Ro Private communication.
30. P.G. Blauner, L. Mahoney and C.L. Chen (private communication).
31. F.G. Rüdenauer, W. Steiger, and D. Schrottmayer, J. Vac. Sci. Technol. B6, 1542 (1988).
32. A.D. Dubner, Mechanism of Ion Induced Deposition Ph.D. Thesis MIT (Sept. 19990).
33. A.D. Dubner, A. Wagner, J. Melngailis and C.V. Thompson, "Second Japan/US Seminar on Focused Ion Beams and Applications", Portland, OR Dec. 3-6, 1990 and to be published.
34. J.P. Biersack and L.G. Hagmark Nucl. Instr. and Methods 174, 257 (1980).
35. J.S. Ro et al. to be published.

MATERIALS ISSUES IN X-RAY MASK REPAIR BY FOCUSED ION BEAMS

JOHN MELNGAILIS
Massachusetts Institute of Technology, 77 Massachusetts Ave. Cambridge, MA 02139

ABSTRACT

In x-ray mask repair high Z absorber features, such as gold or tungsten, must be removed or added. The main challenges are the small lateral dimensions (0.25 µm and below) and the thickness of the absorbers (~ 0.5 µm) The focused ion beam appears to be the best tool developed to meet this challenge. Unwanted features are removed by ion milling while missing absorber is reconstructed using ion induced deposition from a locally piped-in precursor gas. The high aspect ratio of the features complicates both of these processes. Milling away 0.5 µm thick absorber can lead to redeposition of the sputtered material on neighboring features. The crystal grains of the absorber mill at different rates depending on orientation which results in nonuniform features. A possible alternative which only works with W absorber is to use ion assisted etching. In ion induced deposition a precursor gas such as dimethylgold hexafluoro acetylacetonate is provided by a capillary tube aimed at the region scanned by the ion beam. The incident Ga^+ ions, usually at energies in the 25-100 keV range, dissociate the adsorbed precursor molecules leaving a deposit of gold mixed with carbon. The carbon content can approach 50 atomic % resulting in an x-ray attenuation which is about one half of that of pure gold. A number of unexplored materials science issues are associated with mask repair including: the reduction of the carbon content, redeposition both from milling and from induced deposition, milling as a function of crystal orientation and energy, and deposition of high aspect features. The technology is well enough developed so that mask repair of 0.25 µm features can be considered. However, a better understanding of the materials science aspects of x-ray mask repair will help to advance the state-of-the-art.

INTRODUCTION

X-ray lithography is likely to be used to print patterns with more than 10^9 features per chip at minimum dimensions below 0.2 µm. Even in present day optical lithography with coarser and less numerous features mask repair is widely used. For x-ray masks, repair-after-initial-fabrication is likely to be even more important.

The repair of x-ray masks presents special challenges. Compared to optical mask repair, not only are the dimensions smaller, but the absorber film thickness and, therefore, the aspect ratio is much larger. This is illustrated in Fig. 1. Absorber features with height to width ratios as high as 5 or more may need to be reconstructed,. Since the absorber thickness currently used varies between 0.3 and 0.6 µm depending on the spectrum of the radiation and the absorber material (typically Au or W) and since minimum dimensions down to 0.1 µm need to be considered. The repair tool will need to be able to remove or to add material with high resolution, with high aspect ratio and with high placement accuracy. The tool that has been most intensely developed for this purpose is the focused ion beam. Material removal is done by sputtering (also called ion milling) with a beam of diameter

To be published MRS Proceeding (Spring Mtg. 1993, San Francisco)
"Materials Aspects of X-ray Mask Repair"

down to 0.03 μm while material addition is done by ion induced deposition from a, usually organometallic, precursor gas [1]. After describing typical apparatus, we will examine the materials science aspects of these two novel techniques as they relate to x-ray mask repair and also briefly discuss ion assisted etching.

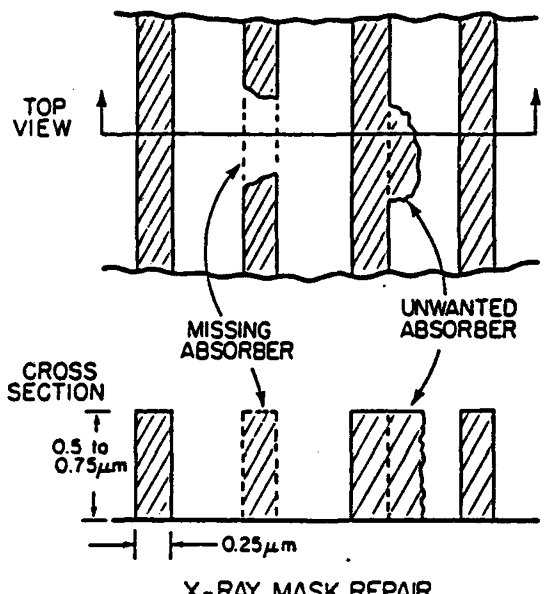

Fig. 1 Schematic of a small portion of an x-ray mask showing 4 parallel metal lines with two defects. The missing absorber with a high aspect ratio needs to be replaced by focused ion beam induced deposition, and the unwanted absorber needs to be milled off.

MASK REPAIR APPARATUS

Because of its simplicity, reliability, and long life, the Ga^+ ion source is almost universally used in mask repair. This bright point source of ions is imaged onto the specimen by electrostatic optics. The ion optical column which looks and functions much like a scanning electron microscope (SEM) produces a beam with minimum diameter of 25 nm and an average current density in the focal spot of about 5 A/cm^2 [2]. With special effort, beams down to 8 nm have been achieved in the laboratory [3]. By detecting secondary electrons one can image a sample. The surface is, of course, eroded but the loss of material can be as little as a monolayer if image frame storage is used. The secondary ions can also be detected. By mass analyzing them one can realize a high resolution SIMS (secondary ion mass spectrometer) [4]. Thus one can find the defect, repair it, and then see and analyze the result.

A schematic of the apparatus is shown in Fig. 2. For ion induced deposition a capillary tube feeds the precursor gas to the surface where the ion beam is incident. The local pressure on the surface is in the 10^{-2} to 10^{-3} Torr range. In the rest of the chamber the pressure is in the 10^{-5} to 10^{-7} Torr range as needed for ion propagation. The column is separately pumped and is usually at even lower pressure. For imaging or for milling, of course, the precursor gas is simply turned off.

A mask repair machine is also equipped with computer controlled electronics which accepts the results of a mask inspection tool and moves the sample stage so that the defects, in turn, appear within the scan range of the ion beam. Each defect is then outlined as a subfield of the scan field, and material is either milled away or deposited over this subfield. Although the focused ion beam imaging [5] and mass analysis are important materials

science topics in their own right, we will focus here on the milling and induced deposition which are the key processes for mask repair.

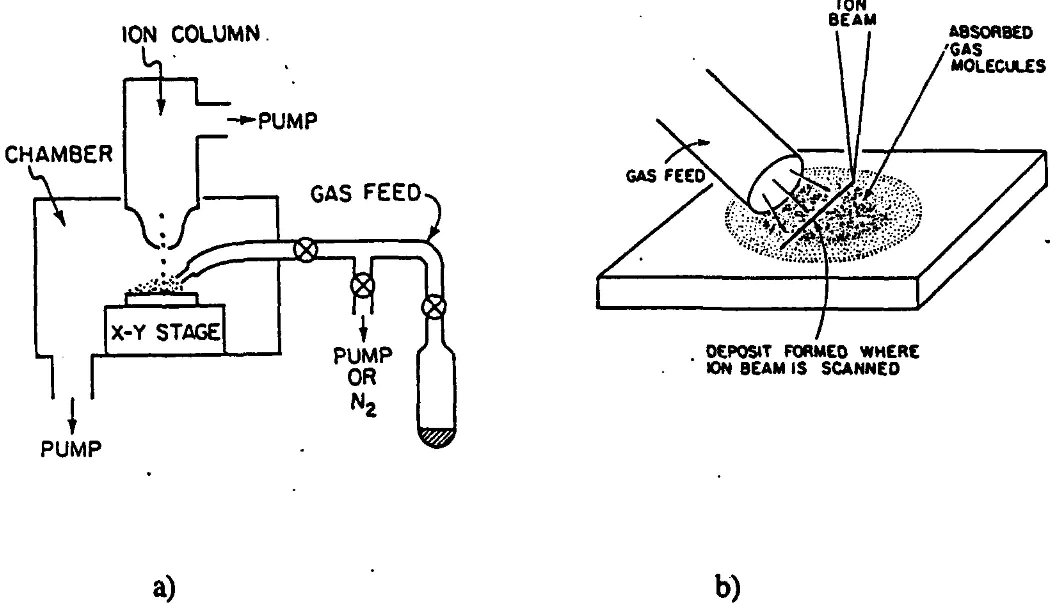

Fig. 2 a) Schematic of the apparatus used for focused ion beam induced deposition. The gas feed creates a local gas ambient on the sample area which is scanned by the ion beam. For low vapor pressure gases such as $W(CO)_6$ the entire gas feed system may need to be heated. b) The deposition area shown schematically close-up.

ION MILLING

Sputter Yield

The removal of surface atoms by energetic ion bombardment, also called sputtering, is a well known phenomenon and plays an important role in microfabrication. Each incoming ion removes a number of substrate atoms. The number (atoms/ion) is called the yield. In the simplest case the yield depends on the mass and energy of the incoming ion as well as the mass and binding energy of the atoms of the substrate. Various ion/substrate combinations have been tabulated, [6] particularly for noble gas ions.

Some additional dependences can become important, especially in the case of focused ion beams. The yield depends on the angle of incidence between the ion and the substrate surface, the orientation of crystallographic axis with respect to the beam direction, and sputtered material redeposition. To compare yield with a focused beam of Ga^+ ions to conventional ion beam results, these complications should be avoided. To do this the yield must be measured with a focused beam rapidly scanned over an area whose dimensions are large compared to the depth milled, and the material must be either amorphous, single

crystal, or fine grained (i.e. with grains small compared to the depth of the pit milled). The reasons for these restrictions will be discussed below.

Various measurements of yield are listed in Table I. for comparison with the Ga^+ ion yield some values of yield for Kr^+ ions are included. This noble gas ion of atomic mass 83.8 is nearest to Ga which has atomic mass 69.7. (Much more data can be found in Ref. 6). For these materials and ions and for the energy range considered (25 keV to 100 keV) the yield increases slowly with energy. In the case of gold there appear to be some disagreement in the data. Most of this disagreement is probably due to the details of the crystal structure of the films.

Table I. Ion milling yields for focused Ga (atomic mass 69) and broad beam Kr ions (atomic mass 84)

Substrate	Ion	Energy (keV)	Yield (atoms/ion)	Reference
Si	Ga^+	30	3.1 ± 0.8	8
Si	Ga^+	25	2.6	9
Si	Ga^+	25	3.9 ± 0.4	7
Si	Kr^+	25	3.1	6
Au	Ga^+	100	32	10
Au	Ga^+	40	15.7 ± 1.3	11
Au (plated)	Ga^+	25	18 ± 3	7
Au (evap)	Ga^+	25	23 ± 5	7
Au	Kr^+	25 45	20 28	6
W (RF sputt.)	Ga^+	25	5 ± 0.7	7
W	Kr^+	22	4.1	6
SiO_2	Ga^+	68	2.0*	12
SiO_2	Ga^+	25	0.84*	7

*molecules/ion

Crystal Structure

An ion which is incident on a crystal along a symmetry axis will penetrate deeper than one incident along a random direction. This effect, known as channeling, means that the amount of energy lost near the surface depends on orientation. Thus also the sputter yield depends on orientation. This has been observed by anyone who has ion milled a polycrystalline surface as a roughening. See for example Fig. 3. Milling of gold or

tungsten polycrystalline films is seen to result in a rough surface while milling of single crystal silicon is seen to result in a smooth surface. The tungsten and gold films were chosen to be similar to those used in x-ray masks i.e. plated gold and rf sputter deposited tungsten. (Incidentally the same channelling effect also leads to a variation of the secondary electron yield from crystal grain to crystal grain. This means that if a polycrystalline surface is viewed in the scanning ion microscope mode the crystal grains stand out clearly. See for example Refs. 5, 13. This appears to be a very useful method for observing crystal grain structure).

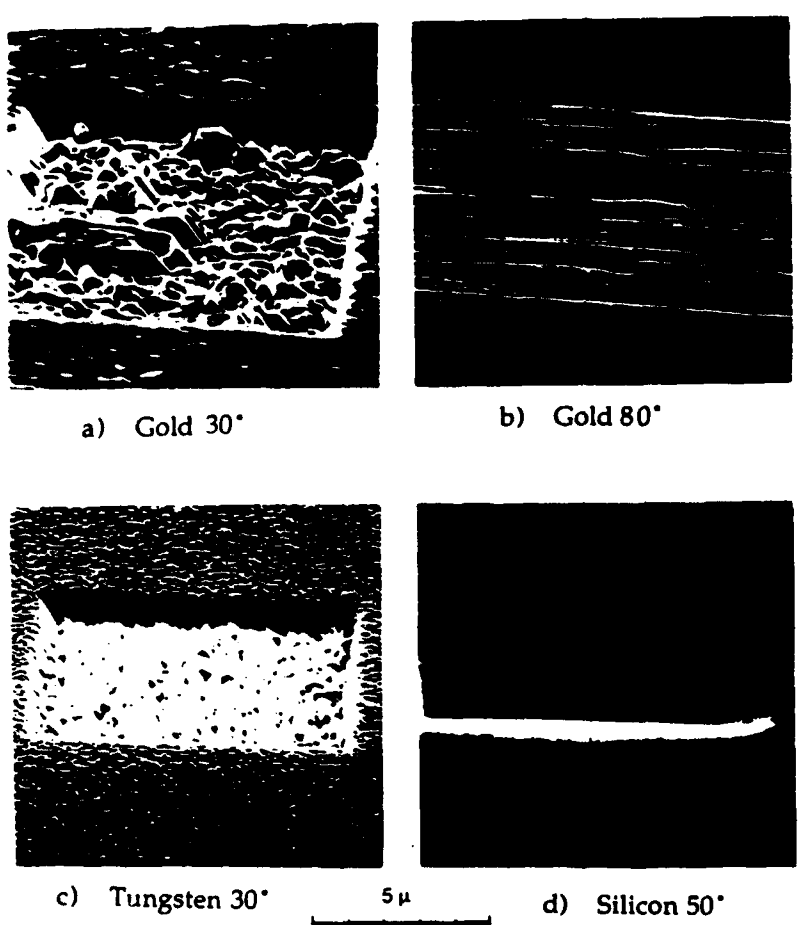

Fig. 3 From Ref. [7]. FIB milling of three materials at various angles of incidence with a 25 keV-Ga^+ beam current of 283 pA and a dwell time per pixel of 0.3 µs. For (a) and (b) the average current J_{av} = 290 $\mu A/cm^2$ and the time to mill the box is 2 min for (c) J_{av} = 700 $\mu A/cm^2$ mill time 8 min and for (d) J_{av} = 710 $\mu A/cm^2$ mill time 3 min. In mask repair most milling will be at normal incidence or near glancing. Glancing incidence as in (b) will occur when a feature is trimmed and may result in an uneven sidewall.

Effect of Angle of Incidence

The angle of incidence, i.e. the angle between the normal to a surface and the ion arrival direction, affects the sputter yield on both a macroscopic and microscopic level. If we simply mill large, relatively shallow pits in samples tilted at various angles with respect to the ion beam and use a rapid beam scan, we can measure the milling yield vs. angle [7] Some sample results are shown in Fig. 4. The yield increases up to about 75-80° and then drops as glancing incidence is approached. Monte Carlo (TRIM) simulations also reveal qualitatively the same behavior. The drop off is due to the fact that as glancing incidence is approached, the probability that the ion escapes from the surface after the first collision approaches 50%. Since it can also escape after the second collision etc., the effectiveness of the collision cascade is substantially reduced.

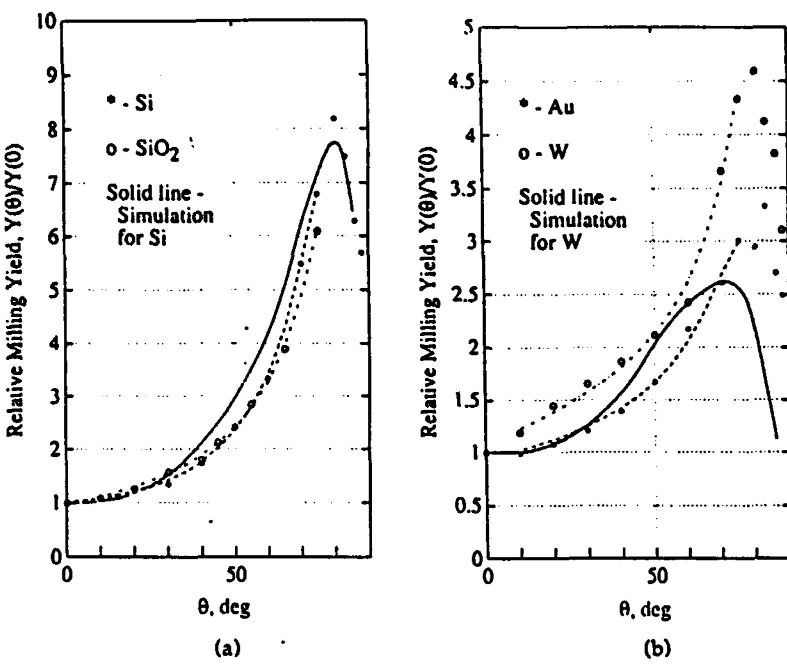

Fig. 4 From Ref. [7]. Relative milling yield vs angle of incidence. The solid lines represent the results from a Monte Carlo simulation (TRIM). The dotted lines serve only to guide the eye. Results for SiO_2 were obtained by milling a quartz fiber with 35 keV $^{69}Ga^+$ at a beam current of 110 pA and an average current density of 2.9 pA/μm^2. Milling conditions for the rest: beam 25 keV $^{69}Ga^+$, beam current 283 pA, dwell time 0.3 μs/pixel, average current density 7 pA/μm^2 for W and Si, 2.9 pA/μm^2 for Au.

This dependence on angle of incidence can play a role also in the microscopic process of focused ion beam milling, particularly if the beam is scanned slowly, so that the thickness of material removed per beam scan is comparable to the beam diameter [14]. This is illustrated in Fig. 5. For example, for the milling of Si, with a focused ion beam of 1 A/cm^2 current density, 0.1 μm of material is removed in 24 msec. Since 0.1 μm is comparable to a typical beam diameter, the beam should spend considerably less time per scan at each point on the sample. Otherwise the milling yield will be a function of the scan rate.

This concept could, of course, be turned around and used to maximize the yield, i.e. the scan rate could be chosen so that the slope of the surface under the beam in Fig. 5 corresponds to the incidence angle where the sputter yield is maximum. This may, however, lead to complications. Strictly speaking the one dimensional picture drawn in Fig. 5 only applies if the beam is scanned very rapidly into the page and the beam is, in effect, a uniform blade which advances to the right in the figure. If the scan rate into the paper also has to be considered, the problem becomes three dimensional. In addition the direction of the sputtered material will be predominantly toward the left in Fig. 5 and may lead to more redeposition of materials on the surface that has just been milled.

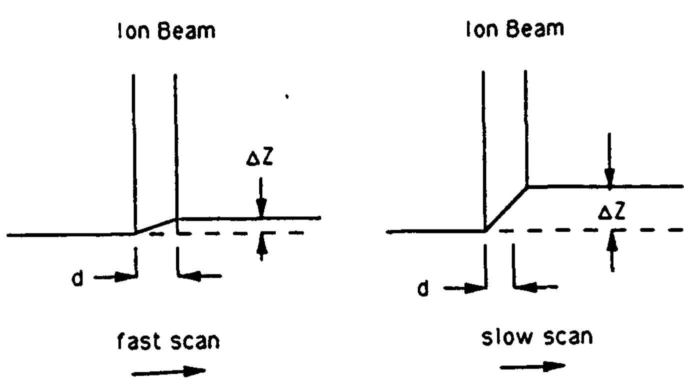

Fig. 5 After Ref. [14]. If the amount of material removed per scan ΔZ is comparable to the beam diameter, d, then on a microscopic scale the ion milling will be at non normal incidence. Of course, the ion beam has an approximately Gaussian cross section so that the profile of the interface being milled will be a curved surface rather than straight.

Redeposition

Not only does redeposition on the surface being milled need to be considered, but also redeposition on neighboring features particularly if the surface has severe topography as it does on x-ray masks.

To model the effect of redeposition we need to know the angular distribution of the sputtered material. This has been measured at the Fraunhofer Institute, Refs. 10, 15 by covering the sputtered surface with a semicylindrical glass screen, where the line being sputtered is along the axis of the cylinder. The relative thickness of the sputtered material is shown in polar plots for two angles of incidence of the 100 keV Ga^+ ion beam on a gold surface Fig. 6. The distribution is seen to be somewhat broader at 45° than at normal incidence.

Given the angular distribution of the sputtered atoms, the beam diameter, the scan speed, (which determines the local angle of incidence, see Fig. 5) and the sticking coefficient of the redeposited atoms the shape of milled features can be calculated. This has been done [15] [10] for a deep pit milled into 1.2 µm of Au deposited on a Si substrate (as in an x-ray mask). This pit, Fig. 7 is milled in a single scan from left to right, and severe redeposition can be seen on the left side of the pit. The simulation, with the sticking coefficient of the redeposited atoms chosen to be 0.5, is seen in Fig. 7 to predict the observed shape of the pit.

Of course, the single-scan milling of a pit is not the strategy one would use in repairing an x-ray mask or milling any relatively deep feature. If the pit is milled with many repeated rapid scans, its shape will be that of the area of the scan and the gross redeposition shown in Fig. 7 can be entirely avoided. For milling of deep pits there are some secondary effects. When the bottom of the pit is milled, redeposition on the nearly vertical sidewalls will occur. When this material is in turn milled off as the beam approaches the sidewall, redeposition will occur on the bottom, etc. In addition the incident ion may scatter along the sidewall. The slope of the sidewall of a deep pit is mainly determined by the diameter of the beam. This has also been simulated [15]. Since diameters of 25 nm will be used for mask repair, quite steep milling of features will be possible.

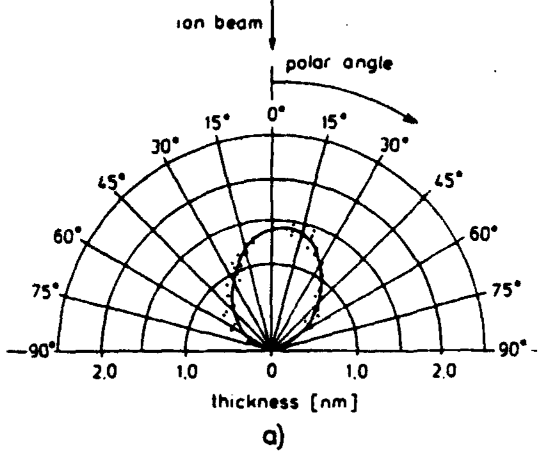

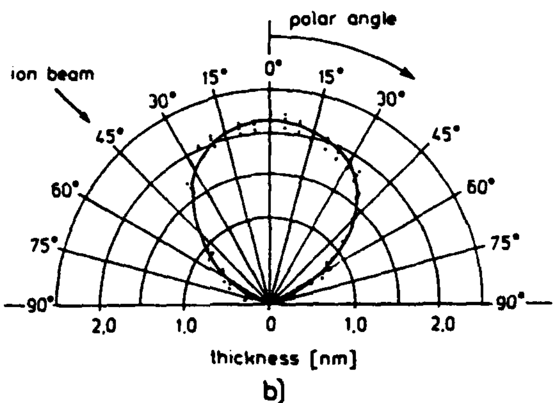

Fig. 6 From Ref. [15]. Polar plot of the redeposition of gold ion milled with a focused 100 keV Ga^+ beam. The beam was scanned along a line at the origin perpendicular to the page, the redeposited material was collected on a half cylinder concentric with the scan, its thickness measured, and plotted as the radius. See also Ref. [10].

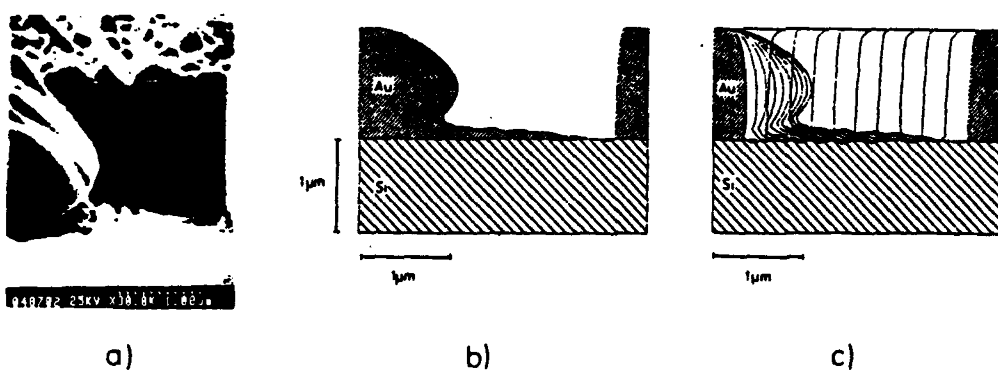

Fig. 7 From Ref. [15]. Observed (a) and simulated (b) & (c) redeposition for a pit milled in polycrystalline gold with a single scan from left to right. Part (c) shows the time evolution of the profile. The beam was 100 keV Ga^+ of 0.1 μm diameter with a step size of 1.2 nm from left to right. A sticking coefficient of 0.5 was assumed for the sputtered material.

ION INDUCED DEPOSITION

To replace missing x-ray mask features high Z material needs to be deposited. Suitable materials which have been demonstrated so far are listed in Table II. The first issue is, can these materials be deposited with the required high aspect ratio. Fig. 8 and 9 show some examples of high aspect ratio depositions of W and Au. So far high aspect ratios of Pt have not been reported, although there is no reason to believe they cannot be produced.

Table II. Ion Induced Deposition Properties of Materials Useful as X-ray Mask Absorbers

Gas (Reference)	Ion, Energy	"Yield" (atoms/ion)	Deposit Composition	Resistivity (μΩcm)
WF_6 [20] [21]	Ar^+ 500 eV & 2 keV		W:F:C 93.3:4.4:2.3	15
$W(CO)_6$ [23]	Ga^+ 25 keV	2	W:C:Ga:O 75:10:10:5	150 - 225
$W(CO)_6$ [24] (at 40^oC)	Ga/In/Sn 16 keV		W:C:O 50:40:10	100
$C_7H_7F_6O_2Au$ [11]	Ga^+ 40 keV (room T)	3-8	Au:C:Ga 50:35:15	500-1500 (Bulk Au = 2.44)
$C_7H_7F_6O_2Au$ [25]	Ga^+ 40 keV at 120^oC	3	Au:C:Ga 80:10:10	3-10
$C_9H_{17}Pt$ [26]	Ga^+ 35 keV	0.2-30	Pt:C:Ga:O 45:24:28:3 24:55:19:2	70-700 (Bulk Pt = 10.4)

Mechanism of Ion Induced Deposition

After study of the deposition of gold from dimenthylgold hexafluoroacetylacetonate (also known as DMG (hfac) or $C_7H_7O_2F_6$ Au) a picture of the atomic mechanism has emerged. The deposition rate was measured using various noble gas ions to bombard the surface with energies from 2 to 100 keV. The decomposition yield varied from near 0 to 30, and increased with increasing mass and increasing energy [16, 17, 18, 19]. The deposition results from a competition between addition of gold by decomposition of the adsorbed molecules of gas and the sputtering of the grown film by the ion beam. We assume that

$$Y_N = Y_D - Y_S \qquad (1)$$

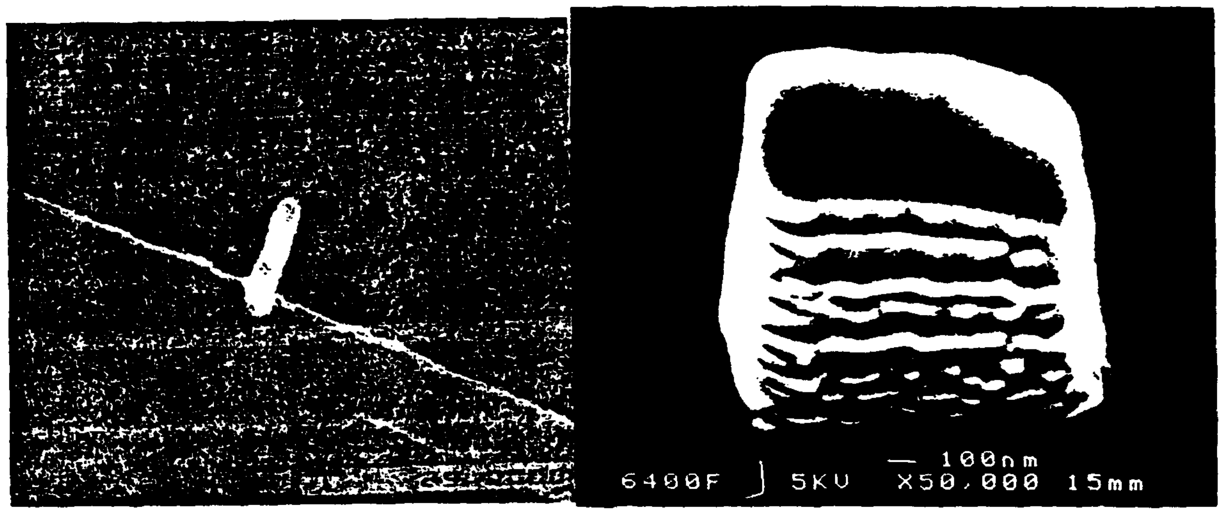

Fig. 8(a) From Ref. [27]. A high aspect ratio tungsten column 3 µm high and 0.6 diameter. Deposited with 25 keV Ga^+ ions.

Fig. 8(b) From Ref. [28]. A 0.5 x 0.5 µm tungsten deposit 0.8 µm thick.

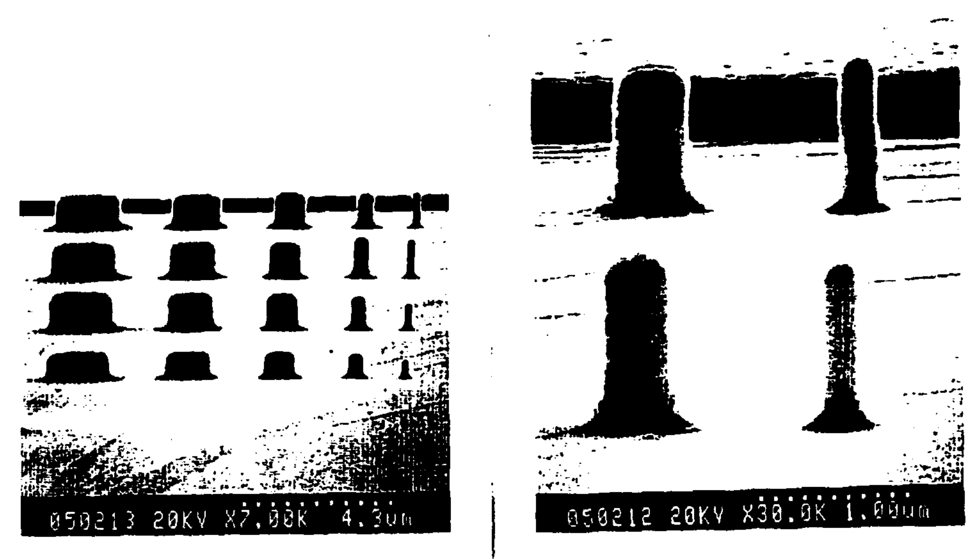

Fig. 9 From Ref. [29]. A series of gold boxes varying in size from 2x2 µm to 0.25x0.25 µm. On the left is an expanded view of the smallest boxes. Note the "foot" at the base of each feature. Deposited with a 100 keV, 15 pA Ga^+ beam, approximately 0.06 µm diameter.

where Y_N is the net deposition yield and Y_D and Y_S are the decomposition and sputter yields respectively. An alternate view has also been proposed, namely that the sputtering can occur only where the surface is not covered by precursor gas [30]. Unfortunately, since Y_S (measured by turning off the precursor gas and sputtering the grown film), and Y_N appear to be proportional to one another, these two models cannot be readily distinguished by simple experiments. All of the noble gas ion experiments were done under conditions where the gas flux on the surface was much larger than the ion flux. Thus the surface was mostly covered by a monolayer, [33] and whether we calculate Y_D from $Y_D = Y_N + Y_s$ or $Y_D = Y_N + \gamma Y_S$, where γ is a function of the adsorbate coverage and accounts for the reduced sputtering, will not alter the relative dependence of Y_D on energy and mass of the ions. Both simulations and experiments indicate that Y_N is proportional to Y_s as the mass and ion energy are varied.

The same collision-cascade, Monte-Carlo-TRIM model that successfully accounts for sputtering can be modified for deposition. When a collision cascade terminates on the surface and imparts an energy greater than the binding energy (3.8 eV for gold) to a surface atom it will be sputtered off. If on the other hand the collision cascade terminates on a surface covered with adsorbed precursor, and imparts an energy greater than the dissociation energy (0.95 eV) to the molecule it will decompose leaving the gold behind. The dependence of Y_D on energy and mass correlates very well with the dependence calculated from this model [16-19].

Composition and Microstructure of Deposits

All of the precursor gases used to deposit W, Au and Pt listed in Table II contain carbon. Unfortunately, this results in carbon incorporation into the "metal" film at up to 50 at %. Since Ga^+ ions are used to induce the deposition Ga is also implanted into the film. The at % of Ga is inversely proportional to the yield.

The microstructure of the films has been studied for gold [31]. For most room temperature deposition conditions the film consists of islands of pure gold in a background of carbon. This is seen by examining the films by transmission electron microscopy (TEM) at the early stages of growth. See Fig. 10. Films grown on samples heated to 100-160°C have the crystal structure of normal polycrystaline metal films, i.e. contiguous grains of various orientations, Fig. 11. In addition, the films grown at higher temperatures have a resistivity near that of pure gold, i.e. 2.5 μΩcm, while the films grown at room temperature typically have resistivities in the 500-10,000 μΩcm range.

As the films, shown in Fig. 10, thicken they can either grow as gold columns or as gold grains. These have been observed by cross section TEM [31, 14, 33]. Overall depending on the growth conditions three different types of microstructure can be observed in the case of gold as sketched in Table III.

The microstructure of Pt film has been examined only once [26]. It was found to be amorphous, i.e. completely featureless and having electron diffraction rings corresponding to amorphous films [26]. This is also consistent with the observation that the surface of Pt films is found in SEM examination to be quite smooth, in contrast to the Au and W films which have a bumpy surface.

The x-ray attenuation of a film that is 50 at % C is only about half of that of a pure gold film of the same thickness. Thus the purity and microstructure issues of these films are important.

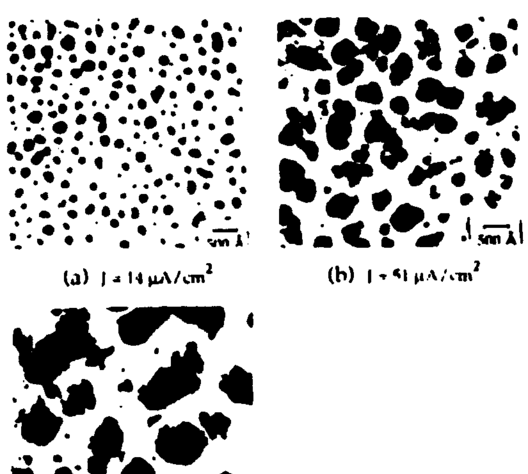

Fig. 10 From Ref. [32]. Plan view TEM of ~ 100 nm thick gold film deposited at different average current densities, from DMG (hfac) at 10 mTorr 100 pA, 0.1 μm-diameter Ga^+ beam at 40 keV. The respective three deposition yields for the current densities were a) 8 at/ion b) 6.7 c) 3.9.

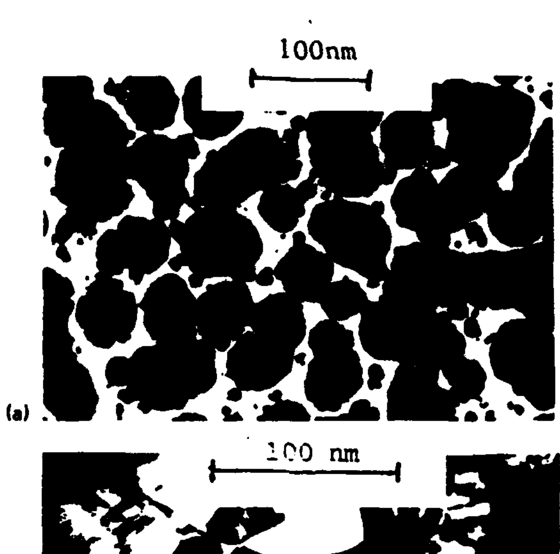

Fig. 11 From Ref. [31]. Transmission electron micrographs of gold films grown by ion-induced deposition at two substrate temperatures: (a) Room temperature, nominal thickness 60 nm, 70 keV Ar^+ ions at 0.7 $\mu A/cm^2$, total dose $1x10^{16}/cm^2$. Film is seen to be made up of unconnected gold islands. This discontinuous columnar structure was observed by cross sectional TEM to persist even to 250 nm thicknesses. (b) 160°C, otherwise same conditions, thickness 100 nm. Film is seen to be continuous and has the microstructure typical of conventionally evaporated films.

Table III Microstructure of "gold" films. Ref. [18]
Data from Ref. [31], except 5 kV Ref. [17]

Type		Composition	Conditions	
	granular	more than 50% C	Ar^+ 70 kV 7 $\mu A/cm^2$ room T	
	columnar	30-50% C	Ar^+ 70 kV 0.7 $\mu A/cm^2$ room T	Ar 70 kV 7 $\mu A/cm^2$ $T \sim 100^oC$
	polycryalline	less than 30% C	Ar^+ 70 kV $T > 100^oC$ 0.7 $\mu A/cm^2$	Ar^+ 5 kV room T $\sim 5 \mu A/cm^2$

Deposition vs. Angle of Incidence and Redeposition

The high aspect ratio features on x-ray masks introduce complications in the ion induced deposition of metal to replace missing absorber. Deposition at non-normal incidence has to be considered as well as unwanted deposition on nearby structures due to sputtering during deposition or to ion scattering.

The deposition yield has been measured for W, Pt, and Au as a function of angle of incidence of the ion beam [35] [7]. A simple way to do this is to deposit on a round fiber and then examine the fiber in an SEM. The result for gold is shown in Fig. 12. The deposit is seen to become ripply at about 50°. These ripples grow in amplitude and become quite deep as grazing incidence is approached [7]. The mechanism for the formation of these ripples is not understood but they are observed also for tungsten [7], Fig. 13, and for Pt [26, 35]. Because of these ripples the deposition yield as a function of angle of incidence is difficult to measure accurately. In Pt the ratio of the yield at normal incidence to the maximum yield near grazing incidence is about 6 while for tungsten it is between 1.5 - 3. Refs. 7, 35.

Another relevant observation is that the deposition yield is much higher in a narrow and deep pit than on a flat surface. This has been observed for Pt [26] and for W [36]. For example, Pt deposited in a trench 0.7 µm deep 0.4 µm wide is estimated to have a yield 6 times higher than on a flat surface. In the case of W, pits that were filled were cross sectioned. No apparent cavities or voids were found, [36] as might have been expected from the observations in Figs. 12 & 13. One can speculate that this high yield in a pit is due to the fact that sputtered material is collected and does not escape and the sputtered or scattered atoms and ions can in turn induce dissociation of the adsorbed precursor gas molecules. The composition of the deposit in the pits compared to that on a flat surface has not been measured. Given the observations in Table III one might suspect that the carbon content may be higher.

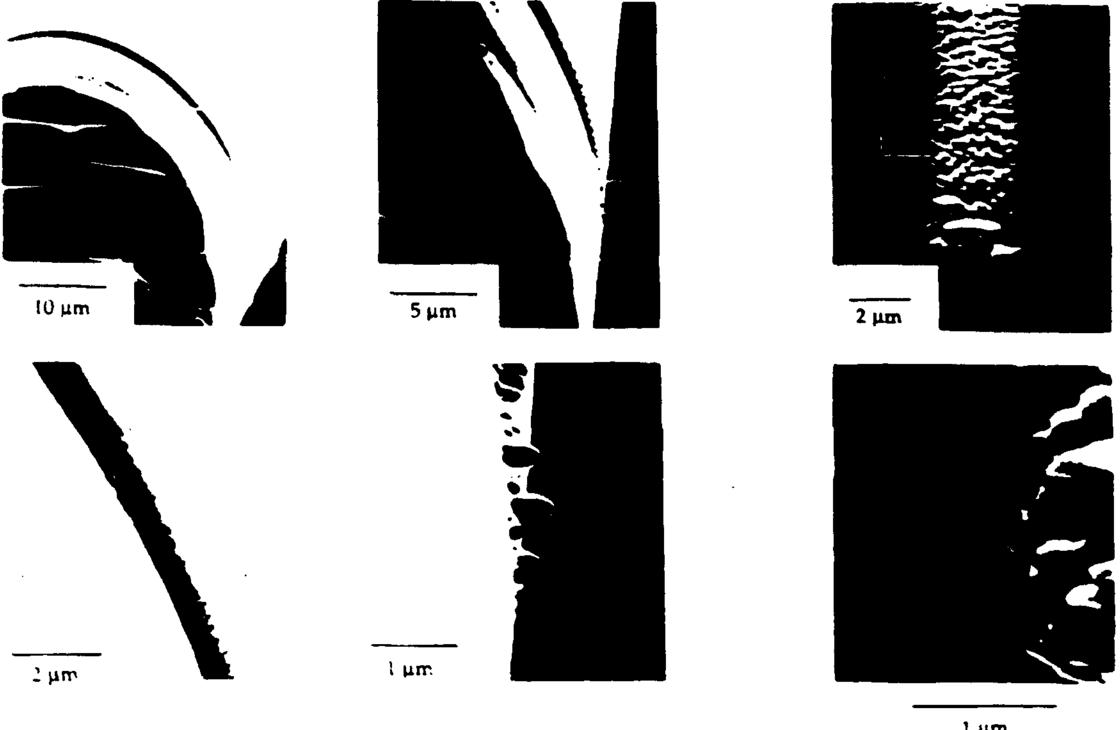

Fig. 12 From Ref. [7]. SEM micrographs of gold deposition on a quartz fiber (with the gas feed 20° off-axis). The four photos on the left-hand side show the end-on view of the fiber while the two on the right-hand side show the region of grazing incidence deposition (lower middle end view photo) viewed at normal incidence. A peculiar growth consisting of an array of protrusions is seen. The lower left-hand side photo shows the transition from smooth to ripply deposition at 50°. The deposition was carried out by scanning a 35 keV, 118 pA, Ga^+ ion beam over a rectangle of 82 μm x 1.8 μm for 50 min.

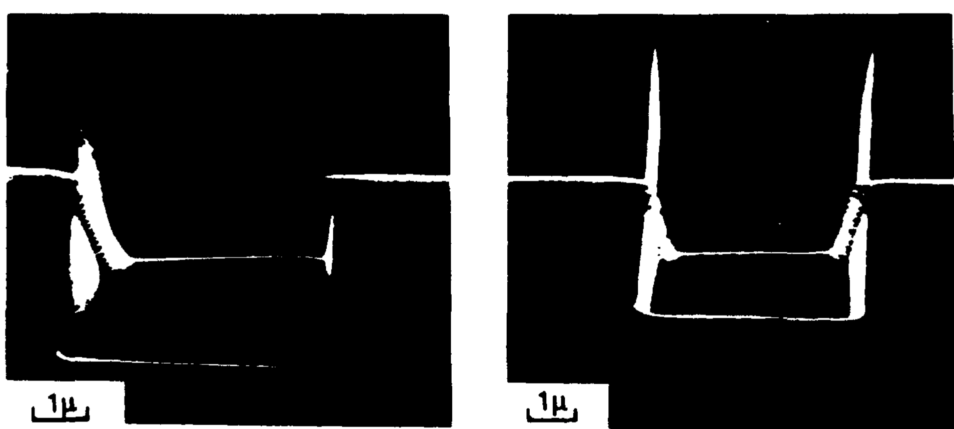

Fig. 13 From Ref. [7]. Tungsten line deposited over grooves in Si with steep sidewall angles showing comblike texture. The deposition conditions were 25 keV Ga^+ beam at 280 pA, $J_{av} = 9 pA/\mu m^2$, dwell time 0.3 μs and total scan time 2 min. The angles of incidence for the four walls with W deposition contained in (b)-(d) are ~ 40°, 75°, 85°, and 80°, respectively.

Another observation that may be related to the deposition in pits is the unwanted deposition on nearly features. If ion induced deposition is carried out near a neighboring high aspect ratio absorber line, material will be deposited on the side of this line even though the ion beam is not scanned there. This is illustrated in Fig. 14(a). The deposit on the facing feature is most likely due to the sputtering that occurs during deposition. This is supported by the fact that, when gold is used with a high deposition yield(~ 70) it shows much less unwanted growth of the neighboring feature than does tungsten Fig. 14(b) which has a low deposition yield (~ 1-2). In other words, at least 35 times more ions are needed to deposit the same quantity of absorber when tungsten is used than when gold is used. The amount of material sputtered and redeposited is proportional to the ion flux.

This focused ion beam process makes use of ion induced surface chemistry to produce deposition of material. The process can be reversed to produce ion assisted etching.

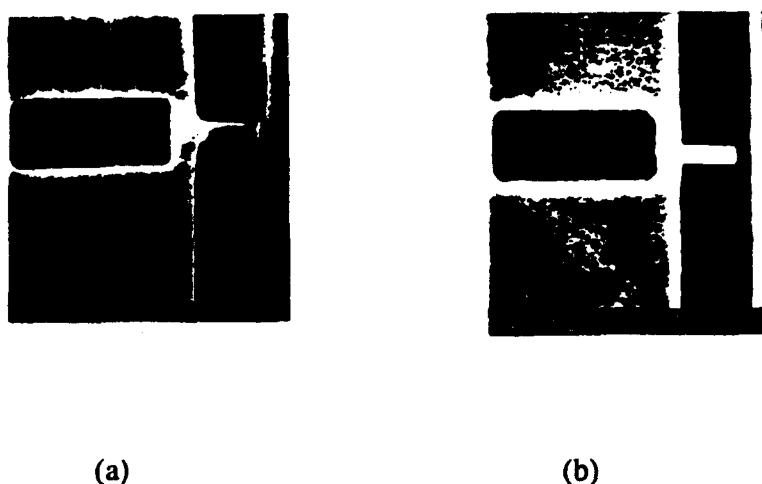

(a) (b)

Fig. 14(a), (b) From Ref. [29]. Simulated repair by deposition of a patch 2 x 0.5 μm extending from one existing gold feature on a mask toward the other. In (a) tungsten is deposited and extensive redeposition is seen. In (b) gold is deposited with much higher yield showing almost no redeposition.

ION ASSISTED ETCHING

In ion assisted etching a reactive gas is introduced such as Cl_2 or XeF_2 which by itself does not react with the substrate. However, at the point where the ion beam is incident a reaction takes place and material is removed at a rate 10 to 20 times faster than by sputtering alone. This has been demonstrated by a number of authors, largely by etching Si [38] and GaAs[39] but also SiO_2 and Si_2N_3[40] and Y-Ba-Cu-O [41]. For the repair of X-ray masks with plated gold absorbers, ion assisted etching is unlikely to work. Few materials react with gold to yield volatile reaction products.

However, if the absorber is made of tungsten the situation is more favorable. In fact, tungsten masks are patterned by reactive ion etching rather than plating and, although the state-of-the art is not as developed as in the case of gold, tungsten masks with stress free films are quite promising [42] [43].

A process for chemically assisted focused ion beam etching of the tungsten masks material has been demonstrated [44], [45]. A 20 beV Ga^+ ion beam was used together

with a XeF_2 gas. The gas pressure on the surface below the gas jet is of order several Torr while the pressure in the work chamber is of order 10^{-6} Torr [45]. The material removal rate is about 100 times faster than with ion milling alone.

The absorber film used consists of an underlying layer of 10 nm of Cr, then 300 nm of W followed by another layer of Cr 30 nm thick. Since there are reactive ion (plasma) etches such as mixtures $CBrF_3$ SF_6, which etch the W but not Cr this sandwich structure is used in the initial patterning of the mask, [42]. The same sandwich structure can be used to advantage in the repair. XeF_2 attacks W much faster than Cr under ion bombardment. Thus once the area to be removed has been defined in the Cr, the continued rapid chemically assisted focused ion beam etch of the W is found to have smoother sidewalls than pure milling alone [44], [45]. In addition, the effect of variable etch rate of different crystal grains which produces very rough bottoms of etched pits as shown in Fig. 3 is absent. In addition, chemically assisted milling eliminates the undesirable effects of material redeposition which may complicate focused ion beam milling, as discussed above.

However, since at the moment, Au masks still appear to be more widely used and have been used in most repair studies we will examine some examples of repair of actual X-ray masks.

MASK REPAIR

Milling

The repair of opaque defects, i.e. unwanted absorber, is accomplished by milling. The defect is observed on the CRT screen of the focused ion beam system. The ion beam is then programmed to scan over the defect and to deliver the dose needed to remove it. The required dose can be either calculated from the yield, Table I, or determined by direct calibration of the instrument. One can compensate for the variation in milling rate due to crystal grain orientation in Fig. 3 simply by overmilling. The membrane of the x-ray mask is made out of material such as Si or Si_3N_4 which mills much more slowly (see Table I) than gold, so that overmilling will not create significant pits in the membrane.

The redeposition during milling is more troublesome. For example, if one line in a closely spaced grating has a protruding defect which has to be milled off, there will be redeposition on the facing sidewall of the neighboring line. This can be, in turn, milled off. An example of this kind of milling is shown in Fig. 15.

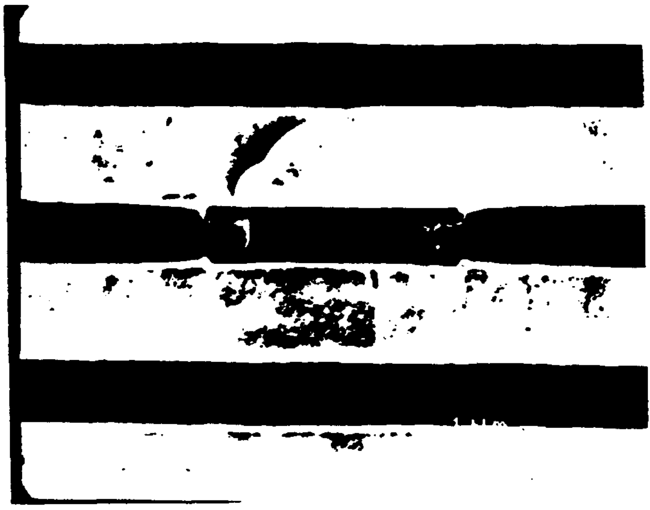

Fig. 15 From Ref. [37]. Defect which had been protruding from the upper central line into the 0.5μm wide space (black in photo) has been milled away and the redeposited material on the lower line has been "trimmed". The trimming in this case was not complete and some of the tails of the redeposit are still seen.

A possible way to minimize redeposition is to mill the interior of the defect first leaving a thin "wall" on the side facing the neighboring feature. If the wall is then milled off as the last step, the redeposition is reduced.

Another key requirement of mask repair is the placement accuracy. Usually a given feature edge has to be located to within a tolerance of $\pm$ 10% of the minimum linewidth. The ability to do this is determined by the control of the milling process and by the stability and imaging capability of the repair system. An example of precise edge alignment is shown in Fig. 16 .

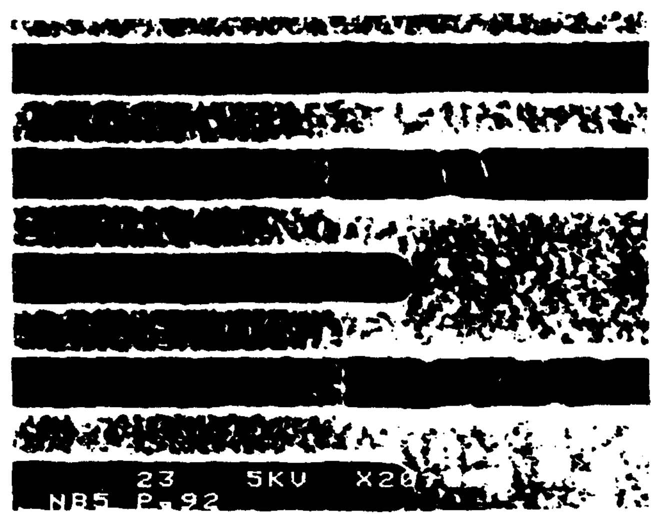

Fig. 16 From Ref. [2]. Illustrates the precise alignment of milled line, 0.5μm wide. The two lines that had originally extended only half way across the figure, as the center line still does, were extended to the right.

Deposition

Clear defects, i.e. missing absorber, are repaired by ion induced deposition. At this time gold appears to be the preferred material to deposit because of its high yield [29]. The deposition rate is determined by the average current density (beam current/area of feature to be deposited) and by the flux of precursor gas. In general, the growth rate increases with increasing current density up to the point where the flux of the adsorbate becomes comparable to the ion current density, and the adsorbate on the surface becomes depleted. Further increase in current density will cause the rate to drop sharply and, in fact, become negative i.e. milling becomes dominant. For example, for dimethylgold hexafluoroacetylacetonate at a pressure of 10 mTorr at the sample surface at room temperature the maximum deposition rate of 0.9 nm/sec was found at an average current density of 200 $\mu A/cm^2$. Ref. [11].

The high deposition yield of gold minimizes unwanted deposition due to resputtering as discussed above, see Fig. 14, Ref. [29]. Of course, in this case also as in milling the unwanted deposition (such as in Fig. 14(a)) can be milled off. This is illustrated in Fig. 17, where trimming was used after deposition.

As in milling, precise placement accuracy or edge location is required. An example of edge reconstruction is shown in Fig. 18. The patch is, for lithography purposes, indistinguishable from the original line.

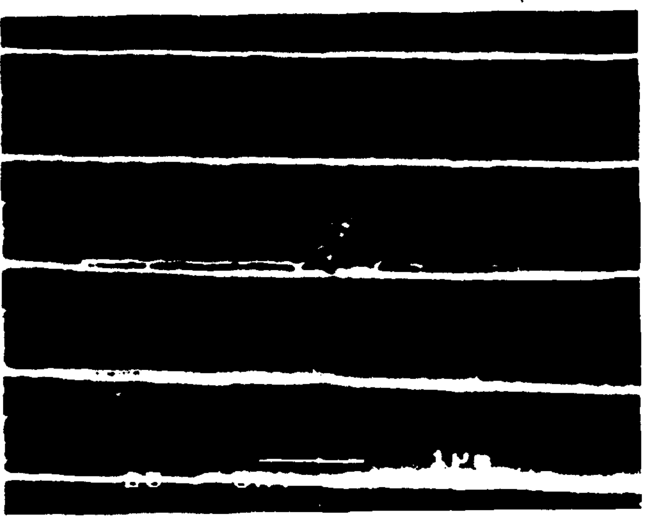

Fig. 17 From Ref. [37]. Bottom two gold lines of an x-ray mask had tungsten patches deposited on them to repair defects. Trimming was used to remove redeposited material from the adjacent features.

Fig. 18 From Ref. [29]. On left, indentation in gold mask line filled in by ion induced deposition of gold. The indentation had been 0.25 μm wide (as the unfilled indentation above it still is). On right, the same pattern printed in resist. The good alignment capability is evident.

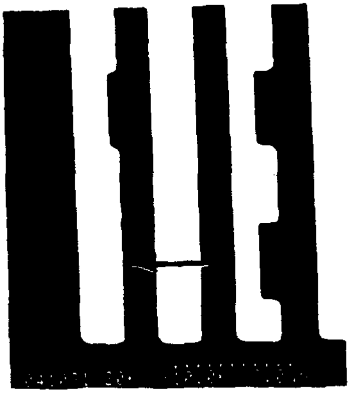

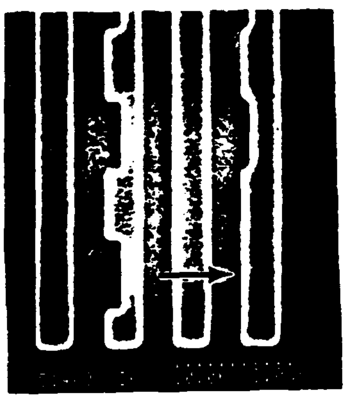

X-ray Opacity of Deposited Repairs

Over the wavelength range from 8-15Å the x-ray attenuation of pure W is slightly lower than that of pure Au and Pt, i.e. to achieve the same attenuation a W mask would need to be about 20% thicker than Au or Pt.

The material produced by ion induced deposition contains large quantities of impurities, mainly C and some Ga. The high yield "gold" repair material most extensively tested was about 50% carbon [29]. Its x-ray attenuation is, of course, equal to that of pure gold half as thick. Various repair thicknesses of "gold" have been tested at IBM and compared to the plated mask absorber which is 0.6 μm thick pure gold. The tested features were 0.5 μm wide isolated lines, lines and spaces, and isolated spaces the repair thickness that printed most like the original mask in terms of the line width measured in resist was the repair that was 0.47 μm thick [29]. This measurement was carried out for a dose 1.2 times the minimum dose needed for exposure. The suggested explanation for this counter intuitive result is that the features deposited, some of which are shown in Fig. 9, have a small "foot" of gold at the base [29]. This alters the x-ray intensity distribution in the resist so that the effect of the reduced opacity is compensated. Perhaps this can be called an x-ray phase shift mask. While this is a favorable and interesting result, these repairs are not ideal. As the authors point out [29] at large overexposures they will not print. In fact, if these repairs were ideal why not make the entire mask with 0.3 μm thick gold rather than 0.6 μm?

SUMMARY AND SOME UNRESOLVED ISSUES

The main steps of x-ray mask repair, namely absorber removal and reconstruction, have been demonstrated using focused ion beam milling and ion induced deposition. In milling the effects of redeposition, the grain structure of the absorber material, and the yield variations as a function of angle of incidence need to be taken into account. By ion induced deposition the high aspect ratio features needed can be achieved. The x-ray opacity of these deposits is reduced by the high (~ 50 at %) carbon content, but this does not appear to seriously impair their "printability" in resist.

Although the needed steps for x-ray mask repair have been demonstrated, the processes are by no means ideal or mature. A number of material science issues remain to be resolved, such as:

1. The microchemistry at the point of ion impact is not known. What are the reaction products?

2. How can the carbon content be reduced for room temperature growth?

3. The mechanism for forming the high aspect ratio deposits characterized by vertical sidewall and a "foot" at the base is puzzling given that the beam profile is gaussian.

4. Except for measurements of the surface pressure vs. capillary tube height [11] the details of the gas feed have not been studied. Does the absorbate diffuse along the surface toward the point where the ion beam is incident?

Research that answers some of these or other questions will no doubt help to improve the x-ray mask repair process.

Acknowledgments:

The author is grateful to Dr. Patricia G. Blauner of IBM Yorktown and Dr. Diane K. Stewart of Micrion for providing a number of figures for this paper and for many enlightening discussions, and to Dr. Stephan Slemmer of U. California Berkeley for discussions of surface chemistry during a chance encounter on Mt. Tamalpais. Although the writing of this review was not directly sponsored, the author's work in areas related to x-ray mask repair is, or has been, sponsored by DARPA/NRL under a subcontract from Micrion, by ARO, and by NSF.

References

[1] Electron beams have also been considered for x-ray mask repair, at least for deposition. See for example, W. Brünger, Microcircuit Engineering 9, 171 (1989). However, material removal especially of gold is more difficult. Tungsten removal by electron beam induced etching in the presence of a reactive gas might be feasible.

[2] D.K. Stewart, Micrion Corp. Private communication.

[3] G.M. Atkinson, F.P. Stratton, and R.L. Kubena, J. Vac Sci. Technol. B10, 3104 (1992).

[4] See for example: J.M. Chabala, R. Levi-Setti, and Y.L. Wang, J. Vac. Sci. Technol. B6, 910 (1988) or L.R. Harriott, and M.J. Vasile, J. Vac. Sci. Technol. B7, 181 (1989). Incidentally, SIMS can also be used for end-point detection.

[5] Focused ion beam imaging can be used to see crystal grains: K. Nikawa, J. Vac. Sci. Technol. B9, 2566, (1991); D.L. Barr, L.R. Harriott, and W.L. Brown, J. Vac. Sci. Technol. B10, 3120 (1992). See also Ref. [13].

[6] H.H. Anderson, and H.L. Bay "Sputter Yield Measurements" in Sputtering by Particle Bombardment I, Physical Sputtering of Single Element Solids", R. Behrisch ed. Springer Verlag (Berlin-Heidelberg 1981) p. 145.

[7] X. Xu, A.D. Della Ratta, J. Sosonkina, and J. Melngailis, J. Vac. Sci. Technol. B10, 2675 (1992).

[8] H. Yamaguchi, J. De Physique Colloque C6, Suppl. no. 11, tome 48 (Nov. 1987) p. C6-165.

[9] J.G. Pellerin, G.M. Shedd, D.P. Griffis, and P.E. Russell, J. Vac. Sci. Technol. B7, 1810 (1989).

[10] K.P. Müller and H.C. Petzold, SPIE Vol. 1263, 12 (1990).

[11] P.G. Blauner, Y. Butt, J.S. Ro, and J. Melngailis, J. Vac. Sci. Technol. B7, 609 (1989).

[12] J. Melngailis, C.R. Musil, E.H. Stevens, M. Urlaut, E.M. Kellogg, R.J. Post, M.W. Geis, and R.W. Mountain, J. Vac. Sci. Technol. B4, 176 (1986).

[13] A. Wagner, J.P. Levin, J.L. Mauer, P.G. Blauner, S.J. Kirsch, and P. Longo, J. Vac. Sci. Technol. B8, 1557 (1990).

[14] T. Ishitani and T. Ohnishi, Japn J. of Appl. Phys. 28, L320 (1989), also J. Vac. Sci. Technol. A9, 3084 (1991).

[15] K.P. Müller, Japan. J. Appl. Phys. 28, 2348 (1989).

[16] A.D. Dubner, A. Wagner, J. Melngailis, and C.V. Thompson, J. Appl. Phys. 70, 665 (1991).

[17] A.D. Dubner, Ph.D. Thesis MIT (1991).

[18] J.S. Ro, C.V. Thompson, and J. Melngailis (in preparation).

[19] J.S. Ro, Ph.D. Thesis MIT (1992).

[20] Z. Xu T. Kosugi, K. Gamo, and S. Namba, J. Vac. Sci. Technol. B7, 1959 (1989).

[21] K. Gamo and S. Namba, Proc. 1989 Intern. Symp. on MicroProcess Conf. p. 293.

[22] D.K. Stewart, L.A. Stern, and J.C. Morgan, SPIE Symp. Proc. "Electron Beam X-ray and Ion Beam Technologies: Submicrometer Lithographies VIII" (Mar. 1989) Vol. 1089, p. 18.

[23] T. Tao, W. Wilkinson and J. Melngailis, J. Vac. Sci. Technol. B9,162 (1991).

[24] Y. Madokoro, T. Ohnishi, and T. Ishitani, Riken Conf. Mar. 1989.

[25] P.G. Blauner, J.S. Ro, Y. Butt, C.V. Thompson, and J. Melngailis, Mat. Res. Symp. Proc. Vol. 129, p. 483 (1989).

[26] T. Tao, J.S. Ro, J. Melngailis, Z. Xue, and H. Kaesz, J. Vac. Sci. Technol. B (Nov/Dec 1990). Also T. Tao private communication.

[27] D.K. Stewart, L.H. Stern, G. Foss, G. Hughes, P. Govil, SPIE Vol. 1263, p 21 (1990).

[28] D.K. Stewart and J.A. Doherty, 10th Annual Symp. on Microlithography Vol. 1496, p. 247 (Sept. 26, 27, 1990).

[29] P.G. Blauner, A.D. Dubner, and A. Wagner, SPIE Symp. (San Jose, CA Mar. 1993) to be published.

[30] Y. Takahashi, Y. Madokoro, and T. Ishitani, Japn J. Appl. Phys. 30, 3233 (1991).

[31] J.S. Ro, A.D. Dubner, C.V. Thompson, and J. Melngailis, Mat. Res. Soc. Symp. Proc. Vol. 101 p. 255 (1988).

[32] P.G. Blauner, J.S. Ro, Y. Butt, C.V. Thompson, and J. Melngailis, Mat. Res. Soc. Symp. Proc. Vol. 129 p. 483 (1989).

[33] A.D. Dubner and A. Wagner, J. Vac. Sci. Technol. B7, 1950 (1989).

[34] J.S. Ro, C.V. Thompson, and J. Melngailis (in preparation).

[35] T. Tao, W. Wilkinson, and J. Melngailis, J. Vac. Sci. Technol. B9, 162 (1991).

[36] D.K. Stewart, J.A. Morgan, and B. Ward, J. Vac. Sci. Technol.B9, 2670 (1991).

[37] D.K. Stewart, T. Olson, W. Ward, SPIE Symp. (San Jose, CA 1993) to be ..blished.

[38] Y. Ochici, K. Gamo, S. Namba, K. Shihoyama, A. Jasuyama, T Shiokawwa, and K. Toyoda. J. Vac. Sci. Technol. B5, 4223 (1987).

[39] M. Komuro and H. Hiroshima. J. Vac. Sci. Technol. B9, 2656 (1991).

[40] Z. Xu, K. Gamo, and S. Namba. J. Vac. Sci. Technol. B6, 1039 (1988).

[41] S. Matsui, N. Takado, H. Tsuge, and K. Asakawa. Appl. Phys. Lett. 52, 69 (1988).

[42] G.K. Celler, L.E. Trimble, J. Frackoviale, C.W. Jurgensean, R.R. Kola, A.E. Novembre, and G.R. Weber. Appl. Phys. Lett. 59, 31105 (1991).

[43] Y.C. Ku, L.P. Ng, R. Carpenter, K. Lu, H.I. Smith, L.E. Haas, and I Plotnik. J. Vac. Sci. Technol. B9, 3297 (1991)

[44] R.R. Kola, G.K. Celler, and L.R. Harriott. Proc. of MRS, Symp. A. Beam-Solid Interactions: Fundamentals and Beam applications (Boston, Nov. 30 - Dec. 4, 1992) to be published.

[45] L.R. Harriott, R.R. Kola, and G.K. Celler. Proc. of SPIE, Electron-Beam, X-ray and Ion Beam Submicrometer, Lithographics for Manufacturing III (San Jose Feb. 28-Mar. 5, 1993) to be published.

Mechanism of Ion Beam Induced Deposition of Gold

J.S. Ro[1], C.V. Thompson and J. Melngailis

Research Laboratory of Electronics
Massachusetts Institute of Technology

Abstract

Ion beam induced deposition is a novel method of thin film growth in which adsorbed, metal-bearing molecules are decomposed by incident energetic ions leaving a deposit. In conjunction with finely focused ion beams this process is used in microelectronics for local repair, i.e. deposition of patches of metal film with better than 0.1 μm resolution. Each ion can decompose as many as 40-50 adsorbed molecules. We have studied the fundamental aspects of this process, namely how is the energy of the ion transferred to adsorbed molecules over a radius of up to 5 nm. The decomposition yield (number of molecules decomposed/ion) was measured for Ne, Ar, Kr, and Xe ions at 50 and 100 keV. A model based on TRIM calculations was developed. The data correlates with this model confirming the view that collision cascades which can provide energy to surface atoms over a substantial area are responsible for ion beam induced deposition. Preliminary results (calculated and measured) are also presented for yield as a function of angle of incidence.

To be published J. Vac. Science and Technology

[1] Present address: Hongik University, Seoul, Korea 121-791

Introduction

Patterned thin films are the building blocks of microelectronic devices. Usually they are produced in a two step process consisting of deposition and of lithography. Processes which combine patterning and deposition in one step are useful for local repair of masks and integrated circuits and may also be of interest for in-situ processing. Such processes have been demonstrated with lasers,[1] electron beams,[2-5] and ion beams and can be thought of as radiation induced localized chemical vapor deposition (CVD). Most often an ambient of a metal organic or metal halide gas is produced on the surface and the radiation induces chemical reaction where it is incident on the surface.

Ion beam induced deposition has in fact proved to be commercially useful for repair processes because the beam can be focused down to 0.05 μm dimensions and below and because the same tool can be used to sputter off material with submicrometer precision simply by turning off the gas ambient. This material addition and removal is used for photomask repair[6-9] and integrated circuit repair[10] [11] [12] and is being developed for x-ray lithography mask repair.[13] [14] Impressive deposition results have been demonstrated including gold lines of 0.1 μm width,[15] high aspect ratio structures,[13] and low resistivity deposits.[16] [17] In spite of the large number of materials that have been deposited, (for a tabulation, review and references see Ref. 18 or 19) the atomic mechanism of ion beam induced deposition has only very recently been addressed. (Refs. 20, 21, 22). In this paper we will present results of measurements of ion beam induced deposition rates of gold with noble gas ions at 50 and 100 keV. These results, as well as measurements in the range of 2-10 keV (Ref. 20), indicate that ion beam induced deposition is substrate mediated and that it can be modeled by collision cascade process in a way that is similar to the successful models of ion sputtering.[23]

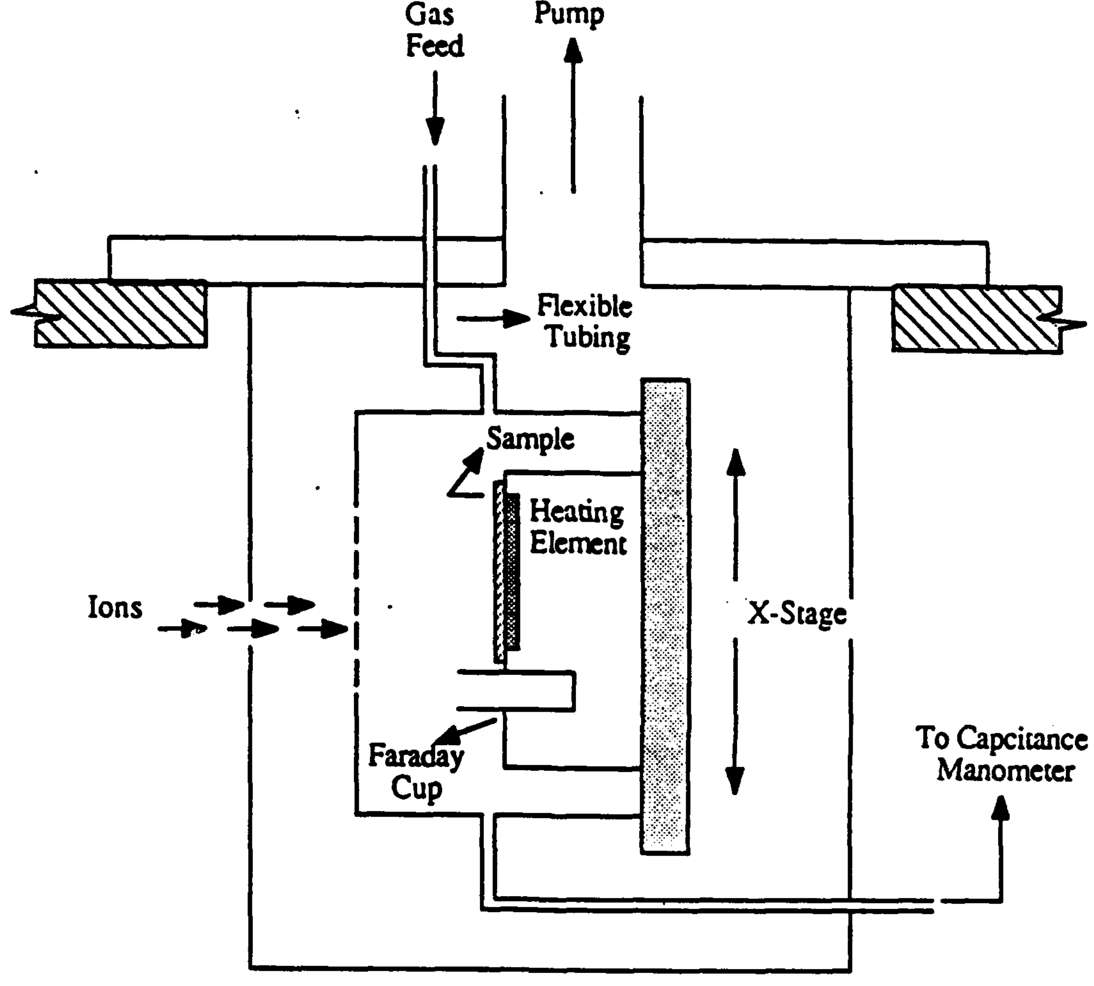

Figure 1: Schematic of experimental setup for ion beam induced deposition using a pressure cell.

Experimental

Although in most of the practical applications of focused ion beam induced deposition Ga^+ ions are used, we chose to study the mechanism of the process using noble gas ions. This choice provides a large range of ion masses and energies, and our earlier results indicate that there is no apparent difference in the microstructure, composition, or relative deposition rate between Ga^+ ions and noble gas ions, in particular Ar^+, the nearest in mass to Ga^+. (Refs. 15, 16, 24, 25).

The precursor gas used to deposit gold was dimethylgold hexafluoroacetylacetonate, $C_7H_7F_6O_2$ Au, abbreviated as DMG (hfac). It is liquid at room temperature with a vapor pressure of 350 mTorr, and was purchased from American Cyanamid Corp.

A special chamber was constructed for the end station of a low-current, research type ion implanter. See Fig. 1. It had a 3 mm diameter hole facing the beam and was separately pumped with a turbomolecular pump to minimize contamination of the implanter by the precursor gas. The sample on which deposition was carried out was further enclosed in a cell which created the local gas ambient. This cell had six-1 mm-diameter holes, and it could be displaced to expose each of these holes in turn to the beam. A Faraday cup was located behind one of the holes to measure the ion current. Thus 5 depositions could be carried out in one loading of the sample. The ion current density on the sample was in the range of 0.7 to 7 $\mu A/cm^2$. The deposition yield (atoms deposited per incident ion) was independent of current density in this range. A capacitance manometer was connected to the gas cell. The depositions were carried out at a pressure of 1 mTorr. The samples were pieces of SiO_2-coated Si wafer. A 50-μm-period grating was lithographically exposed in photoresist. After deposition the resist was

dissolved in acetone leaving 25 μm wide stripes of gold. The thickness of the deposited gold was measured with a surface profilometer. To measure the sputtering rate of the grown films the sample was displaced slightly so that half of the grown area was exposed to the ion beam. The gas supply was then turned off and part of the film was sputtered away. The composition of the film was measured by Auger electron spectroscopy. The film microstructure was examined by transmission electron microscopy using a JEOL-200CX TEM operated at 200 kV. For plan-view TEM samples, a back etching technique was used. Films were deposited on the thermally grown SiO_2 on the silicon wafer. The sample was scribed and broken into 2x2 mm squares and it was then placed face down on a microscopic glass slide and melted white wax was used to cover the sample except for a small window in the center of the sample. Droplets of an acid solution (1:1 HF-HNO_3) were then applied to the window using a capillary tube. Cross sectional transmission electron microscopy was also used to investigate various stages of film growth in ion beam induced deposition. For this sample cross sections were thinned by standard grinding and ion milling techniques.

Results

The microstructure of the films will be discussed in more detail elsewhere,[26] but we mention some of the results here since they pertain to the model. For growth at room temperature with relatively light ions the films contain up to 50 atomic % of carbon. The early stages of growth is found to take place in islands of polycrystalline gold 20-50 nm in diameter imbedded in a background of carbon.[24] At later stages this growth becomes columnar. Films grown on a heated substrate (~ 120°C) had a normal, continuous polycrystalline microstructure. Rings in the electron diffraction pattern, were

observed in all cases which indicates that the films consist of randomly oriented crystals of gold. The carbon is presumed to be amorphous. Because of the apparent separation of the film into two separate materials, the deposition or sputter yield of gold (atoms deposited or sputtered per incident ion) was calculated by multiplying the film thickness (grown or sputtered) by the volume fraction of gold. This scaled thickness was then used to calculate the yield of sputtered or deposited gold. The assumptions implicit in this scaling can be debated, but, since we are mainly seeking to establish trends and correlations, the conclusions should not be affected.

The thickness of the film deposited was observed to be directly proportional to the dose, and independent of pressure of the DMG (hfac) gas in the range of 0.1 to 3 mTorr and of current density from 1.5 to 10 $\mu A/cm^2$. These results are as expected since the flux of gas molecules on the surface is many orders of magnitude higher than the flux of ions, and since earlier results[27] of gas adsorption on a quartz crystal microbalance indicate that a constant thickness (presumably a monolayer) is adsorbed over this pressure range at room temperature and above.

Each incident ion causes a number of adsorbed molecules to dissociate and also causes a number of substrate atoms to be sputtered off. The net growth is a result of the competition between these two effects. Thus one can write that

$$Y_N = Y_D - Y_S$$

where Y_N is the number of atoms deposited per incident ion, Y_S is the number of atoms sputtered per incident ion and Y_D is the number of molecules decomposed by the ion.[16] [27] This expression has been verified by measuring the net yield Y_N as a function of the density of adsorbed molecules.[27] The results obtained for the yields are given in Table I. For

comparison we have also measured the sputter yield of pure, electron-beam-evaporated, gold films. As seen in Table I the sputter yield is about a factor of 2 to 3 higher for the pure films than for the carbon containing films grown by ion beam induced deposition. The presence of carbon, as expected, lowers the sputter yield.

Following earlier work on Pt deposition[12] we have also measured the ion beam induced deposition rate as a function of angle of incidence. This was done by depositing on thin, round pyrex fibers and determining the thickness of the deposit vs. angle by examining the cleaved fibers in an SEM. These preliminary results will be discussed in connection with the modeling.

Mechanism of ion beam induced deposition

The first main question in understanding the IBID process is to define the reaction zone where decomposition of molecules is taking place. In principle, decomposition may take place either in the gas phase or on the surface. The cell pressure was varied, by a factor of 30, from 0.1 to 3.0 mTorr. Experimental results shows that the yield is insensitive to the pressure over the ranges investigated. If decomposition in the gas phase were dominant, the yield would be proportional to the pressure. This indicates that the substrate surface is the dominant decomposition reaction zone in IBID. Since the adsorbed molecules of DMG (hfac) are found to form a monolayer under room temperature deposition conditions,[27] we can calculate the radius surrounding the point of incidence within which all of the molecules would have to be decomposed given the measured values of Y_D. This radius can be as high as 45Å for 100 keV Xe ions. (If not all molecules within the interaction area are decomposed, the radius of the interaction area would, of course, be larger). The questions we wish to address is what is the mechanism by which an incident ion can cause a molecule 45Å from the point of

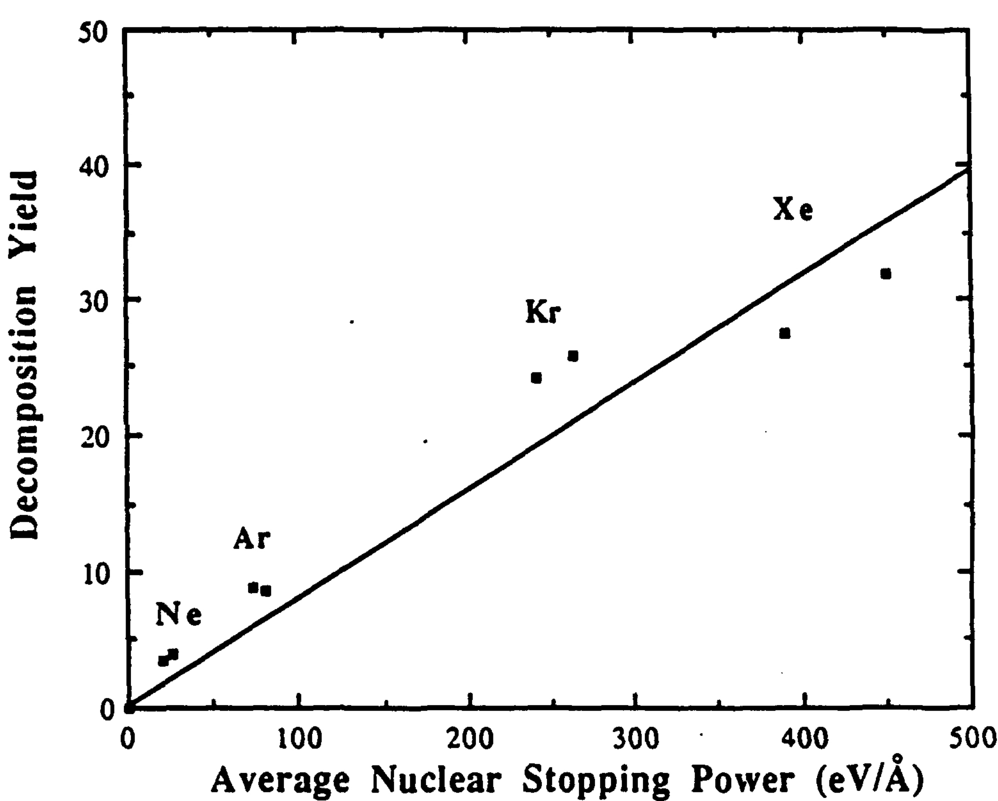

Figure 2: Decomposition yield as a function of average nuclear stopping power for different ion species and energies. Decomposition yield is the sum of the measured net deposition yield and the measured sputtering yield. Films were deposited at room temperature and 1.0 mTorr of DMG(hfac). For each ion species, two different energies; 50 and 100 keV, were used for deposition.

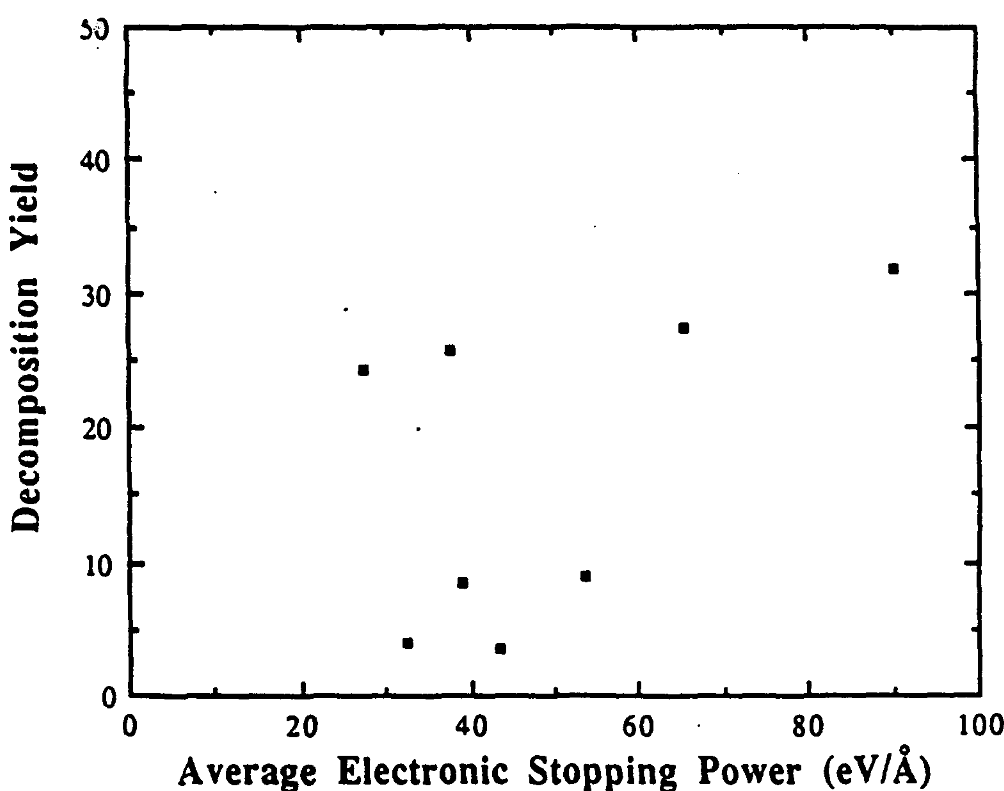

Figure 3: Decomposition yield as a function of average electronic stopping power. Decomposition yield is the sum of a measured net deposition yield and a measured sputtering yield. Each data point for stopping power represents a combination of each ion species and energy (see Table 5.3). Films were deposited using Ne^+, Ar^+, Kr^+, and Xe^+ at 50 and 100 keV each, and at room temperature and 1.0 mTorr of DMG(hfac).

incidence to decompose. Simple cross section arguments indicate that neither direct ion-molecule collisions on the surface nor ion-molecule collisions in the gas above the surface can account for the yield. Thus the mechanism most likely includes the substrate-ion interaction. Incident ions lose their energy by collisions with the nuclei of the substrate or by interaction with the electron gas of the substrate. The energy loss rates per unit depth of penetration is described by a nuclear stopping power S_n and an electronic stopping power S_e. Since films deposited using various ion species and energies are not pure, stopping powers of pure elements may not be used. Microstructural observation of these films confirmed that gold islands are embedded in a matrix of amorphous carbon. Electron diffraction pattern of these films showed ring patterns, indicating that the gold grains are randomly oriented polycrystals. Therefore, the microstructure of deposited films consists of a mixture of randomly oriented polycrystalline gold and amorphous carbon. From this observation, it is reasonable to assume that an incoming ion sees pure gold and pure carbon separately along its path. Based on these results, we have calculated stopping powers of IBID films for the ions and energies used by using a weighted sum of the stopping powers of pure Au and pure C and using atomic concentrations of the films and have plotted in Fig. 2 and 3 respectively the decomposition yield Y_D vs. the stopping powers. The results indicate that the decomposition yield is much better correlated with energy loss to the nuclei than with energy loss to the electrons. Thus a purely electronic mechanism for the dissociation is unlikely. Incidentally, the sputter yield of pure gold also correlates with the nuclear stopping power and not the electronic stopping power.[22]

The mechanism we propose, which has been already verified at lower energies,[20] [21] is based on collision cascades. The incident ion scatters lattice

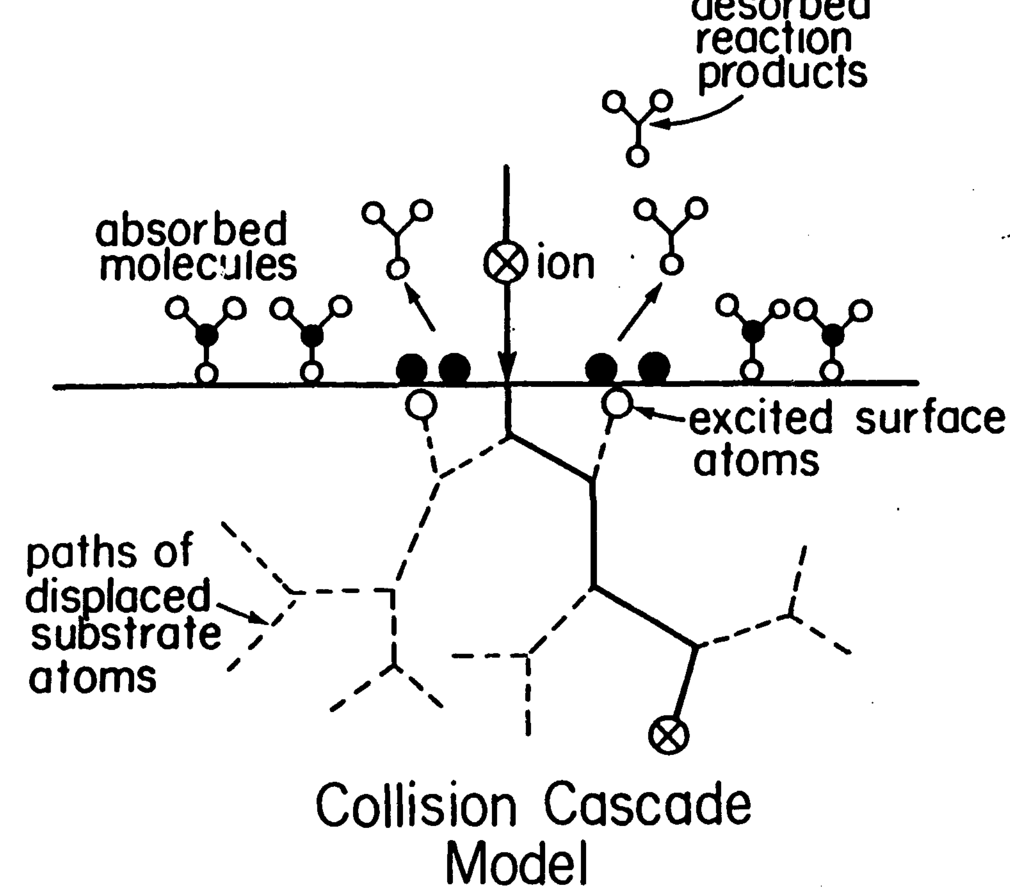

Figure 4: Schematic of the collision cascade process of surface adsorbate decomposition.

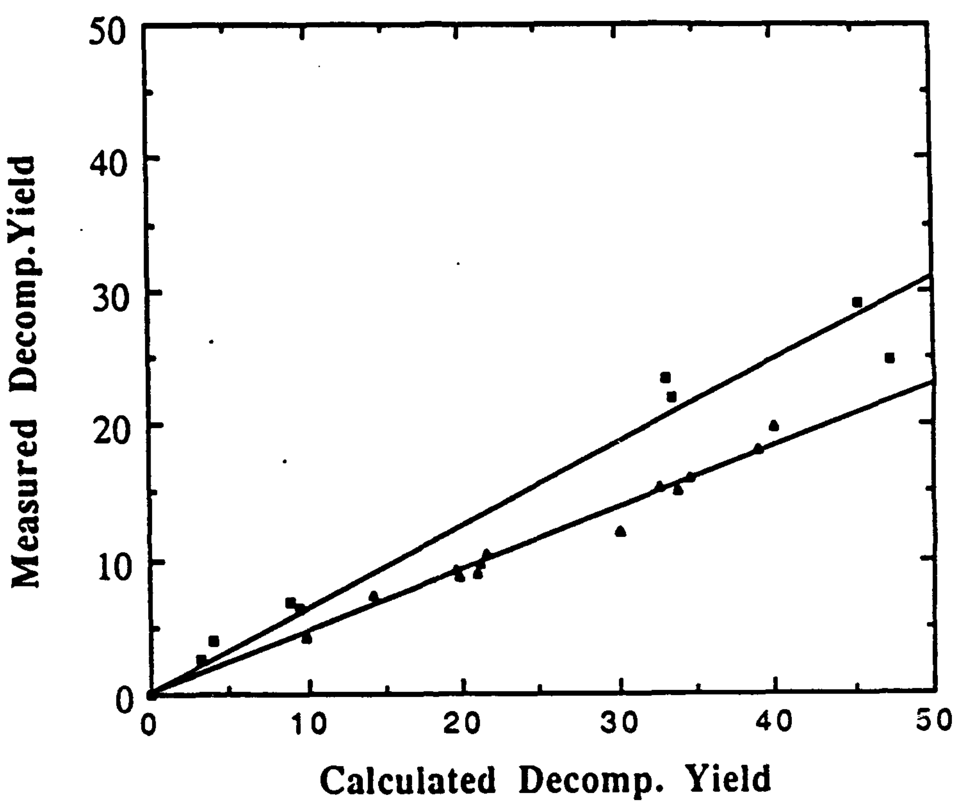

Figure 5: Measured decomposition yield vs. calculated decomposition yield for the higher energies (50 & 100 keV), square symbols, and the lower energies (2-10 keV), triangular symbols, measurements of ref. 20. The calculated values were all obtained as described in the text. Both sets of data are seen to lie on straight lines (slopes 0.47 & 0.62). The difference in slope is likely due to the differences in measurement techniques. At low energies the mass of the film was measured on a quartz crystal microbalance (ref. 20) and it was assumed to be pure gold. At the high energy (this work) thickness was measured with a profilometer, and the yield was corrected for carbon content.

atoms, some with enough energy to, in turn, scatter other lattice atoms producing the collision cascades. Some of these cascades reach the surface imparting energy to the surface atoms. (See Fig. 4) If this energy is high enough to remove surface atoms (the surface binding energy is 3.8 eV in the case of gold), sputtering occurs. If the energy is above the dissociation energy of the adsorbate (0.95 eV ref. 28), then the adsorbed molecules can break up leading to deposition of gold (and carbon).

We will assume for simplicity that all surface atoms which attain an energy above 0.95 eV will decompose an adsorbed DMG (hfac) molecule. This probably overestimates the decomposition yield because the energy transfer from a substrate atom to the adsorbed molecule may not be complete. One can treat the energy transfer by a colliding-billiard ball model.[21] The effect of the surface-atom/adsorbate interaction introduces a multiplying factor in Y_D which is the same for all ion species and energies. Since we are interested in the relative magnitude of the decomposition yield and since this energy transfer will introduce only a scaling factor, we will ignore it and consider that every surface atoms that attains an energy in excess of 0.95 eV will decompose an adsorbed molecule.

The energy distribution of surface atoms surrounding the point of ion impact was calculated using the TRIM-SP code[29] and from this the decomposition yield Y_D was obtained. Since the substrate is a mixture of gold and carbon, Y_D was calculated separately for DMG (hfac) adsorbed on carbon and adsorbed on gold, and the two results were weighted according to the composition of the substrate. Since the grown film is made up of separate areas of pure gold and pure carbon this is a reasonable procedure.

The measured Y_D is plotted vs. the calculated Y_D in Fig. 5, for all of the ion species and ion energies available, including the earlier low energy

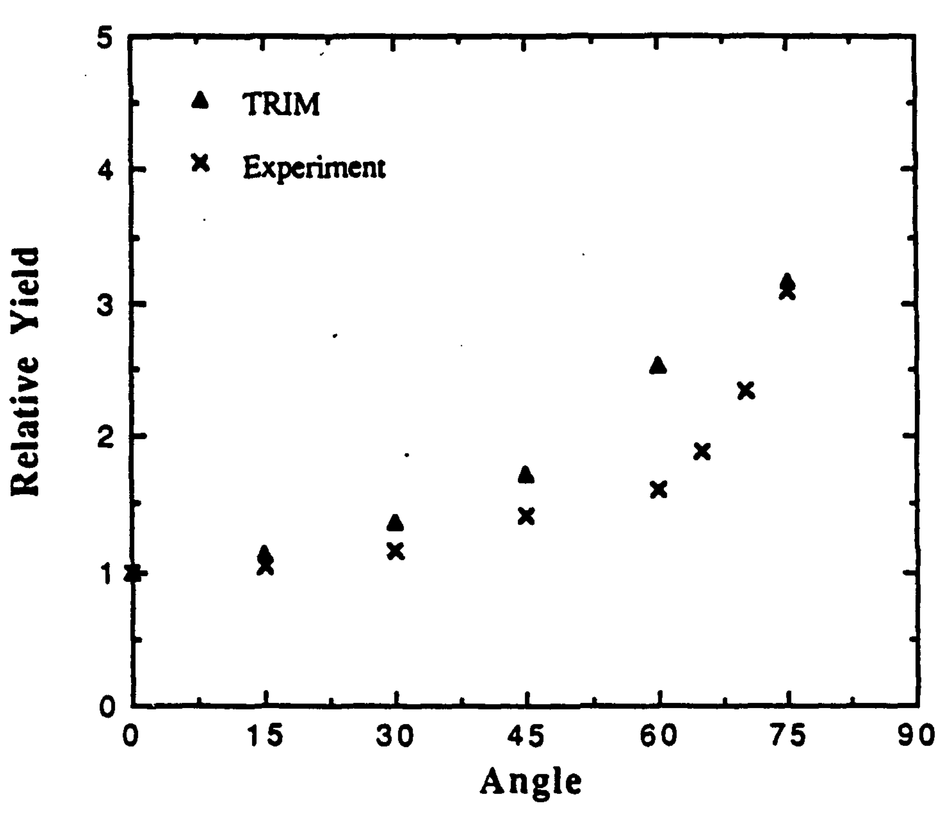

Figure 6: Relative yield as function of angle of incidence.

data.[20] The good correlation between measured and calculated values supports the collision cascade model of ion induced deposition. The fact that the slope of the curve is less than one instead of unity is unimportant. As discussed above somewhat different assumptions concerning the energetic-substrate-atom/adsorbate interaction would scale all of the data changing only the slope.

The collision cascade model predicts that as the angle of incidence goes from normal toward glancing the yield should go up. The number of collision cascades terminating on the surface will clearly increase on purely geometric grounds. We have calculated the relative decomposition yield for Xe^+ ions at 100 keV as a function of angle. The results are plotted in Fig. 6. We have also measured the net yield Y_N by depositing on a glass fiber and measuring the thickness of the deposit as a function of angle. Because we have not as yet measured the sputtering yield as a function of angle, we do not have Y_D as a function of angle. So a direct comparison cannot be made. Note, nevertheless that the relative dependence of measured $Y_N(\theta)/Y_N(o)$ is similar to the calculated $Y_D(\theta)/Y_D(0)$. A similar trend was also observed by focused ion beam induced deposition of Pt over a cylinder.[12] Ion beam induced deposition at non-normal incidence is important in the practical applications of this technique. In both circuit repair and, particularly, x-ray mask repair, deposition is often over severe topography. More detailed measurements of deposition and sputtering as a function of angle of incidence for Ga^+ ions from a focused ion beam have recently been carried out (30).

Summary

Measurements have been made of the ion beam induced deposition yield of gold from dimethylgold hexfluoroacetylacetonate for noble gas ions

from Ne to Xe at energies of 50 and 100 kV. The results correlate with a collision cascade model of the process. Preliminary results are also presented for deposition as a function of angle of incidence.

Acknowledgments

The authors wish to thank Patricia G. Blauner and Andrew D. Dubner for valuable discussions, and Nicole Herbots for help with the TRIM-SP program operation. Libby Shaw performed the Auger analysis and Jim Carter, Richard Perilli and Tim McClure provided technical help. The work was supported by the Army Research Office Contract no. DAAL-03-90-G-0223 and by the Naval Research Laboratory Contract no. 00014-89-2238 under a subcontract from the Micrion Corp.

Table I. Effect of ion species and energies on the decomposition yield and film purity. Decomposition yield was calculated by summing a measured net deposition yield and a measured sputtering yield. Films were deposited at 1.0 mTorr and room temperature. For comparison the measured sputter yield of pure gold is also included in parentheses.

Ion	Energy	J	Purity	Y_N	Y_S	Y_S	Y_D
	keV	Current Density ($\mu A/cm^2$)	(% Au)	(Au atoms per ion)	(Au atoms per ion)	(Pure Au)	(Au atoms per ion)
Ne	50	2.6		2.3	1.7	(4)	4.0
	100	4.2	40%	2.2	1.2	(3.5)	3.4
Ar	50	3.4		5.5	3.1	(8.8)	8.6
	100	5.0	45%	4.7	4.2	(9.2)	8.9
Kr	50	3.0		6.2	18.0	(29)	24.2
	100	5.5	80%	7.0	18.7	(35)	25.7
Xe	50	3.6		7.7	19.6	(45)	27.3
	100	5.4	80%	10.6	21.3	(52)	31.9

References

1. For a review of laser induced deposition see for example, D.J. Ehrlich and J.Y. Tsao, J. Vac. Sci. Technol. B1, 969 (1983) and D. Bauerle "Chemical Processing with Lasers" Springer Series in Materials Science 1 (1986).

2. W. Brunger, Microcircuit Engineering 9, 171 (1989).

3. S. Matsui and K. Mori, J. Vac. Sci. Technol. B4, 299 (1986).

4. R.R. Kunz and T.M. Mayer, J. Vac. Sci. Technol. B6, 1557 (1988).

5. H.W.P. Koops, R. Weiel, D.P. Kern, and T.H. Baum, J. Vac. Sci. Technol. B6, 477 (1988).

6. A. Wagner, Nucl. Instr. and Methods 218, 355 (1983).

7. J.R.A. Cleaver, H. Ahmed, P. Heard, P. Prewitt, G. Dunn, and H. Kaufman, Microelectron. Eng. 3, 253 (1985).

8. N.P. Economou, D.C. Shaver, and B. Ward, SPIE 733, 201 (1987).

9. M. Yamamoto, M. Sato, H. Kyogoko, K. Aita, Y. Nakagawa, A. Yasaka, R. Takasawa, and O. Hattori, SPIE 632, 97 (1986).

10. T. Ishitani, Y. Kawanami, and H. Todokoro, Jpn. J. Appl. Phys. 24, L133 (1985).

11. D.K. Stewart, L.A. Stern, and J.C. Morgan SPIE Vol. 1089, 18 (1989).

12. T. Tao, W. Wilkinson, and J. Melngailis, J. Vac. Sci. Technol. B9, 162 (1991).

13. A. Wagner, J.P. Levin, J.L. Mauer, P.G. Blauner, S.J. Kirch, and P. Longo, J. Vac. Sci. Technol. B8, 1557 (1990).

14. D.K. Stewart, J. Morgan, B. Ward, J. Vac. Sci. Technol (to be published) Presented at 2nd Japan/US Seminar on Focused Ion Beam and Applications (Portland, Dec. 1990).

15. P.G. Blauner, J.S. Ro, Y. Butt, and J. Melngailis, J. Vac. Sci. Technol. B7, 609 (1989).

16. P.G. Blauner, Y. Butt, J.S. Ro, C.V. Thompson, and J. Melngailis, J. Vac. Sci. Technol. B7, 1816 (1989).

17. Z. Xu, T, Kosugi, K. Gamo, and S. Namba, J. Vac. Sci. Technol. B7, 1959 (1989).

18. J. Melngailis, P.G. Blauner, A.D. Dubner, J.S. Ro, T. Tao, and C.V. Thompson, Process Physics and Modeling in Semiconductor Technol. Ed. G.R. Srinivasan, J.D. Plummer and S.T. Pantelides, (ECS Proceeding Vol. 92-4) p. 653.

19. J. Melngailis, SPIE Vol. 1465 (1991) p. 36.

20. A.D. Dubner, A. Wagner, J. Melngailis, and C.V. Thompson, J. Appl. Phys. 70, 665 (1991).

21. A.D. Dubner, "Mechanism of Ion Induced Deposition", Ph.D. Thesis MIT (Sept. 1990).

22. J.S. Ro, "Microstructure and Mechanism of Gold Films Grown by Ion Induced Deposition", Ph.D. Thesis MIT (June, 1991).

23. J.P. Biersack and W. Eckstein, Appl. Phys. 34, 73 (1984).

24. J.S. Ro, A.D. Dubner, C.V. Thompson, J. Melngailis, Mat. Research Soc. Symp. Proc. 101, 255 (1988).

25. P.G. Blauner, J.S. Ro, Y. Butt, C.V. Thompson, and J. Melngailis, "Mat. Research Soc. Symp. Proc. 129, 483 (1989).

26. J.S. Ro, C.V. Thompson and J. Melngailis (to be published).

27. A.D. Dubner, and A. Wagner, J. Appl. Phys. 66, 870 (1989).

28. K. Halloway and S. Zuhoski, J. Electro. Chem. Soc. (to be published).

29. J.P. Biersack, Nucl. Instr. and Methods B27, 21 (1987).

30. Xin Xu, A.D. Della Ratta, J. Sosonkina, and J. Melngailis, J. Vac. Sci. Technol. B10, 2675 (Nov/Dec 1992).

Figure 1: Schematic of experimental setup for ion beam induced deposition using a pressure cell.

Figure 2: Decomposition yield as a function of average nuclear stopping power for different ion species and energies. Decomposition yield is the sum of the measured net deposition yield and the measured sputtering yield. Films were deposited at room temperature and 1.0 mTorr of DMG(hfac). For each ion species, two different energies, 50 and 100 keV, were used for deposition.

Figure 3: Decomposition yield as a function of average electronic stopping power. Decomposition yield is the sum of a measured net deposition yield and a measured sputtering yield. Each data point for stopping power represents a combination of each ion species and energy (see Table 5.3). Films were deposited using Ne^+, Ar^+, Kr^+, and Xe^+ at 50 and 100 keV each, and at room temperature and 1.0 mTorr of DMG(hfac).

Figure 4: Schematic of the collision cascade process of surface adsorbate decomposition.

Figure 5: Measured decomposition yield vs. calculated decomposition yield for the higher energies (50 & 100 keV), square symbols, and the lower energies (2-10 keV), triangular symbols, measurements of ref. 20. The calculated values were all obtained as described in the text. Both sets of data are seen to lie on straight lines (slopes 0.47 & 0.62). The difference in slope is likely due to the differences in measurement techniques. At low energies the mass of the film was measured on a quartz crystal microbalance (ref. 20) and it was assumed to be pure gold. At the high energy (this work) thickness was measured with a profilometer, and the yield was corrected for carbon content.

Figure 6: Relative yield as function of angle of incidence.

Focused ion beam induced deposition and ion milling as a function of angle of ion incidence

Xin Xu, Anthony D. Della Ratta, Jane Sosonkina, and John Melngailis
Research Laboratory of Electronics, Massachusetts Institute of Technology, Massachusetts 02139

(Received 28 May 1992; accepted 12 August 1992)

In the repair of integrated circuits, and x-ray masks focused ion beam induced deposition, and ion milling often have to be performed over quite nonplanar topography. Thus, the milling and the deposition as a function of the angle of ion incidence are important. The milling yield of Si, SiO_2, Au, and W versus angle of incidence using 25 keV Ga^+ ions has been measured. In qualitative agreement with simulations, the yield rises with angle and then falls as grazing incidence is approached. Deposition yield versus angle was measured using dimethylgold hexafluoro-acetylacetonate and $W(CO)_6$ as the precursor gases. The measurements were carried out using cylindrical quartz fibers 30–50 μm in diameter which automatically provide angles of incidence from 0° to 90° or on planar surfaces at various angles. Rippling of the deposited material is observed at angles of incidence greater than 50°.

I. INTRODUCTION

Focused ion beams (FIBs) are now widely used for the modification of integrated circuits (ICs) and for the repair of masks. Unwanted conductors or unwanted mask features are sputtered off by the scanning ion beam. FIB induced deposition is the process for material addition which can be used to reconstruct a missing feature.[1] In this process a local gas ambient of an appropriate compound, such as a metalorganic, is formed above the surface surrounding the point of ion incidence. The gas ambient is usually created with a small diameter tube aimed at the surface. The local pressure on the surface is in the 10^{-2}–10^{-3} Torr range, while in the rest of the chamber it is at a pressure 3–4 orders of magnitude lower, as needed for ion source operation and beam propagation. The precursor gas molecules adsorb on the surface where they are dissociated by the incident FIB. Since the ion beam can be focused down to diameters of 0.05 μm and below, submicrometer features can be deposited. In fact, 0.1 μm wide gold lines have been reported[2] as well as high aspect ratio features:[3] pillars 0.15 μm in diameter and 10 μm high or walls 0.15 μm thick and 5 μm high.[3]

One of the more demanding applications of FIB induced deposition is in the repair of x-ray lithography masks. Minimum features are 0.25 μm or less and the height of the features is in the 0.3–0.6 μm range. Thus, repairs may need to be carried out over severe surface topography. Similarly as the dimensions of conductors in ICs shrink, the topographic requirements for circuit repair become ever more challenging. Some relevant experimental observations made so far are that deposition on a "vertical" sidewall at near glancing incidence produces globular deposition of Pt with high yield,[4] that deposition in cavities has much higher yield than on a flat surface for Pt (Ref. 4) and W (Ref. 5), and that deposition yield increases in the case of Pt as the angle of incidence goes from normal toward grazing.[4] These point to the need to understand the deposition characteristics in the cases where the ion beam is not normally incident on the surface. In fact, even on an initially planar surface the deposition of a high aspect ratio feature will in itself induce non-normal ion incidence.

In this article, we will report on measurements of deposition and milling rates as a function of angle of incidence of the ion beam, as well as scanning electron microscope (SEM) observations of the features produced.

II. EXPERIMENTAL

The FIB system used for the gold depositions operates at 35–40 keV with $^{69}Ga^+$ ions. It is mounted on an ultrahigh vacuum (UHV) chamber that can be pumped well into the 10^{-9} Torr range. This system has been used in previous experiments.[2] The precursor gas is dimethylgold hexafluoroacetylacetonate and is aimed at the surface at about 45° from a stainless tube of 0.8 mm inner diameter as schematically shown in Fig. 1. The deposition was carried out with the ion beam focused on top of fused quartz fibers

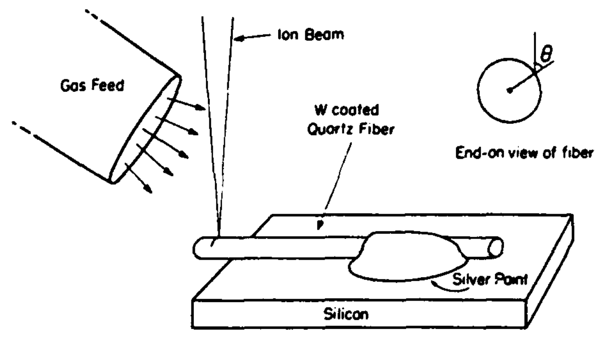

FIG. 1. Schematic of the FIB induced deposition process.

 ©1992 American Vacuum Society

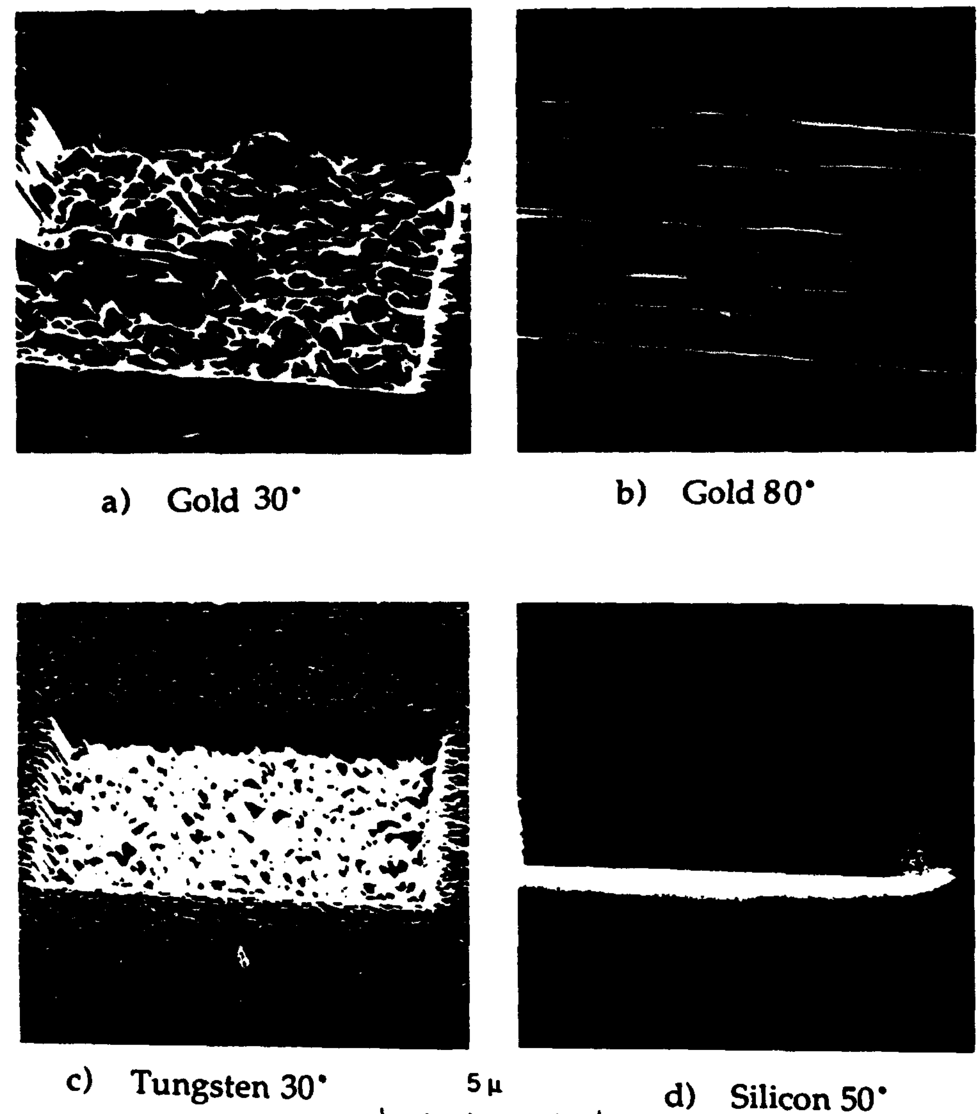

FIG. 2. FIB milling of three materials at various angles of incidence with a beam current of 283 pA and a dwell time per pixel of 0.3 μs. For (a) and (b) the average current $J_{av}=2.9$ PA/μm^2 and the time to mill the box is 2 min for (c) $J_{av}=7$ pA/cm^2 mill time 8 min and for (d) $J_{av}=7.1$ pA/μm^2 mill time 3 min.

30–50 μm in diameter and coated with tungsten to avoid charging. The thickness $d(\theta)$ of the deposits along the normal of the surface as a function of angle of beam incidence θ was measured with a SEM. Relative yield $Y(\theta)/Y(0)$ was obtained from $d(\theta)/d(0)\cos\theta$. Milling of trenches on the fiber was also carried out to measure the yield as a function of angle.

The tungsten deposition experiments and some of the milling versus angle experiments were carried out in an FEI model 500D FIB system which features a SEM type stage able to tilt up to 70° and has a base pressure in the 10^{-7} Torr range. The precursor gas, $W(CO)_6$, came from a heated reservoir and was directed to the area scanned by the FIB with a stainless capillary tube of 800 μm i.d. Milling and deposition were performed on quartz fibers as for gold, and also on planar samples. In the latter case stage-tilting capability was utilized, and two samples were mounted on the stage, one flat and one on a 45° wedge. Thus the entire 0°–90° range could be accessed by tilting only from 0°–45°. Besides the SEM, a surface profilometer and a WYCO interferometer were also used to measure the thickness of deposits or depth of grooves, and in each case, the microstructure was monitored using SEM. The diameter of the quartz fiber and the X,Y dimensions of milled boxes were used for interinstrumental calibration. The absolute value of yield $Y(0)$ can be calculated from the milling depth or deposition thickness, if the atomic number density is known (in milling) or can be reasonably assumed (e.g., for W deposits, see Sec. III). θ is usually referred to as the macroscopic average value of the angle of beam incidence for each section of surface, in spite of the fact that microscopic grains or an irregular structure may exist. In on-fiber experiments, the change of this θ during milling or deposition is small because the depth or thickness has been controlled to less than a tenth of the fiber radius.

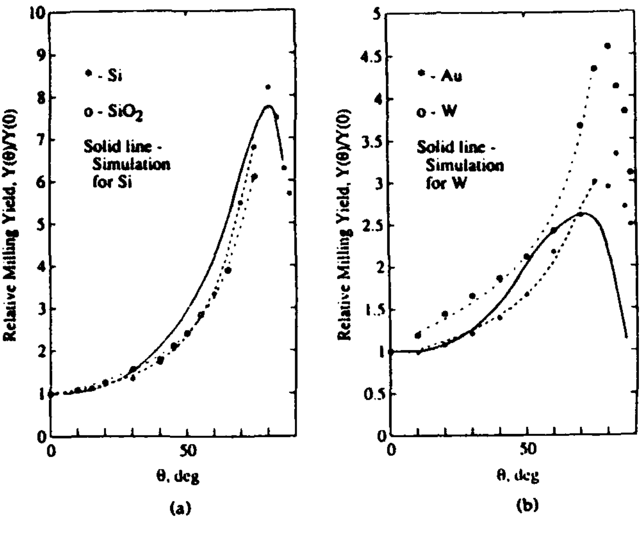

FIG. 3. Relative milling yield vs angle of incidence. The solid lines represent the results from a Monte Carlo simulation (TRIM). The dotted lines serve only to guide the eye. Results for SiO_2 were obtained by milling a quartz fiber with 35 keV $^{69}Ga^+$ at a beam current of 110 pA and an average current density of 2.9 pA/μm^2. Milling conditions for the rest: beam 25 keV $^{69}Ga^+$, beam current 283 pA, dwell time 0.3 μs/pixel, average current density 7 pA/μm^2 for W and Si, 2.9 pA/μm^2 for Au.

III. RESULTS AND DISCUSSION

A. Milling

The relative milling yield as a function of angle of incidence was measured for electroplated gold, radio-frequency (rf) sputtered tungsten (materials used as absorbers in x-ray masks), as well as SiO_2 and single crystal silicon. As has been observed by numerous workers (see for example Ref. 3), the individual crystallites in polycrystalline films mill at different rates leading to a rough surface, as shown in Fig. 2. Note that single crystal Si mills smoothly (Fig. 2), and noncrystalline SiO_2 also mills smoothly at low θ, and forms ripples perpendicular to the beam at $\theta > 45°$. Milling yields at normal incidence obtained in these experiments were 3.9 ± 0.4 (atom/Ga^+ of 25 keV, unless otherwise specified) for Si, 18 ± 3 for plated Au, 23 ± 5 for evaporated Au, 5 ± 0.7 for W, and 0.84 (molecule/Ga^+ of 35 keV) for SiO_2. This is in reasonable agreement with other workers' findings in Si (Refs. 6–8), Au (Refs. 2, 8, 9), W (Ref. 8), and SiO_2 (Ref. 10). All milling experiments were done in the rapid scanning regime where each pass of the beam removes only a fraction of a monolayer, thus avoiding significant effects of redepo-

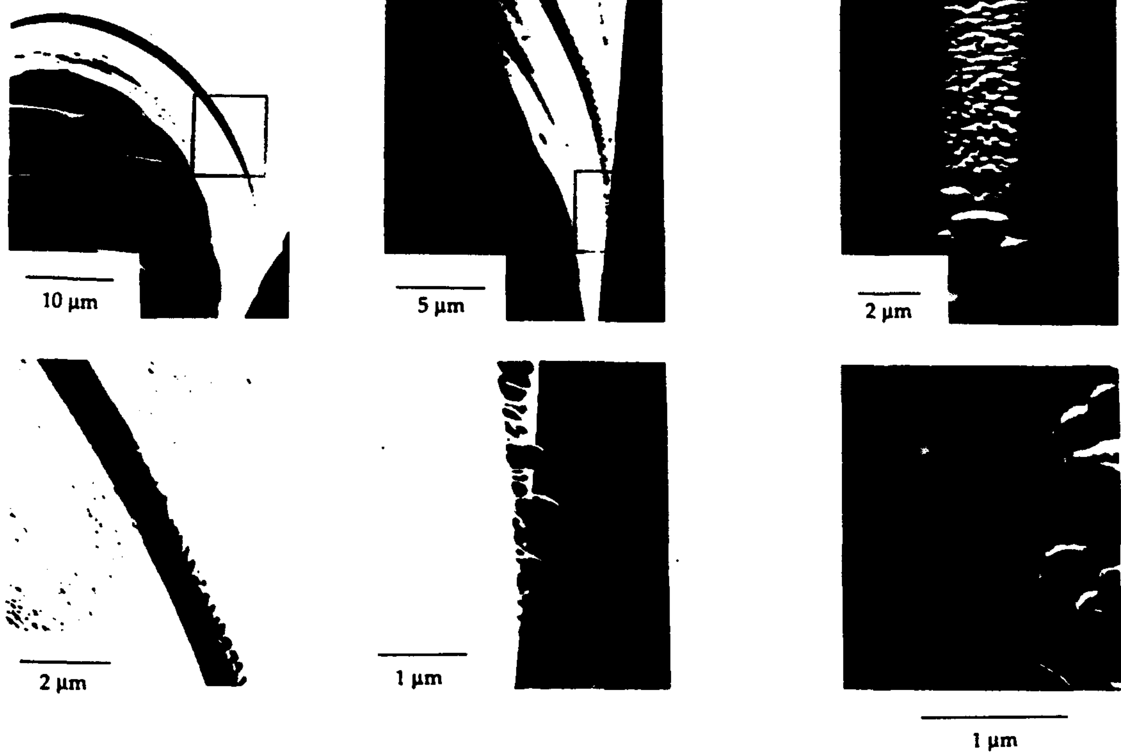

FIG. 4. SEM micrographs of gold deposition on a quartz fiber (with the gas feed 20° off-axis). The four photos on the left-hand side show the end-on view of the fiber while the two on the right-hand side show the region of grazing incidence deposition (lower middle end view photo) viewed at normal incidence. A peculiar growth consisting of an array of protrusions is seen. The lower left-hand side photo shows the transition from smooth to ripply deposition at 50°. The deposition was carried out by scanning a 35 keV, 118 pA, Ga^+ ion beam over a rectangle of 82 $\mu m \times 1.8$ μm for 50 min.

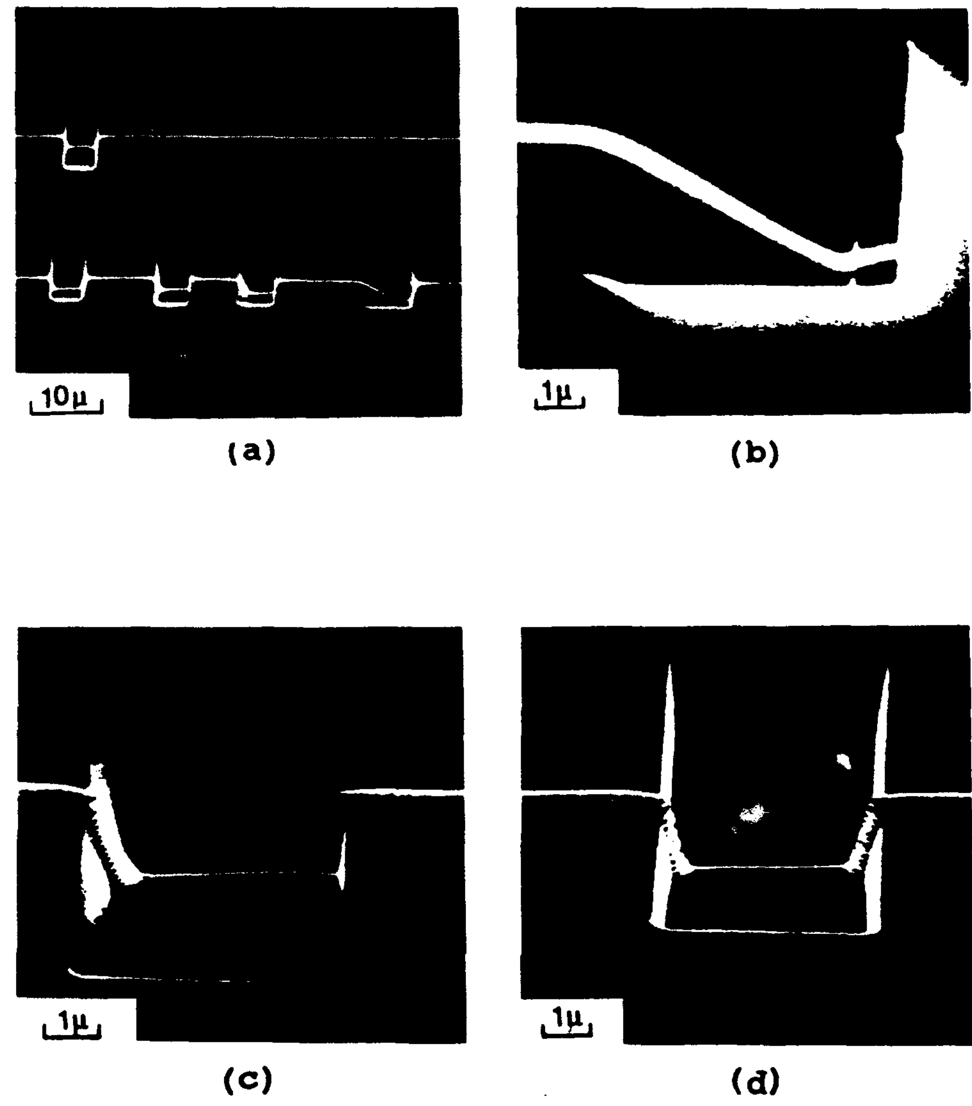

FIG. 5. Tungsten line deposited over grooves in Si with various sidewall angles. The sidewall deposits in (c) and (d) at steep angles of incidence show a comblike texture. The deposition conditions were 25 keV Ga^+ beam at 280 pA, $J_{av} = 9$ pA/μm^2, dwell time 0.3 μs and total scan time 2 min. The angles of incidence for the four walls with W deposition contained in (b)–(d) are ~40°, 75°, 85°, and 80°, respectively.

sition or of local non-normal incidence which would occur if each beam pass removed a thickness of material comparable to the beam diameter (see Ref. 11 for analysis of this point). For the polycrystalline Au and W samples, local non-normal incidence is obviously unavoidable and the overall milling rate is likely to depend on the average grain size and distribution of orientations. The relative milling yields as a function of angle of incidence for Si, SiO_2, tungsten, and gold are shown in Figs. 3(a) and 3(b). For comparison we have also included the relative sputter yields generated by a Monte Carlo simulation (the TRIM program).[12,13] Note that both the measurements and simulations show a drop off in the relative yield above 75°–80°. This is presumably due to the fact that near grazing incidence the incoming ion as well as the energetic secondary knock-on particles have a large probability of escaping from the surface. At intermediate angles, the yield increases with increasing angle of incidence, because the number of energetic particles in the collision cascade which reach the surface increases. At this point, the agreement is only in qualitative features, and, for example, for Si the simulated absolute yield at normal incidence $Y(0) = 1.67$ while the measured value is 3.9. For tungsten the simulated $Y(0) = 4.5$ and the measured value is 5.0, but the curve shape differs appreciably from that of experimental data. Since we have checked our experiment data with at least two different measurement methods, we suspect that some aspects of this version of TRIM need to be improved.

B. Ion induced deposition

We have measured the deposition yield as a function of the angle of incidence for gold and tungsten. These materials are of interest for circuit repair and, because of their high density, also for x-ray lithography mask repair. A deposit of gold on a quartz fiber is shown in Fig. 4. Tung-

sten deposited on milled groove walls of various angles is shown in Fig. 5.

A feature common to all of these results is the appearance of a ripply surface for angles of incidence greater than about 45°. At nearly glancing incidence separated islands of Au or comblike blades of W deposition were formed, as can be seen in Figs. 4 and 5. Once the ripples or blades are formed, one can qualitatively understand that they would propagate, because the underside of the feature has no ion flux incident and the leading edge grows fastest because the angle of incidence is optimal. The initiation of the periodic ripples after the original random nucleation may involve the growth of grains whose size is dictated by the extent of the collision cascade and which grow at the expense of those in their shadow. This will only happen at high angles of incidence because the milling and redeposition would tend to fill any local gaps when θ is small. The aboveargument is consistent with the observed fact that the period of the ripples increases with increasing angle of incidence, as indicated by Fig. 5. But at this time, we have not reached a firm understanding of this phenomenon.

Clearly the measurement of the deposition thickness is difficult above 45° due to the ripples, and the data taken there can only be regarded as a measure of the upper limit. In the case of gold deposition between 0° and 45°, where the data are most reliable, only a modest increase in relative yield was found, and a small effect of the gas arrival direction was also observed. In the case of tungsten deposition from $W(CO)_6$, the yield versus angle of incidence is shown in Fig. 6. Again, qualitatively the relative yield rises as the angle of incidence increases, but this increase in relative deposition yield is rather modest as compared to that for milling, especially for $0° < \theta < 45°$. In one case where the deposition was carried out with a higher average current density, the relative deposition yield drops in the 20°-50° range before beginning to rise. This effect, which can clearly be seen for both positive and negative angles on the film deposition over the fiber, is at this point not well understood. Also shown in Fig. 6 are the results of deposition on milled groove slopes as a function of angle of beam incidence. These results are in agreement with the results of deposition on a fiber. The deposited material was found to be mainly composed of 75% W and 25% C (atomic percent) and a small amount of Ga. Assuming the deposition has the same atomic number density as bulk W, a yield at normal incidence of $Y(0) = 2.2 \pm 0.4$ W/ion was obtained from on-fiber experiments.

The model of ion induced deposition which is based on the Monte Carlo calculations of the collision cascades[13-15] would qualitatively predict that the deposition should have similar angular dependence as the milling. It should be noticed, though, that the milling yield is much higher than the net deposition yield, especially for gold. We have not yet attempted to fit our deposition results to this model. To calculate the net deposition yield versus angle, we would need to calculate the dissociation yield Y_D and the sputter yield Y_s (or use the measured value of Y_s) and take the difference of two large numbers, i.e., $Y_N = Y_D - Y_s$. It appears suspect (e.g., from the deviation analysis point of view) that two large variables happened to give a rather small but more stable (with respect to angle of incidence) difference. This expression assumes that the sputter yield is unaffected by the presence of adsorbed gas molecules. An alternate point of view,[16] which assumes that sputteringcan take place only from sites not covered by the precursor, may need to be considered.

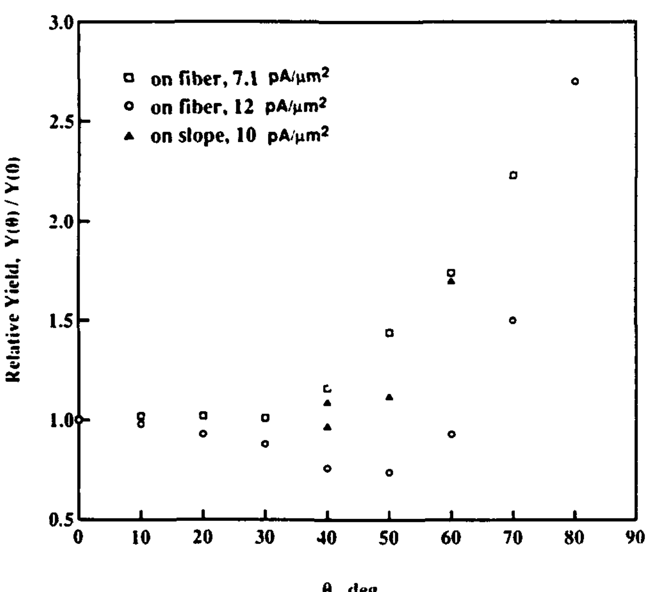

FIG. 6. The relative deposition yield vs angle of incidence for deposition from $W(CO)_6$. The current density values quoted are the average ion current density that would be incident on a sample normal to the ion beam. Total beam current was 280 pA. The data for $\theta > 45°$ can only be taken as the upper limit because of the rippling effect.

IV. CONCLUSIONS

For a rapidly scanned 25 keV Ga^+ ion beam of instantaneous current density ~ 1 A/cm^2, the milling yield versus angle of incidence for the four materials measured increases as the angle of incidence goes from normal (0°) toward grazing incidence (90°). For the three materials, Si, W, and Au for which our experimental data extend to near grazing, a sharp decrease in milling yields above about 80° was observed. The maximum value of the relative yield is 8 for Si, 4.5 for W, and 3 for Au, all attained at angles between 70° and 80°. Simulations for Si and W qualitatively agree with the measurements. In FIB induced deposition the yield also increases as the angle of incidence goes from normal to grazing. However, at 45° and above a rippling of the deposited material is observed for Au and W in the form of discrete periodic structures.

ACKNOWLEDGMENTS

This work was supported in part by the ARO Contract No. DAAL 93-90-G-0223 and in part by the NRL Contract No. N00014-89-2238 under subcontract from Micron Corp. The authors wish to thank the FEI Co. for the donation of a FIB system Model 500D to MIT. We are grate-

ful to James Carter and Jean Porter for help with the SEM and with thin film preparation issues.

[1]For a review of ion induced deposition and references to the literature see K. Gamo and S. Namba, Microelectron. Eng. 11, 403 (1990); or J. Melngailis, Proc. SPIE 1465, 36 (1991).

[2]P. G. Blauner, Y. Butt, J. S. Ro, and J. Melngailis, J. Vac. Sci. Technol. B 7, 609 (1989).

[3]A. Wagner, J. P. Levin, J. L. Mauer, P. G. Blauner, S. J. Kirch, and P. Longo, J. Vac. Sci. Technol. B 8, 1557 (1990).

[4]T. Tao, J. S. Ro, J. Melngailis, Z. Xue, and H. Kaesz, J. Vac. Sci. Technol. B 8, 1826 (1990); T. Tao, W. Wilkinson, and J. Melngailis, *ibid.* 9, 162 (1991).

[5]D. K. Stewart, J. A. Morgan, and B. Ward, J. Vac. Sci. Technol. B 9, 2670 (1991).

[6]H. Yamaguchi, J. Phys. C 6, C6 (1987).

[7]J. G. Pellerin, G. M. Shedd, D. P. Griffiths, and P. E. Russell, J. Vac. Sci. Technol. B 7, 1810 (1989).

[8]H. H. Anderson and H. L. Bay, in *Sputtering by Particle Bombardment I. Physical Sputtering of Single Element Solids*, edited by R. Behrisch (Springer, Berlin, 1981), p. 145.

[9]K. P. Muller and H. C. Petzold, Proc. SPIE 1263, 12 (1990).

[10]J. Melngailis, C. R. Musil, E. H. Stevens, M. Urlaut, E. M. Kellogg, R. J. Post, M. W. Geis, and R. W. Mountain, J. Vac. Sci. Technol. B 4, 176 (1986).

[11]T. Ishitani and T. Ohnishi, Jpn. J. Appl. Phys. 28, L320 (1989).

[12]J. P. Biersack and L. G. Haggmark, Nucl. Instrum. Methods 174, 257 (1980); J. P. Biersack and W. G. Eckstein, Appl. Phys. A 34, 73 (1984); J. P. Biersack, Fusion Technol. 6, 475 (1984).

[13]A. D. Dubner, A. Wagner, J. Melngailis, and C. V. Thompson, J. Appl. Phys. 70, 665 (1991).

[14]A. D. Dubner, Ph.D. thesis, MIT, September 1990.

[15]J. S. Ro, Ph.D. thesis, MIT, June 1991.

[16]Y. Takahashi, Y. Madokoro, and T. Ishitani, Jpn. J. Appl. Phys. 30, 3233 (1991).

Quasi-Periodic Nano-Structures in Focused Ion Beam Deposited Tungsten at High Angles of Incidence

Xin Xu and John Melngailis

Research Laboratory of Electronics, Massachusetts Institute of Technology, Cambridge, Massachusetts 02139

Abstract

As reported in our previous work, at high (near glancing) angles of incidence of ion beam, a quasi-periodic, comb-blade like metal structure can form in focused ion beam (FIB) induced deposition, most typically in tungsten but also in gold, platinum or copper depositions. This kind of discontinuity tends to increase the resistance if a metal link needs to be made across a rather deep and near-vertical wall. On the other hand, if controlled, it may find some useful applications in nano-fabrication. We investigated this phenomenon by using "milling-and-deposition" on single crystal silicon and examining the correlation between the "period" and various experimental parameters. We found that there is no correlation between the period and step size of beam scanning. The average period depends on the beam incidence angle, and especially on the ion beam energy. The average period is 55, 75 and 105 nm for the Ga^+ energy at 10, 20 and 25 keV respectively, when the beam incidence angle during deposition is around 75°. The range of the thickness of the "comb-blades" is about 75 ± 25 nm. The period becomes larger as the beam energy and beam incidence angle increases.

Introduction

The focused ion beam induced deposition process consists of a capillary gas feed which produces a local gas ambient on the sample surface usually of an organometallic or of metal carbonyls. The incident ions dissociate the gas molecules adsorbed on the surface leaving a deposit (Fig. 1). This process is now widely used in the repair and rewiring of prototype integrated circuits and in the repair of masks. In the repair of some circuits, and particularly in the repair of X-ray lithography masks, deposition will need to be carried out over quite non-planar topography. In the course of measuring the deposition yield as a function of the angle of incidence by depositing on a fiber we have observed that the deposited material has ripples on the surface or consists of deep blade-like structures near glancing incidence[1] (See Fig. 2). This was observed in gold and tungsten and has also been seen in platinum [2] and most recently copper [3] deposition.

The discontinuity in the deposition on near vertical surfaces may increase the resistance of a conductor that is deposited over a step and may change the X-ray attenuation of features added during repair that cross existing high-aspect-ratio structures. The phenomenon may also affect the fillings of deep vias [4] and the growth of very high aspect-ratio structures where the grown structure itself presents near vertical faces, and where small protrusions are seen on these faces. [5] [6].

This paper reports how the formation of the ripples depends on various deposition parameters.

Experimental

The apparatus was on FEI Model 500D system with a 25 kV ion column and a tiltable and rotatable sample stage. The gas used was $W(CO)_6$ piped in from a heated reservoir through a capillary tube as in Fig. 1. First rectangular pits (8 µm x 4 µm, 1.8 µm deep) were milled in single crystal Si(100) at various small tilt angles of the stage, usually

0—10°. The stage was returned to be perpendicular to the ion beam, and deposition of a tungsten line was then carried out across the edges of a series of pits, thus keeping all the deposition conditions the same except for the angles of beam incidence θ for these side-walls. In the experiments with different beam energies or with different step-sizes of beam scan, the other experimental parameters could also vary somewhat. The period of the ripples was measured by examining in an SEM.

Results and Discussion

In searching for the reasons for the formation of this kind of quasi-periodic structures in deposits, one would first think of the fact that the beam is scanned step by step during the deposition. Therefore we first investigated the correlation between the characteristics of the structures (using the average period as a measure) and the step-size of the beam scan. Our experimental results indicate no or little correlation between the average period and the beam scanning step-size, as can be seen in Fig. 3(a). The second factor need to be studied is naturally the angle of incidence of ion beam θ, because these structures only occur at high θ, and we already saw the sign of the angular dependence of the structure in Ref [1]. Results from more systematic experiments verified this, and are shown in Fig. 3(b). Note that, when the Si(100) surface is set perpendicular to the ion beam, i.e. the tilt angle of stage $\alpha = 0°$, the side-walls of a deep pit milled by the 280 pA and 25 keV Ga^+ beam from the FEI 500D system have an effective slope of ~7° from the ideal vertical direction. During the deposition, where the Si(100) surface was always set at 0° tilt, these walls will have a θ of 83°. If the Si(100) surface has a tilt angle α during the pit milling, this 7° "intrinsic" slope will add to the tilt angle. The effective slopes for the two walls along the tilting direction will be $(7 \pm \alpha)°$. A negative value represents a "concave" or hidden slope to the ion beam. We observed that such a wall will bear no deposition. There is also a small range of slope, from 0° to ~ 3°, where the structure

periodicity is not stable. Another noted experimental fact is that on the near vertical walls, the growth direction of the comb blades is around the middle in between the ion beam and the normal direction of the wall, i.e. upward at about a 45° angle.

We found from our experiments that the most critical factor is the beam energy. The measured period is plotted vs. energy in Fig. 3(c). It is seen to increase by about a factor of 2 in going from 10 keV to 25 keV. The SEM micrographs of tungsten deposited on near vertical walls by Ga^+ of different energies are shown in Fig. 4.

Shown in Fig. 5 are the front views of some of these quasi-periodic structures. In Fig. 5(a) and 5(b) we can see the effect of beam energy on the period and structure of the tungsten deposition at $\theta = 83°$. In Fig. 5(c) and 5(d), the deposits on fibers at near grazing incidence are shown for two different distances of the gas delivery tube from the sample. This, in effect, varies the pressure of the precursor gas. There is about a 20 percent decrease in period for the larger tube to sample distance.

These quasi-periodic deposit structures can be viewed as a mass oscillation of the deposited material with respect to the spatial dimension. One criterion for an oscillation to occur is that there is a positive feedback in the process. At high θ, a region shaded by a protrusion would have no ion flux while the leading edge has an optimal angle of incidence for growth. This is a positive feedback in nature, so there is no surprise to see the deposit mass oscillation at high θ. What we need to understand is why this oscillation can be periodic or quasi-periodic (again, with respect to spatial dimension), what are the physics and chemistry underneath this phenomenon. It is still not clearly understood at this moment. However, the strong beam-energy dependence could have pointed out to us the direction.

We assume, the average period mainly consists of two parts: the average thickness of the blades, which is basically determined by the "range of ion energy dissipation" (RIED) in the deposited material, and the shaded distance along the surface. Thus we can propose a first order approximation formula for the average period L measured along the substrate surface as follows:

$$L = A + B \cdot \tan \theta$$

where A is an ion-energy dependent constant, which can be taken as a measure of the RIED, B a coefficient, θ the angle of incidence of the ion beam for the surface. A fit of the data in Fig. 3(b) gives A = 82 nm, B = 5.0 nm for 25 keV Ga^+. The fit curve is also plotted there. It seems that, not only on the leading edge, but also on the back edge of a thin blade, if located within the RIED from the incidence point of an ion, the adsorbed precursor molecule can get the necessary energy to dissociate. Data and information from different types of experiments give us the hint that this RIED can be of the order of 75 ± 25 nm for 25 keV Ga^+. Obviously, the RIED decreases as ion energy decreases, and hence the period of the comb-blade structure, as already seen in Fig. 3(c). Applying the RRKM theory[7] to the beam induced surface reactions[8], we can imagine that, no matter what the details are, the energy transfer from ion to the adsorbed precursor molecule has to include the statistical distribution of available excitation energy into all possible degrees of freedom before the molecule can be fully dissociated. Therefore, RIED can be expected to vary with other parameters, e.g. substrate temperature, as well as ion energy E_i.

The range of 25 keV Ga^+ ion in our deposited material (a mixture of W and C) is estimated to be between 5 to 10 nm, much smaller than the RIED. At this point more experiments need to be done to determine if this RIED concept has any physical meaning. We can speculate that just as in the case of III-V compounds the depth of damage due to ion bombardment by low energy ion s has been found to be much higher than the penetration depth[9,10], so in this case also the energy needed to dissociate the adsorbate

can penetrate deeper than the range. Near glancing incidence each ion would cause deposition to occur along a 75 nm stripe rather than a stripe defined by the 5—10 nm range.

Summary

Quasi periodic ripples and comblike blades form in material grown by focused ion beam induced deposition near glancing incidence. In the case of deposition from $W(CO)_6$ this period increases with increasing energy (10—25 keV) and increases as grazing incidence is approached. If these ripples pose a problem, for example, in deposition of conductors over near vertical surfaces in integrated circuit repair, then the results suggest that lowering the ion energy will decrease the depth of the ripples. An assumption of the "range of ion energy dissipation" , which could be of the order of 75 ± 25 nm for 25 keV Ga^+, was proposed.

Acknowledgments

This work was supported in part by ARO contract No. DAAL 90-6-0223 and in part by the NSF.

References

1. X. Xu, A. D. Della Ratta, J. Sosonkina, and J. Melngailis, J. Vac. Sci. Technol. **B 10,** 2675 (1992).

2. T. Tao, J. S. Ro, J. Melngailis, Z. Xue and H. Kaesz, J. Vac. Sci. Technol. **B 8,** 1826 (1990).

3. A. D. Della Ratta, C. V. Thompson and J. Melngailis, This Conference, Submitted to J. Vac. Sci. Technol. **B**.

4. D. K. Stewart, J. A. Morgan, and B. Ward, J. Vac. Sci. Technol. **B 9,** 2670 (1991).

5. A. Wagner, J. P. Levin, J. L. Mauer, P. G. Blauner, S. J. Kirch, and P. Longo, J. Vac. Sci. Technol. **B 8,** 1557 (1990).

6. D. K. Stewart, L. H. Spern, G. Foss, G. Hughes and P. Govil, SPIE, Vol. **1263**, 21 (1990).

7. See, e.g. (a) J. Steinfeld, J. Francisco and W. Hase, Chemical Kinetics and Dynamics (Prentice-Hall, Englewood Cliffs, NJ, 1989) Ch.11. (b) R. G. Gilbert and S. C. Smith, Theory of Unimolecular and Recombination Reactions (Blackwell, Oxford, 1990).

8. X. Xu and J. I. Steinfeld, Appl. Surface Sci. **45**, 281 (1990).

9. S. W. Pang, J. Electrochem. Soc. **133**, 784 (1986).

10. D. Kirillov, C. B. Cooper, and R. A. Powell, J. Vac. Sci. Technol. **B 4**, 1316 (1986).

11. S. W. Pang, W. D. Goodhue, T. M. Lyszczarz, D. J. Ehrlich, R. B. Goodman, and G. D. Jonson, J. Vac. Sci. Technol. **B 6,** 1916 (1988).

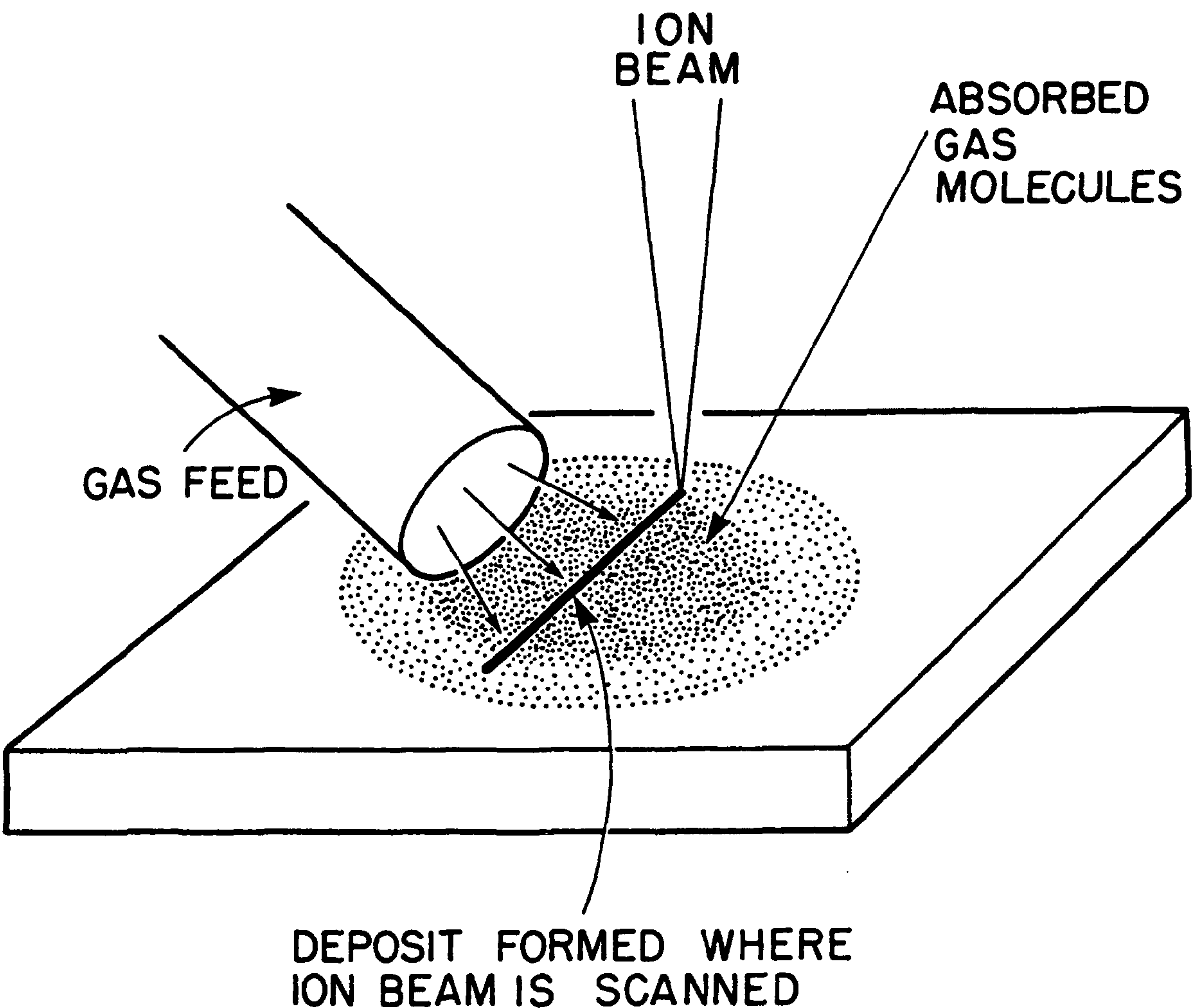

Fig. 1. Schematic of focused ion beam induced deposition.

Fig. 2. High aspect ratio tungsten deposited on a fiber using $W(CO)_6$ gas. Deposition conditions: 280 pA x 10 min over 45 μ long line, quartz fiber coated with ~40 nm W. (a) and (b) view of deposition at 0° angle of incidence, and (d) near 90°.

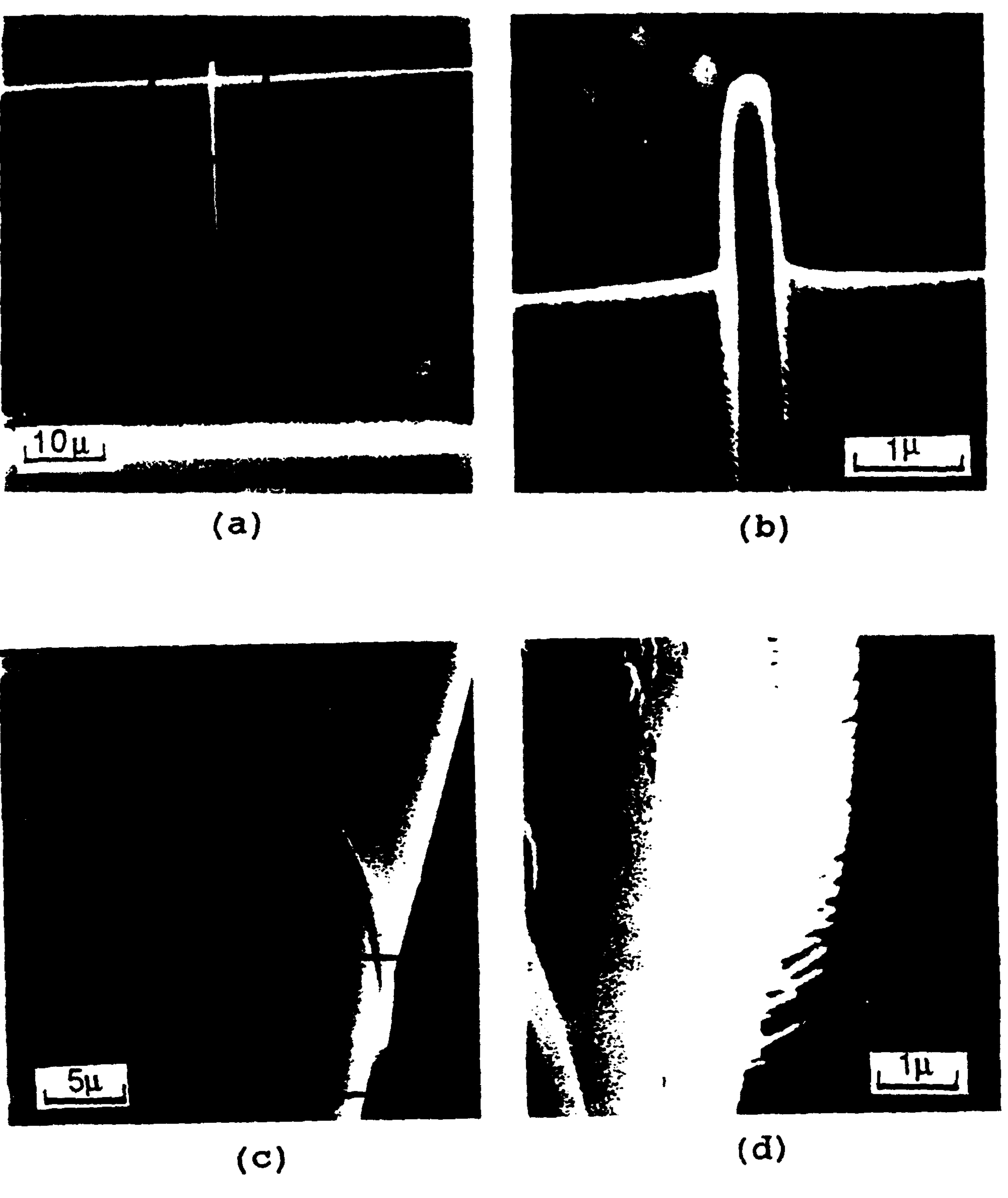

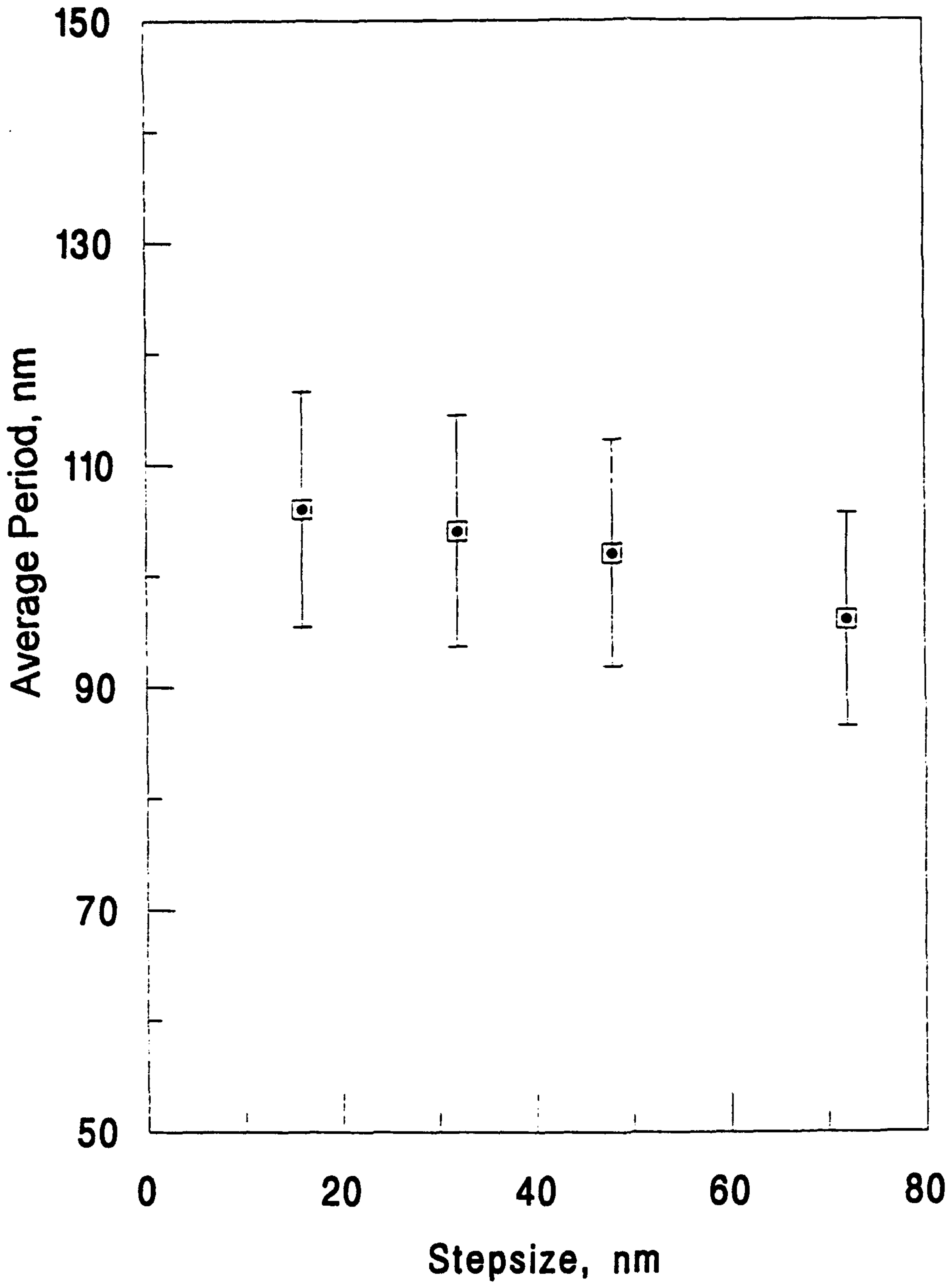

Fig. 3(a). Average period of tungsten nano-structure vs. ion beam scanning step size. Tungsten deposited with 25 keV Ga^+, I_b = 280 pA, beam size 80 nm. Corrected angle of incidence of ion beam is 73°, length of slope 1.8 μ.

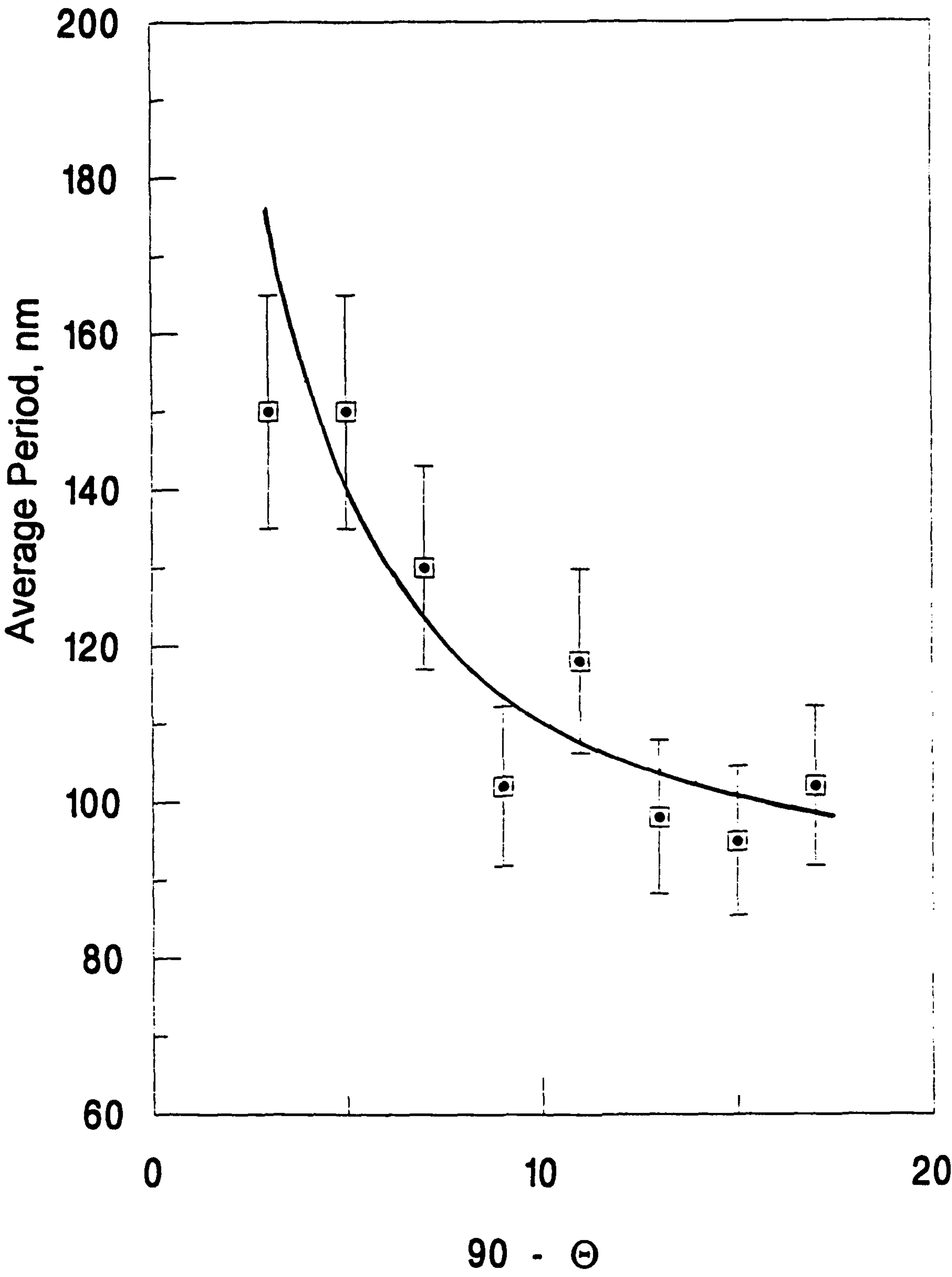

Fig. 3(b). Average period of tungsten nano-structure vs. corrected angle of incidence of ion beam. Tungsten deposited with 25 keV Ga^+, I_b = 280 pA, beam size 80 nm. When Si(100) is set perpendicular to the ion beam, the deep vertical walls of the pit resulted by milling have an effective slope of 7° from the ideal vertical wall.

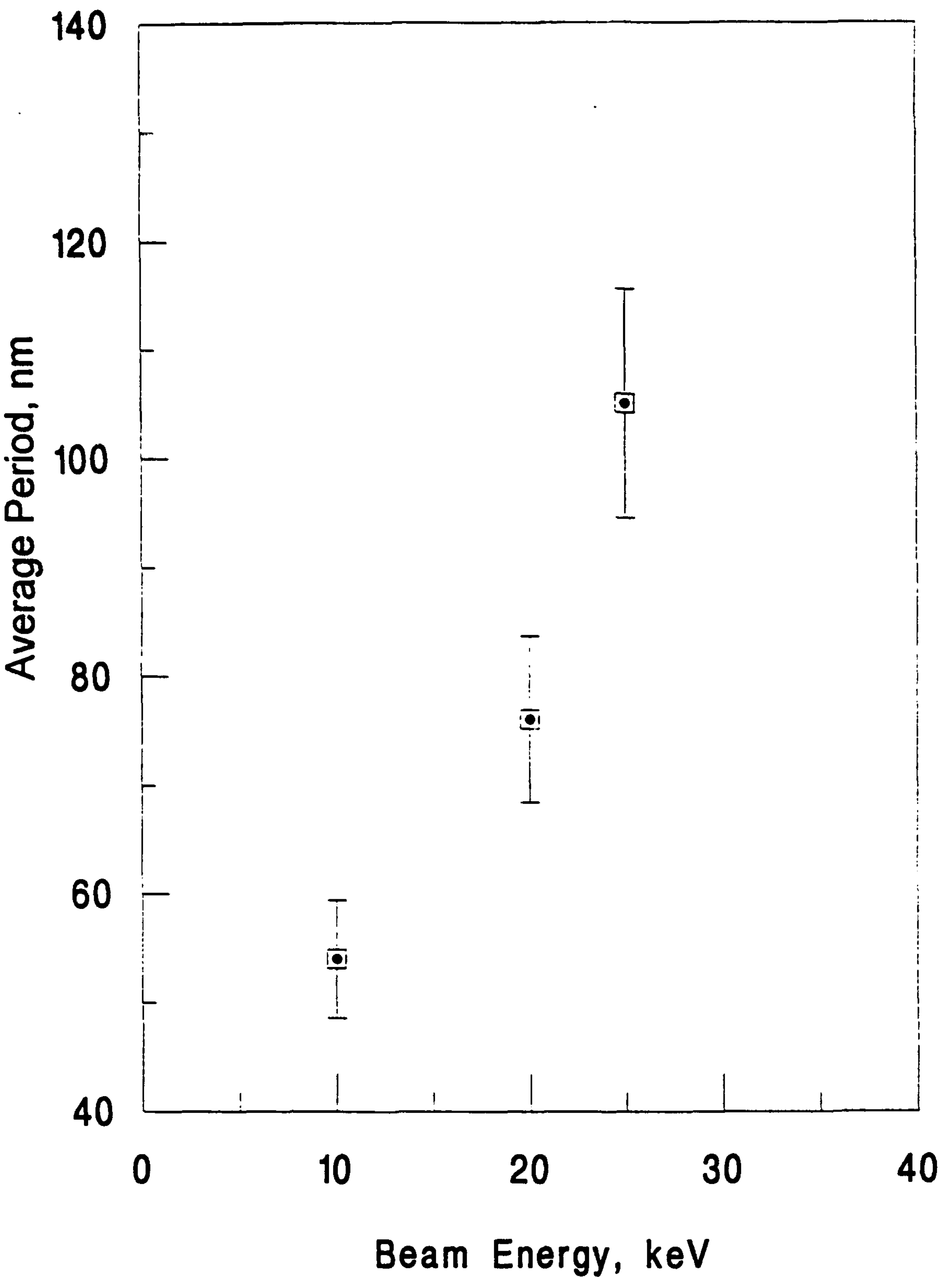

Fig. 3(c). Average period of tungsten nano-structure vs. Ga^+ ion energy. Angle of incidence of ion beam is 75°, depth of pit 1.8 μ.

Tungsten deposited with Ga^+ beam of different energy

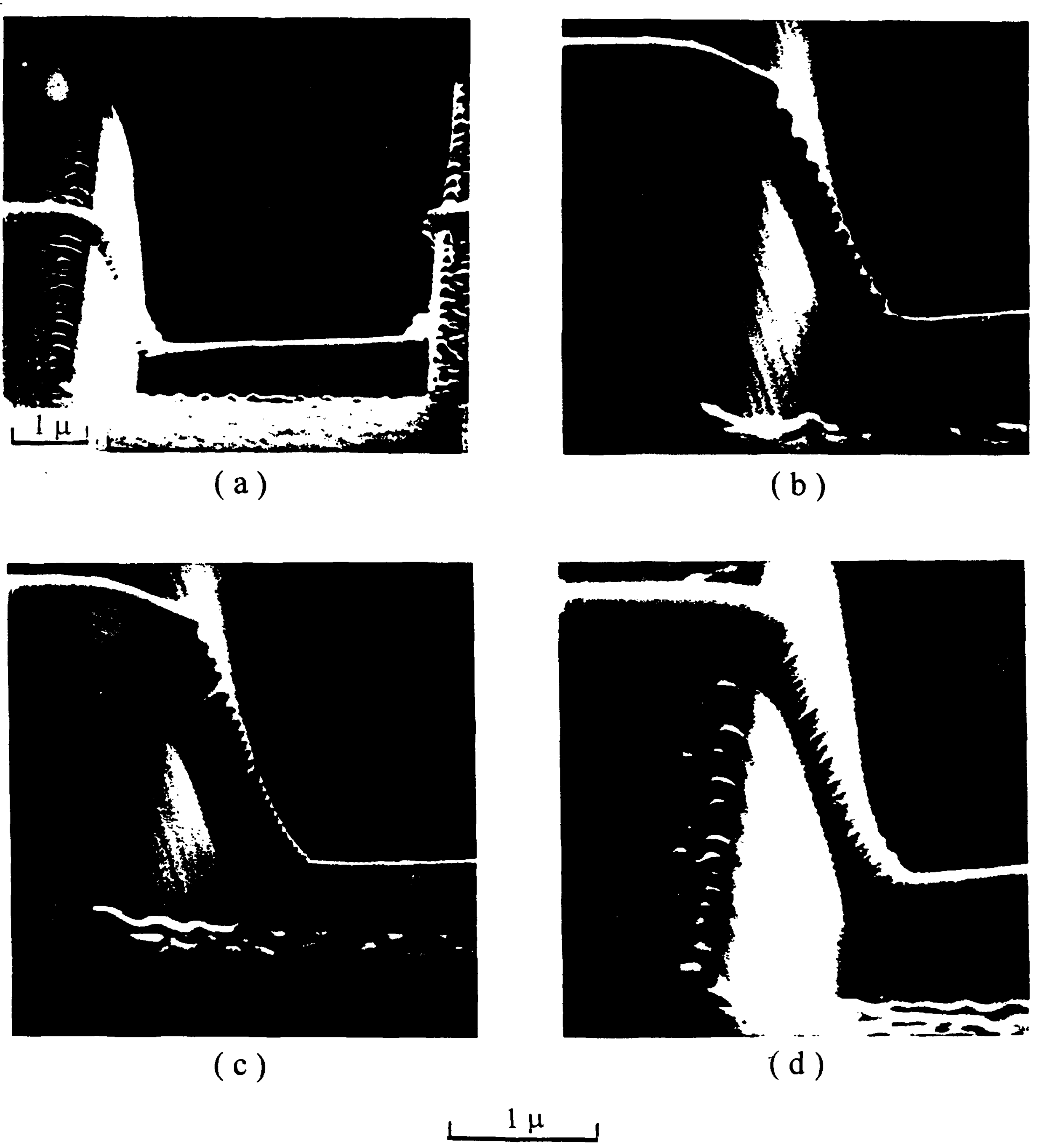

Fig. 4. Tungsten deposited with Ga^+ beam of different energy. Corrected angle of beam incidence on the left walls is 75°. Ga^+ beam energy: (a) and (b) 25 keV, (c) 20 keV, (d) 10 keV.

W deposited at near vertical surfaces, front views

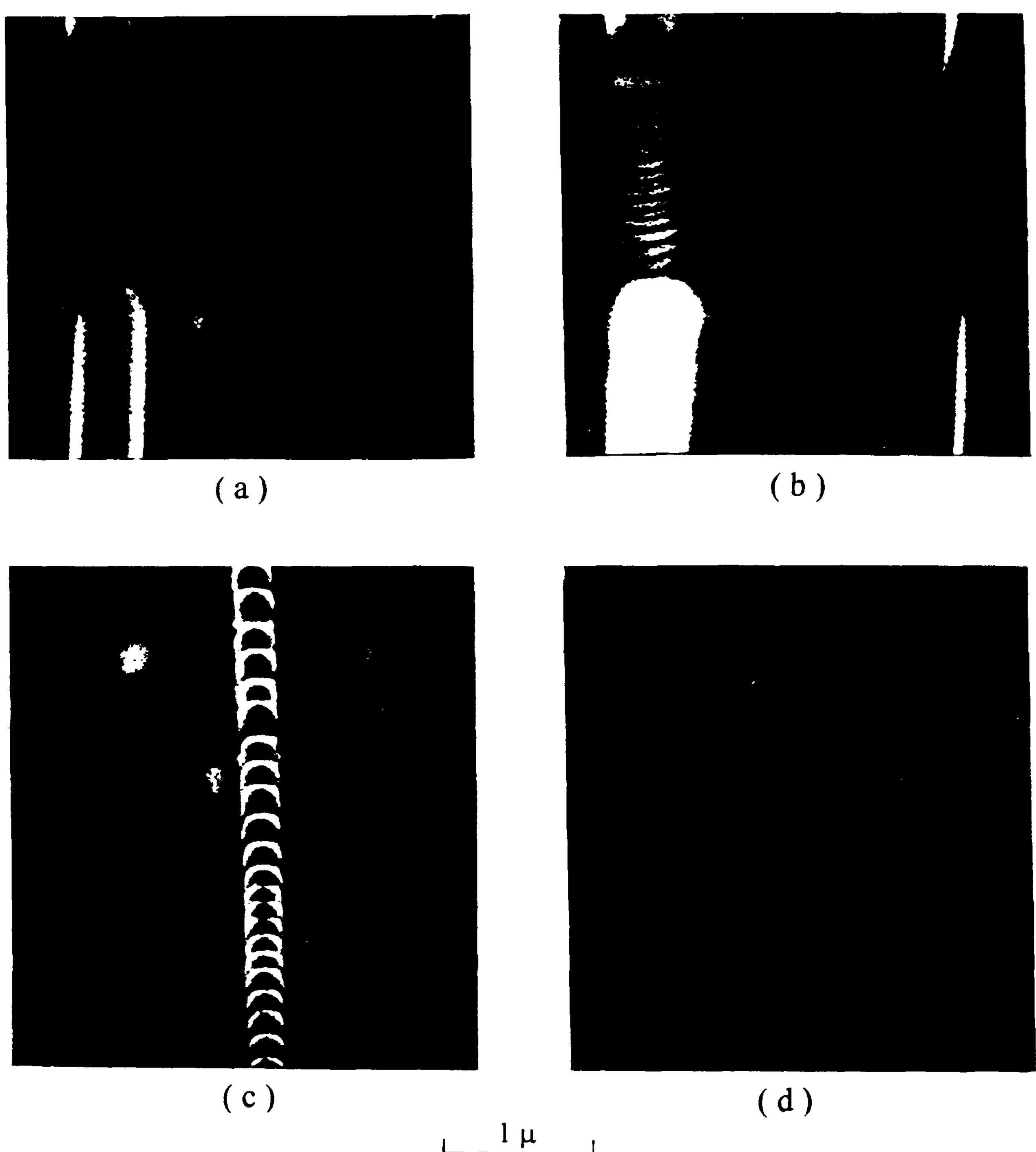

Fig. 5. Tungsten deposited at near vertical surfaces, front views. Deposition conditions: (a) 25 keV Ga^+, 280 pA, beam size 80 nm, 50 μm long line deposited for 2 min. across -7° wall; (b) 10 keV Ga^+, 260 pA, beam size 180 nm, the rest are the same as in (a); (c) W blade structure deposited with 25 keV Ga^+, 72 pA x 8 min, beam size 60 nm, 80 μ long line on fiber, gas jet height ~200 μ; (d) same as in (c), except gas jet height ~800 μ.

Microstructure of Gold Grown by Ion Induced Deposition

by

Jae Sang Ro, Carl V. Thompson and J. Melngailis

Research Laboratory of Electronics
Massachusetts Institute of Technology
Cambridge, MA 02139

Abstract:

Ion induced deposition is a process of film growth where adsorbed gas (usually organometallic) molecules are decomposed on the surface by ion impact leaving a deposit behind. This process is used in focused ion beam repair of microelectronic devics and masks. The deposited films are usually mixtures of metal and carbon. We have studied the microstructure of ion deposited gold by transmission electron microscopy. The gas used was dimethylgold hexafluoro acetylacetonate. The film is found to be made up of segregated gold and carbon. The gold can either be in the form of grains (isolated, approximately spherical island 20-50 nm in diameter, in the form of columns perpendicular to the surface of comparable diameter, or in the form of a normal polycrystalline structure. Higher temperature growth (80-100°C) or slower growth rate favors the polycrystalline films while faster growth or growth at room temperature tends to produce granular films with high carbon content. The incorporation of carbon may be related to the inability of the reaction products to escape from the surface.

Introduction:

Ion induced deposition is a new method of thin film growth which is used together with a finely focused ion beam for integrated circuit repair or restructuring and for mask repair. The focused ion beam (usually Ga^+ at 10-40 keV) by itself can be used to remove material with 0.1 μm resolution for example to cut conductors in an integrated circuit or to remove unwanted mask material. Ion induced deposition provides the inverse process.[1,2] A local gas ambient is created on the surface in the area where the ion beam is incident. If the gas is an organometallic, for example, then the ions cause molecules that are adsorbed on the surface to break up leaving the metallic component as a deposit on the surface. Numerous gases have been used to deposit W, Al, Au or Pt with minimum linewidths down to 0.1 μm.[3] [3a] In all cases the "metal" films are impure and contain, most often, 10 to 50 at % of carbon, and the resistivity of the films is 20 to 200 times higher than that of the pure metal.[2] In applications to circuit repair the films are still usable as conductors since they can be made thick to compensate for the poor conductivity.

We have studied the microstructure of gold films deposited from dimethylgold hexafluoacetylacetonate. In the repair applications focused beams of Ga ions are used in the energy range of 10-100 keV. We have used noble gas ions from an implanter in the energy range of 50 to 100 keV. Our previous results [2] indicate that the properties of the films such as microstructure, deposited using finely foucsed beams of Ga ions are similar to those obtained using noble gas ions.

Experimental:

The apparatus used to deposit the films is shown in Fig. 1. It consisted of a separately pumped chamber which was inserted into the end-station of a

standard research ion implanter. The gas was fed to the surface with a small capillary tube which provided a local pressure on the surface in the 1-10 mTorr range. In some experiments where we wished to know the local pressure accurately, a small enclosure surrounded the sample with an opening for the ion beam, an opening for the gas, and an opening for pressure measurement. Noble gas ions in energies of 50-100 keV were used, but most of the microstructure studies were carried out with Ar at 70 keV. The samples were attached to a platform which could be resistively heated.

After growth the samples were examined in transmission electron microscopy (TEM) in both plan view and cross section. For the plan view the films were deposited to a thickness of < 100 nm over SiN windows (100 nm thick). These windows were held in a silicon wafer "frame" and were made by etching a hole from the back in a small part of a SiN coated silicon wafer. The samples for cross section TEM were prepared by standard techniques. Two small samples were glued face to face, potted in a molybdenum tube and cut into disks and thinned to 100 μm and then dimple ground to about 30 μm with diamond paste. The samples were then ion milled at 15° until they were optically transparent and a small hole was beginning to form near the region of interest.

The composition of the films was determined by Auger Analysis.

<u>Results:</u>

Three types of micro structure of the gold/carbon films were observed: granular, that is grains of gold in a carbon matrix; columnar, that is columns of gold surrounded by carbon, or polycrystalline. In all cases the electron diffraction rings were characteristic of pure gold, i.e. with the normal lattice constant and crystal structure. This observation together with the Auger

analysis results supports the claim that the film in the first two cases consists of gold grains or gold columns surrounded by carbon.

The properties and growth conditions for the three types of "gold" films grown by ion induced deposition are shown in Fig. 2. The TEM micrographs of the granular structures in cross section are shown in Fig. 3, the columnar structures in Fig. 4 (a) & (b) plan view and in Fig. 5 cross section, and the polycrystalline structure is shown in Fig. 4 (c) & (d). Our observation that complements these results is that the resistivity of the film drops sharply as the substrate temperature during deposition is raised from room temperature to 120°C. This has been observed for deposition with both Ar ions[4] and Ga ions.[5] In fact the resistivity drop by about 2 orders of magnitude between 40 and 90°C, (i.e. from 500-1000 μΩcm to 3 to 10 μΩcm).

The picture that emerges from these observations is that the carbon is incorporated in the film due to the fact that the reaction products of the initial breakup of the $C_7H_7O_2F_6$ Au molecule do not readily desorb from the surface so that subsequent ion impacts will further break up these molecules leaving carbon behind. Heating the substrate increases the desorption rate of the reaction products and leads to purer films. Similarly growing at a slower rate, i.e. lower average current density, leaves more time for the reaction products to escape.

References:

1. For a recent review see J. Melngailis, "Materials Issues in X-ray Mask Repair by Focused Ion Beams," to be published in MRS Proceedings (Spring Mtg. 1993) *Materials Aspects of X-ray Lithography*.
2. P.G. Blanner, J.S. Ro, Y. Butt and J. Melngailis, J. Vac. Sci. Technol. **B7** 609, (1989).
3. D.K. Stewart, J.A. Morgan, and B. Ward, J. Vac. Sci. Technol. **B9**, 2670 (1991), T. Tao, J.S. Ro, J. Melngailis, Z. Xue, and H. Kaesz, J. Vac. Sci. Technol. **B8**, 1826 (1990).
4. J.S. Ro, A.D. Dubner, C.V. Thompson and J. Melngailis, MRS Symp. Proceedings, Vol. 101, p. 255 (MRS 1988).
5. P.G. Blanner, Y. Butt, J.S. Ro, C.V. Thompson, and J. Melngailis, J. Vac. Sci. Technol. **B7**, 1816 (1989).

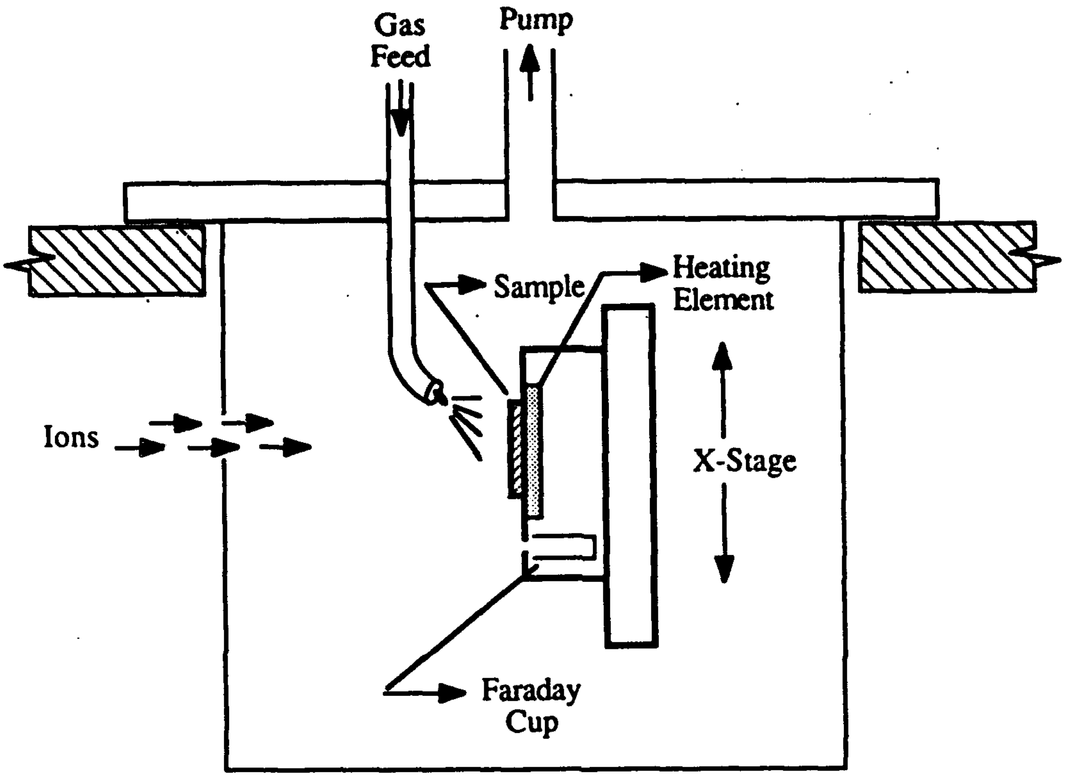

Fig. 1 Schematic of the apparatus used for ion beam induced deposition. The chamber is about 15 cm in diameter and fits into the end station of an ion implanter. The noble gas ions are incident on the sample through a 3 mm hole in the side. The inset at the bottom shows an enlarged view of the deposit in cross section and top view.

Microstructure of Films

Type		Composition	Conditions	
Substrate	granular	more than 50% C	Ar^+ 70 kV 7 μA/cm^2 room T	
	columnar	30-50% C	Ar^+ 70 kV 0.7 μA/cm^2 room T	Ar 70 kV 7μA/cm^2 T ~ 100°C
	polycryalline	less than 30% C	Ar^+ 70 kV T > 100°C 0.7 μA/cm^2	

Fig. 2. Tabulation of the three types of microstructure observed in the films deposited from dimethylgold hexafluoroacetylacetonate.

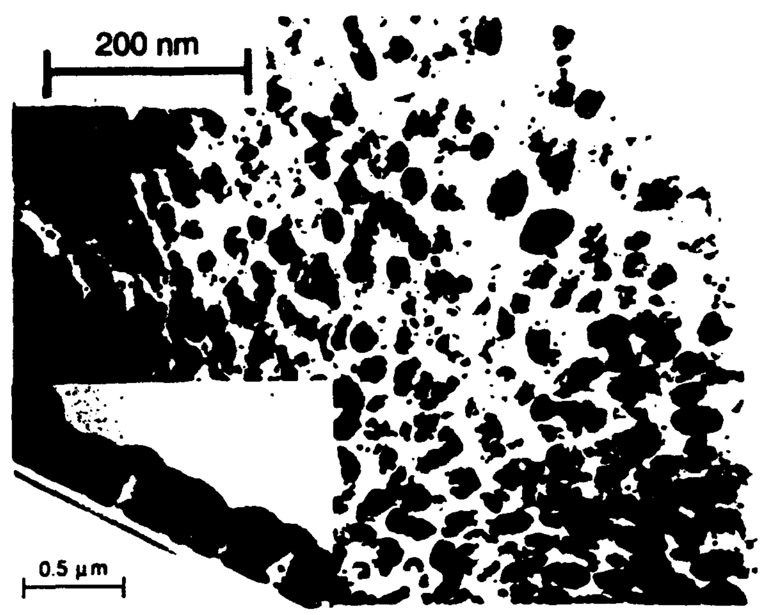

(b) t_h ~ 600 nm (D ~ 1 x 10^{17} ions/cm^2)

Fig. 3 Cross sectional TEM micrograph of film grown to a thickness of 600 nm with a high current density (7 μA/cm^2) at room temperature. The dose was 10^{17} ions/cm^2. The inset shows a larger portion of the film at a coarser scale. The film consists of grains of gold in a carbon background.

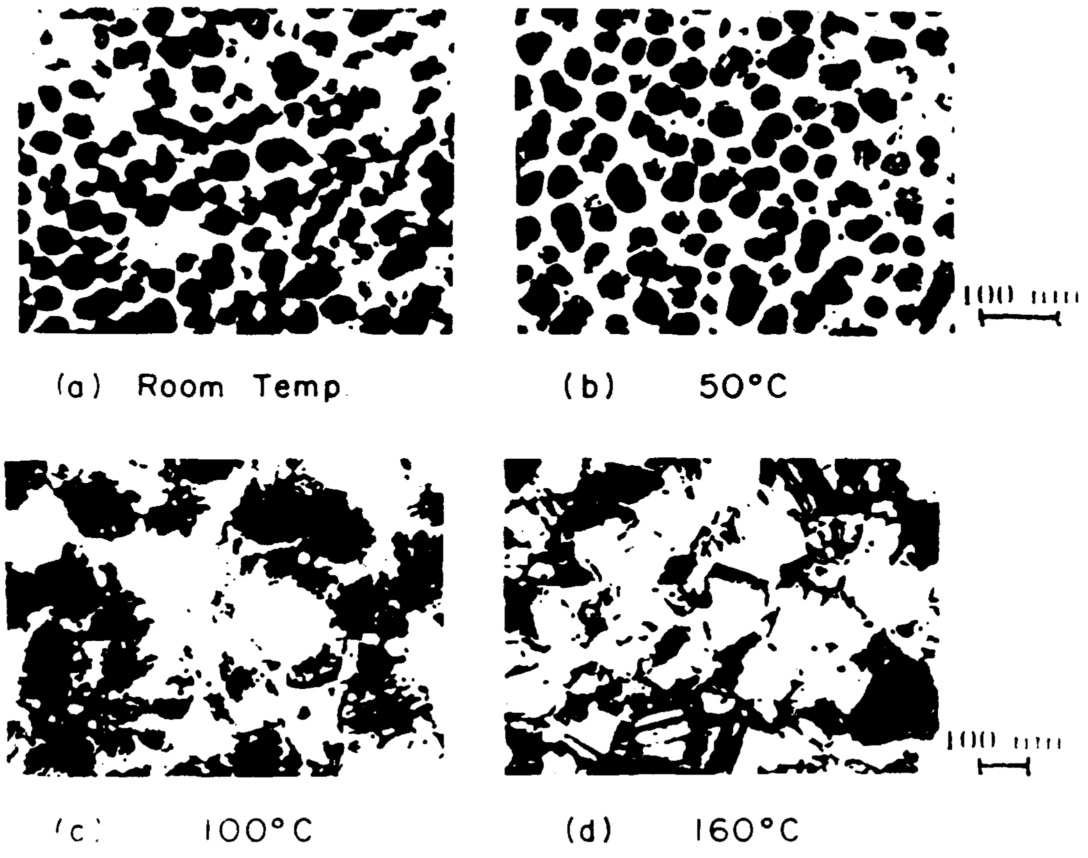

Fig. 4 Plan view transmission electron micrographs of 4 films grown at 4 substrate temperatures. 70 keV Ar^+ ions were used at a current density of 0.7A/cm^2 with a total dose of 10^{16} ions/cm^2. The nominal thickness of the film is ~ 10 nm. For room temperature growth (a) and 50°C growth (b) the film is seen to consist of a layer of rounded gold islands. At 100°C (c) and 160° (d). The film has the normal polycrystalline structure, seen in evaporated films.

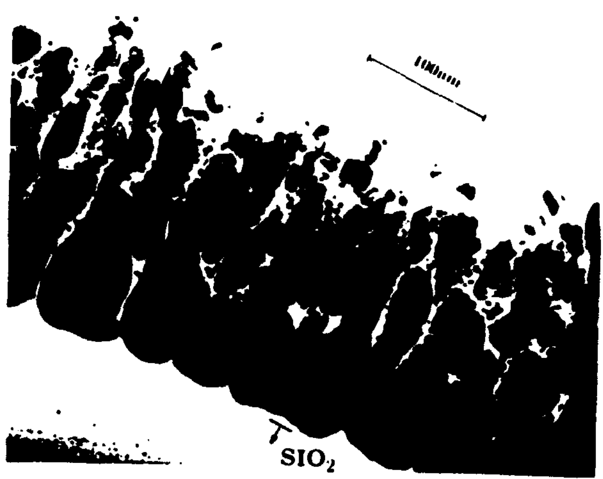

Fig. 5 Cross sectional TEM micrograph of a film grown at room temperature and low ($0.7 A/cm^2$) current density with 50 keV Ar^+ ions. This shows how the film depicted in Fig. 4 (a) grows as its thickness is increased, i.e. the rounded islands of gold become columns.

Focused Ion Beam Induced Deposition of Copper

Anthony D. Della Ratta, John Melngailis, and Carl V. Thompson

Research Laboratory of Electronics

Massachusetts Institute of Technology, Cambridge, MA 02139

Abstract

As the dimensions of integrated circuits decrease into the submicron range, the problems of circuit delay and interconnect reliability become more urgent. Due to its low resistivity (1.67 $\mu\Omega$-cm) and high electromigration resistance, copper has received attention as a candidate metal for the integrated circuits of the future. In addition, the focused ion beam, with its capability for milling and deposition at linewidths of 0.1 μm or below, has proved useful as a tool for integrated circuit "microsurgery". Focused ion beam induced deposition of copper from a novel organometallic precursor compound, Cu(hfac) TMVS, has been achieved using 25 to 35 keV Ga^+ ions from a liquid metal ion source. Submicron copper lines deposited at room temperature from this precursor exhibit resistivities as low as 50 $\mu\Omega$-cm; a sharp drop in these values is noted for deposition above 67°C, and deposition on a substrate heated above about 100°C yields resistivities near those of pure bulk copper. Composition analysis by Auger Electron Spectroscopy shows the high temperature deposition to be nearly pure copper. Deposition yields of 14 copper atoms per incident Ga^+ ion have been obtained on both silicon and silicon dioxide substrates, with growth rates of up to 2.2 nm per second at an average ion current density of 200 $\mu A/cm^2$. The quality and microstructure of the de-

To be published J. Vac. Sci. Technol. B 11, Nov/Dec (1993)
(Presented at EIPB, San Diego, CA June 1993)

posited film seems to be inextricably tied to the ability of the carbon-containing byproduct molecules to desorb from the growing film. For instance, high temperature deposition results in a low resistivity film with few impurities, most likely because this condition allows greater byproduct desorption. Under the proper conditions, this particular precursor compound shows great promise for use in the focused ion beam induced deposition of low resistivity, submicron interconnects on integrated circuits for repair processes.

I. Introduction

The focused ion beam, or FIB, is capable of carrying out repair operations such as milling and deposition on integrated circuits to the linewidths and tolerances required at this small scale. Milling is used to cut conductors and ion induced deposition is used to make connections.[1] In some cases redeposition of milled material can also be used to make connections.[2] During deposition, an organometallic gas is adsorbed on the surface of the IC and the FIB is used to decompose the molecules into metal, which deposits, and volatile, carbon-containing byproduct molecules which must desorb upon decomposition of the molecule to create a pure film. Using both of these techniques, it is possible to salvage a microelectronic circuit which is faulty due to a misplaced or missing interconnect by introducing open circuits and jumpers at strategic locations. It is the latter process, FIB induced deposition, which will be addressed in this paper.[3,4]

Already, deposition has been achieved for a variety of metals, including W, Au, Pt, Cr, Ta and Al, using this technique.[5-14] For example, focused ion beam induced deposition of Au from a DMG(hfac) precursor at room temperature resulted in a film containing a large

fraction of carbon, with a microstructure consisting of gold islands in a carbon matrix and resistivities on the order of polysilicon.[10,12] Heating of the substrate during deposition caused the gold content to increase and resistivity to drop markedly.[11] Clearly, the enhanced ability of the byproduct molecules to escape the growing film at higher temperatures improved the quality of the resultant deposit.

II. Experimental

Two focused ion beam machines were used during the course of this work, and both can be illustrated schematically by figure 1. In one case, 35 keV Ga^+ ions from an IBT Dubilier focused ion beam column (estimated beam spot size approximately 0.2 μm) mounted on a custom made UHV work chamber were used, and in the second 25 keV Ga^+ from an FEI 500D Focused Ion Beam Milling System (estimated spot size < 0.1 μm at 16 pA beam current) were employed. The instantaneous ion current densities was estimated to be on the order of 1 A/cm^2. The ion columns and work chambers are differentially pumped in these machines. In both cases a capillary tube with a 0.8 mm inner diameter was used to direct vapors of Cu(hfac)TMVS precursor to the point of ion incidence. Depositions were carried out on both silicon and silicon dioxide substrates. The average current density of the gallium ions (defined as the beam current divided by the scan area) was varied from 5 to 250 $\mu A/cm^2$ by changing the area or line length scanned by the beam; in the case of the FEI machine, the ion beam dwell time could be varied independently of the scanned area. The dwell time used in every experiment was 100 ns, and the pixels overlapped by 50 % on the sample. The sample temperature during deposition could be varied using a resistively heated stage.

Resistivity was measured by depositing a line of copper across a previously fabricated four-point probe pattern on SiO_2. Auger analysis was carried out on the deposits to determine the relative concentrations of metal and impurity, and transmission electron microscopy (TEM) samples were prepared by depositing on 0.1 μm thick silicon nitride membranes.

The copper precursor Cu(hfac)TMVS is also known as Copper(+1)hexafluoroacetylacetonate trimethylvinylsilane, and is used primarily for selective copper chemical vapor deposition.[15,16] The trimethylvinylsilane group acts to stabilize the Cu(+1) oxidation state at room temperature. The normal CVD disproportionation reaction at substrate temperatures above 120°C is:

$$2Cu(hfac)TMVS(g) = Cu(s) + Cu(hfac)_2 + 2TMVS(g)$$

and occurs preferentially on conductors. It is a straw yellow or yellow-green, low viscosity liquid at room temperature, with a vapor pressure of approximately 0.2 torr. For these experiments, the liquid was maintained at room temperature in a glass flask outside the work chamber; during depositions the liquid was allowed to evaporate through the capillary tube to vacuum. The pressure of the precursor at the point of ion incidence was measured by allowing the gas to fill a stagnation tube positioned under the capillary mouth and connected to a capacitance manometer.

III. Results and Discussion

SEM micrographs of lines deposited using this compound appear in figure 2 (a) and (b).

A linewidth of 0.25 μm has been achieved, and an aspect ratio of 5.4 to 1 is evident in figure 2(b). The lines were deposited at room temperature by scanning a 25 keV, 16 pA beam over a 50 μm length at a local Cu(hfac)TMVS precursor pressure of 1.5 mtorr and an ion beam dwell time of 100 ns. Data for the growth rate of this compound appears in figure 2 (c) and (d). The maximum yield of this precursor, assuming the deposit has the density of pure bulk copper (8.4×10^{22} atoms/cm^3), is found to be 28 atoms/ion. The yield is found to decrease with increasing average ion current density as expected due to the depletion of the adsorbate on the substrate surface. Viewed in terms of growth rate in figure 2(d), the compound is found to grow at a maximum rate of 2.2 nm/s at an average current density of 250 μA/cm^2.

The resistivity data measured by depositing a line across four contacts in figure 3 shows an increase in the resistivity with increasing current density. The lowest room temperature value, obtained at a current density of 20 μA/cm^2, was 50 $\mu\Omega$-cm, increasing to over 500 $\mu\Omega$-cm at higher current densities. The most likely explanation for this is that the film is growing too rapidly for the byproduct molecules to escape readily, although it is possible that a microstructural effect may also be responsible for this trend. This is strikingly different from the cases of platinum[13] and gold[10] deposition, which resulted in low resistivity depositions at high ion current density (low yield) conditions. A marked decrease in film resistivity noted at high deposition temperatures is illustrated in 3(b). The value of resistivity at the highest temperature (110°C) is 2 $\mu\Omega$-cm, which is within experimental error of that of pure copper (1.7 $\mu\Omega$-cm.)

TEM investigation of 50-100 nm thick copper films as a function of deposition temperature is illustrated in figure 4 and correlates with the drop in resistivity with increasing deposition temperature. The low temperature films apparently consist of small, 20 nm islands of copper surrounded by a low Z matrix, presumably mostly carbon. At higher temperatures the islands contact each other. At 100°C the film appears to be a polycrystalline copper film. TEM micrographs of samples deposited at various average ion current densities at room temperature appear in figure 5. Some growth of the copper islands is observed at higher current densities, but the films do not become continuous, and so the resistivity remains relatively high.

Results of Auger electron spectroscopy composition analysis of the films appears in figure 6. The two main components of the film are copper and carbon, with gallium and oxygen appearing only in negligible amounts. In a typical room temperature deposit, the film appears to be consist roughly of a 1:1 atomic ratio of copper to carbon. Using this compositional data, it is possible to calculate a maximum copper atom yield of 14 copper atoms/gallium ion using this precursor compound. At higher temperatures, the copper content increases dramatically until at 100°C, the film is almost pure copper. Figure 6(b) shows that the carbon to copper ratio does not change as a function of average ion current density.

IV. Conclusions

We have deposited quarter micron copper interconnects using a 25 to 35 keV Ga^+ focused ion beam. The lowest resistivity at room temperature attained has been 50 $\mu\Omega$-cm. Heating of the substrate during ion beam writing results in depositions with resistivities as low

as 2 $\mu\Omega$-cm. Yields as high as 14 Cu atoms/Ga^+ ion and growth rates as high as 2.2 nm/s have been obtained. TEM analysis showed a drastic change in the film morphology as a function of deposition temperature, from a discontinuous island structure at room temperature to a continuous polycrystalline metal film at a temperature of 100°C. Under film growth conditions which promoted the desorption of carbon-containing byproducts (e.g. high temperature), the carbon content and resistivity were found to be decreased.

V. Acknowledgments

We would like to express our appreciation to J.A.T. Norman of Schumacher in Carlsbad, Calif. for supplying us with the Cu(hfac)TMVS compound. This particular compound was suggested for use with the FIB by K.F. Jensen at MIT. We would also like to thank X. Xu for helpful discussions and instruction in the use of the IBT FIB machine, and E.L. Shaw of the Surface Analysis Facility at MIT for the Auger composition analysis. This work was supported by the Army Research Office under contract number DAAL 93-90-G-0223 and by the National Science Foundation under grant number DMR 9202633.

[1]The possibility of using focused ion beam induced deposition to repair integrated circuits was recognized early. See K. Gamo, N. Takakura, N. Samoto, R. Shimizu, and S. Namba, Jpn. J. Appl. Phys. **23**, L293 (1984). For recent examples see: D.K. Stewart, L.A. Stern, and J.C. Morgan, SPIE **1089**, 18 (1989), and T. Tao, W. Wilkinson, and J. Melngailis, J. Vac. Sci. Technol. B **9**, 162 (1989).

[2]C.R. Musil, J.L. Bartelt, and J. Melngailis, IEEE Elect. Dev. Lett. Vol. EDL-7, No. 5,

[2]C.R. Musil, J.L. Bartelt, and J. Melngailis, IEEE Elect. Dev. Lett. Vol. EDL-7, No. 5, 285 (1986).

[3]K. Gamo and S. Namba, Microelectron. Eng. **11**, 403 (1990).

[4]J. Melngailis, Proc. SPIE **1465**, 36 (1991).

[5]K. Gamo, D. Takehara, Y. Hamamura, M. Tomita, and S. Namba, Microel. Eng. **5**, 163 (1986).

[6]Z. Xu, T. Kosugi, K. Gamo, and S. Namba, Riken Conference, March 1989.

[7]Z. Xu, T. Kosugi, K. Gamo, and S. Namba, J. Vac. Sci. Technol. B **7**, 1959 (1989).

[8] M.E. Gross, L.R. Harriott, and R.L. Opila, J. Appl. Phys. **68**, 4820 (1990).

[9] G.M. Shedd, H. Lezec, A.D. Dubner, and J. Melngailis, Appl. Phys. Lett. **49**, 1584 (1986).

[10] P.G. Blauner, J.S. Ro, Y. Butt, and J. Melngailis, J. Vac. Sci. Technol. B **7**, 609 (1989)

[11] P.G. Blauner, J.S. Ro, Y. Butt, C.V. Thompson, and J. Melngailis, J. Vac. Sci. Technol. B **7**, 1816 (1989).

[12] P.G. Blauner, J.S. Ro, Y. Butt, C.V. Thompson, and J. Melngailis, Materials Research Society Proceedings (MRS, Pittsburgh, 1989), Vol. 129.

[13] T. Tao, J.S. Ro, J. Melngailis, Z. Xue, and D. Kaesz, J. Vac. Sci. Technol. **8**, 1826 (1990).

[14]J. Puretz and L.W. Swanson, J. Vac. Sci. Technol. B **10**, 2695 (1992).

[15] J.A.T. Norman, B.A. Muratore, P.N. Dyer, D.A. Roberts, A.K. Hochberg, and L.H. Dubois, presented at E-MRS Meeting, Strasbourg, France, June 1992.

[16] J.A.T. Norman, B.A. Muratore, P.N. Dyer, D.A. Roberts, and A.K. Hochberg, J. de Physique, IV, C2-271 (1991).

Figure Captions

Figure 1. Schematic of a typical focused ion beam apparatus. The FIB column and the work chamber are separated by a differential pumping aperture. The organometallic gas is directed to the sample substrate by a 0.8 mm I.D. capillary tube, and deposition occurs where the ion beam decomposes the adsorbed gas molecules on the sample surface.

Figure 2. Appearance and growth rate characteristics of copper depositions. Copper lines of 50 μm length are deposited with a 25 keV Ga^+ ion beam at a current of 16 pA and a local gas pressure of 1.5 mtorr, at an ion beam dwell time of 100 ns: (a) A linewidth of 0.25 μm is evident, and in (b) an aspect ratio of 5.4 to 1 is apparent. Growth rate data for depositions using 35 keV Ga^+ at a local gas pressure of 1.5 mtorr and an ion beam dwell time of 100ns: (c) Yield in atoms per incident Ga^+ ion, assuming the deposit has the density of pure copper (8.4 X 10^{22} atoms/cm^3) as a function of the average ion current density, and (d) growth rate in angstroms/second as a function of the average ion current density. One can expect an error of approximately +/- 20 % in the yield and growth rate measurements.

Figure 3. Resistivity data of copper deposited using a 35 keV Ga^+ beam, as a function of (a) average ion current density, at room temperature, and (b) as a function of substrate temperature during deposition, at an average ion current density of 20 $\mu A/cm^2$. Experiments were carried out with a beam of 35 keV Ga^+ ions at varying currents, scanned in a line 300 μm in length. Both experiments were carried out at a local precursor pressure of 1.5 mtorr and an ion beam dwell time of 100 ns. An error margin of approximately +/- 20 % can be

expected in the resistivity data.

Figure 4. TEM micrographs of 50-100 nm thick copper films deposited at various substrate temperatures using 25 keV Ga^+ ions at an average current density of 20 $\mu A/cm^2$, a local precursor gas pressure of 1.5 mtorr, and a ion beam dwell time of 100 ns. (a) 25°C (b) 40°C (c) 67°C (d) 80°C (e) 100°C. Experiments were carried out with a 25 keV Ga^+ ion beam at 60 pA into a scanned area of 10 by 30 μm^2.

Figure 5. TEM micrographs of 50-100 nm thick copper films deposited at various average ion current densities using 25 keV Ga^+ ions at a room temperature, at a local precursor gas pressure of 1.5 mtorr and an ion beam dwell time of 100 ns. (a) 10 $\mu A/cm^2$ (b) 50 $\mu A/cm^2$ (c) 200 $\mu A/cm^2$. Experiments were carried out with a 25 keV Ga^+ ion beam at 60 pA scanned into 600 μm^2, 120 μm^2, and 30 μm^2 areas, respectively.

Figure 6. Auger composition data for films deposited using 25 keV Ga^+ ions at a local precursor gas pressure of 1.5 mtorr and an ion beam dwell time of 100 ns (a) at various substrate temperatures at an average ion current density of 20 $\mu A/cm^2$ and (b) at various ion current densities at room temperature. The fractions of Ga, O, and other elements were negligible. One can expect an error of from 10-30 at. % on uncalibrated Auger data such as this.

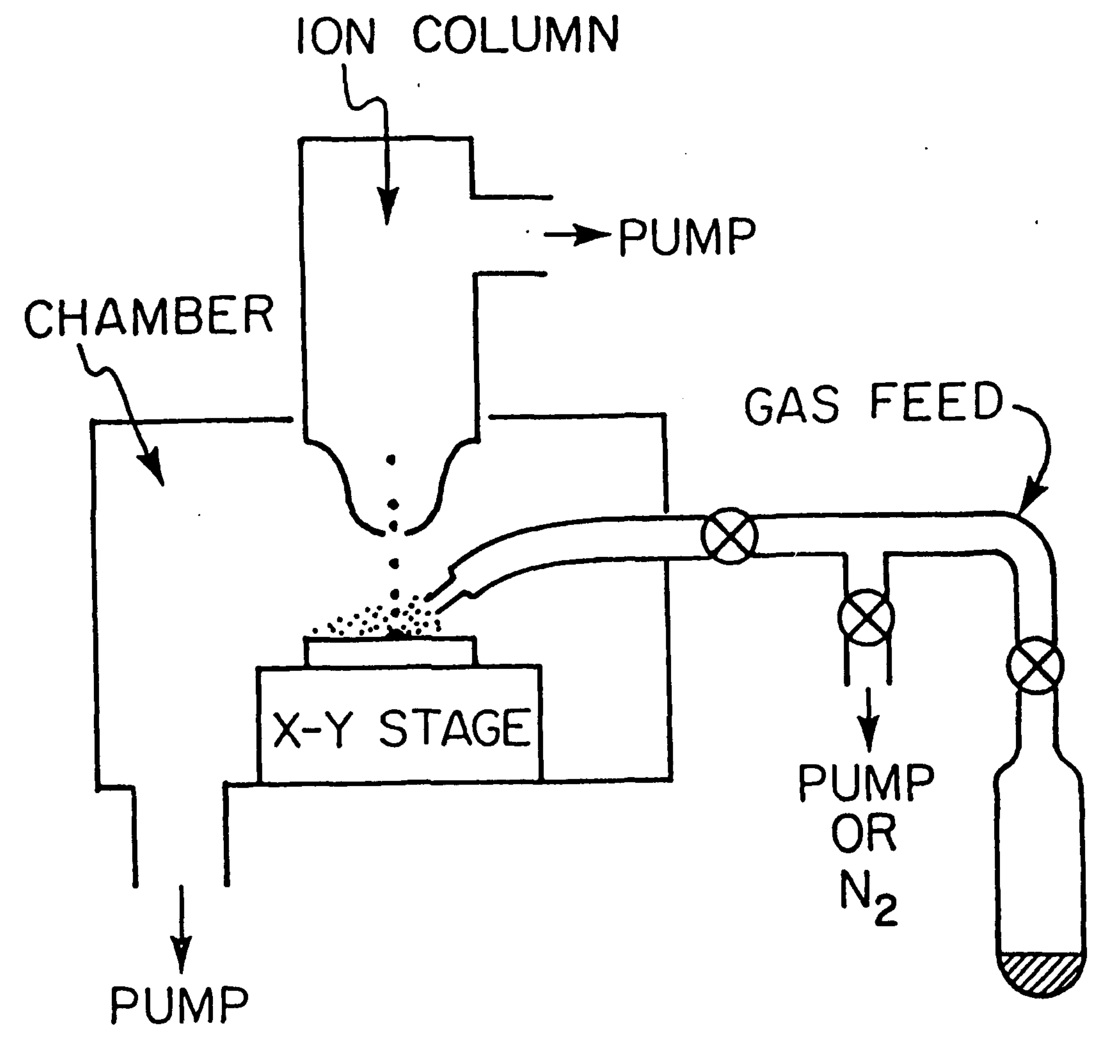
ION COLUMN
PUMP
CHAMBER
GAS FEED
X-Y STAGE
PUMP
OR
N_2
PUMP

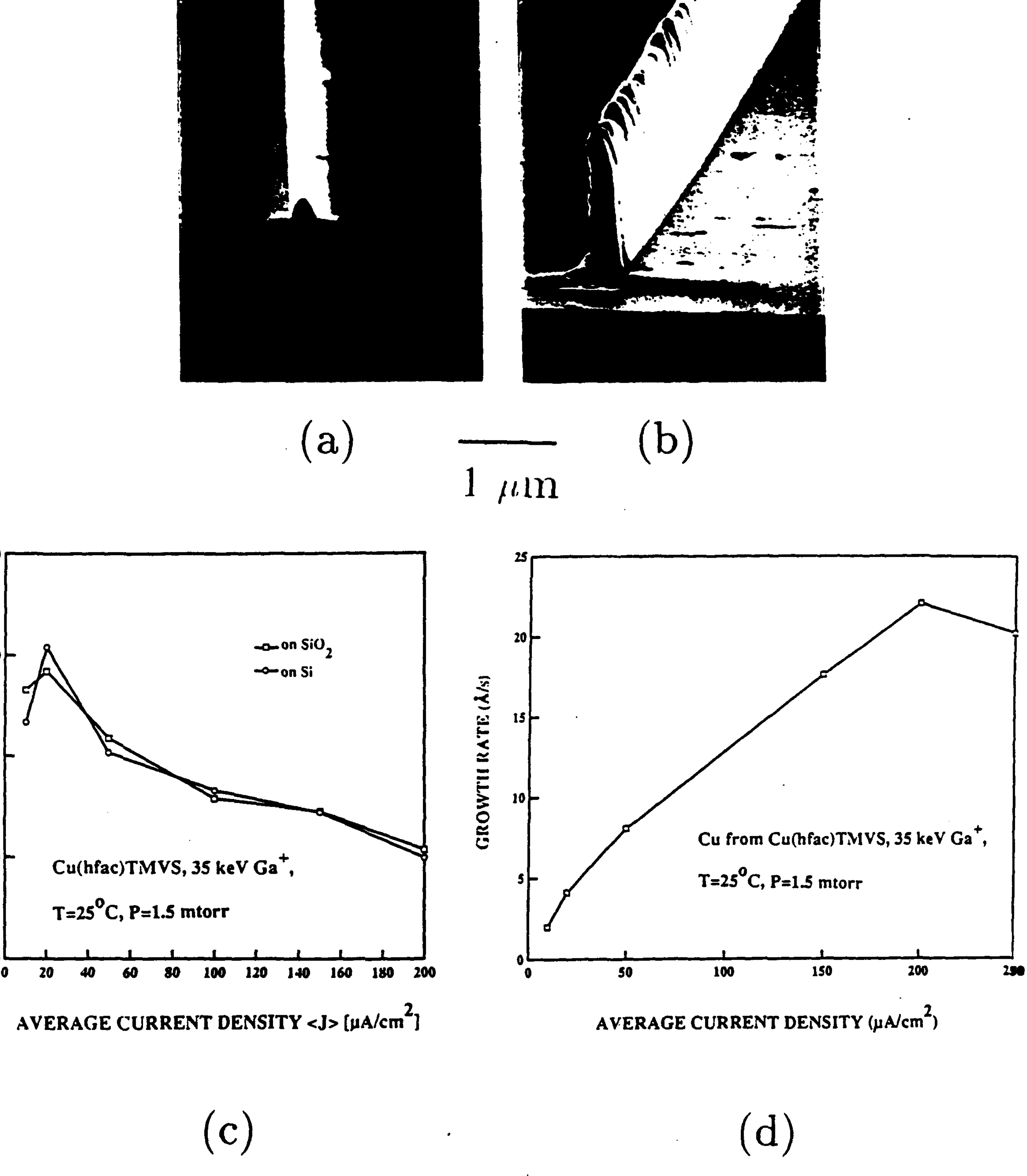
(a)
(b)
1 μm
on SiO2
on Si
Cu(hfac)TMVS, 35 keV Ga+,
T=25°C, P=1.5 mtorr
0
20
40
60
80
100
120
140
160
180
200
AVERAGE CURRENT DENSITY <J> [μA/cm2]
(c)
GROWTH RATE (Å/s)
25
20
15
10
5
0
50
100
150
200
250
Cu from Cu(hfac)TMVS, 35 keV Ga+,
T=25°C, P=1.5 mtorr
AVERAGE CURRENT DENSITY (μA/cm2)
(d)

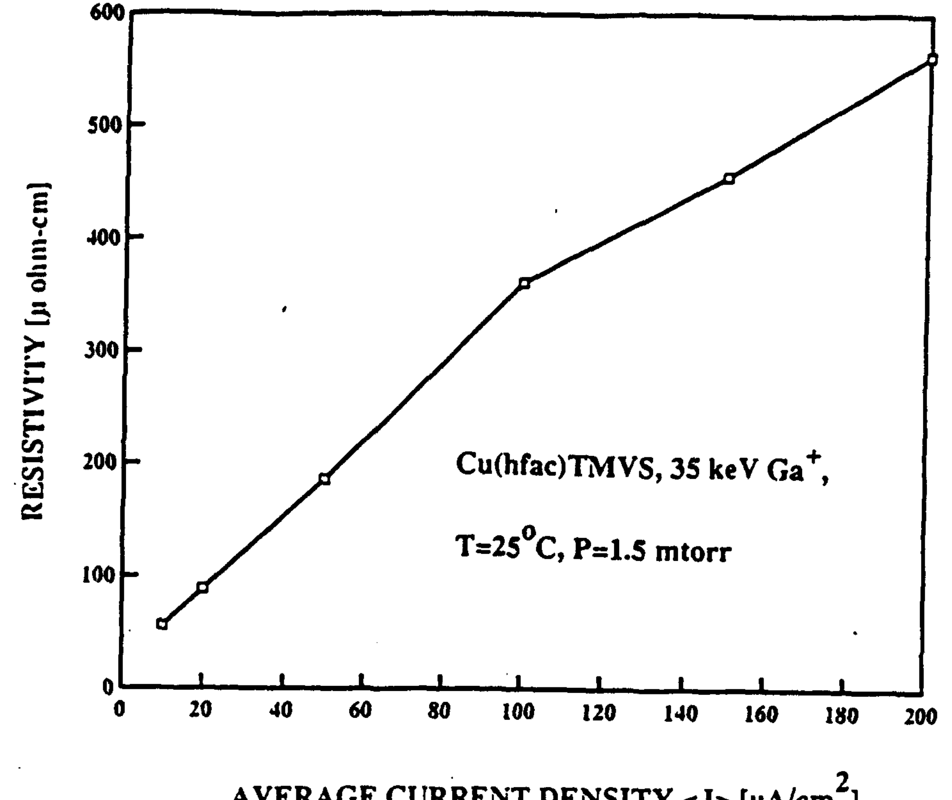

(a)

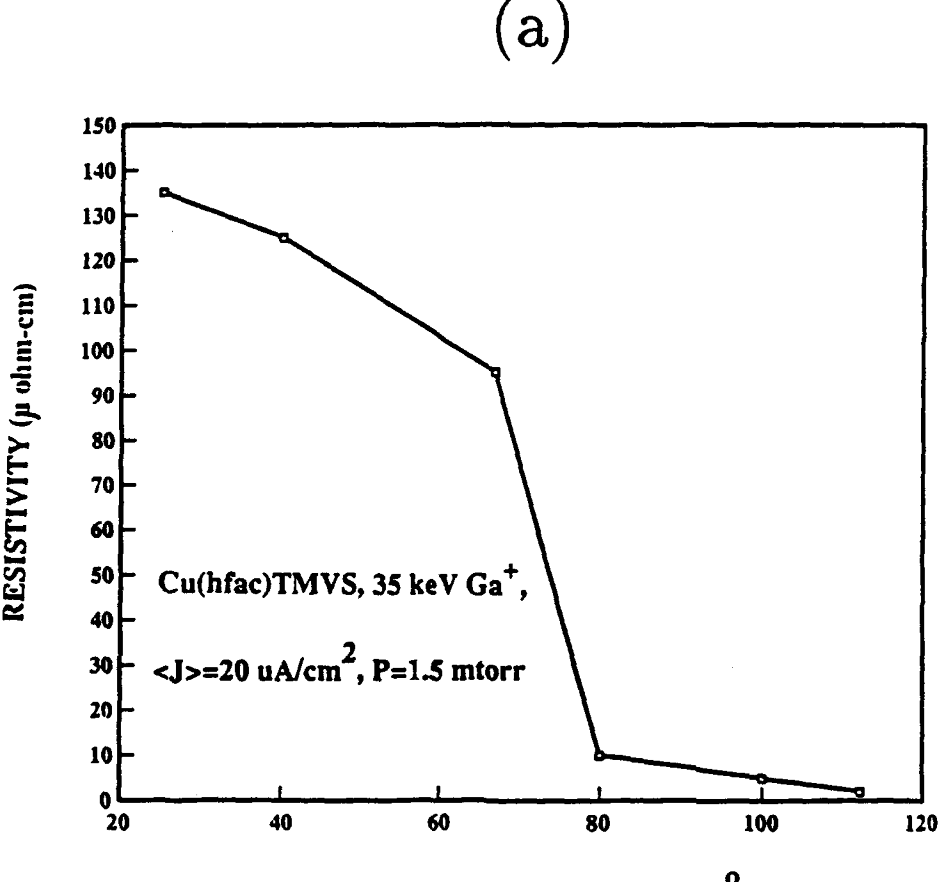

(b)

EM--Effect of Temperature

100 nm thick, <J>=20 uA/cm^2,

P=1.5 mtorr

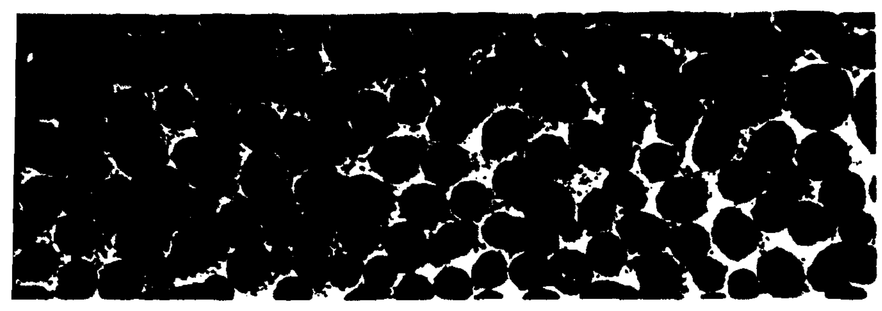

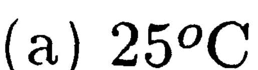

(a) 25°C

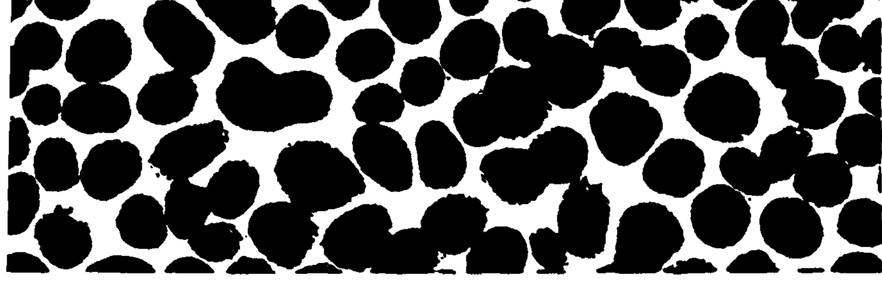

(b) 40°C

(c) 67°C

25 nm

(d) 80°C

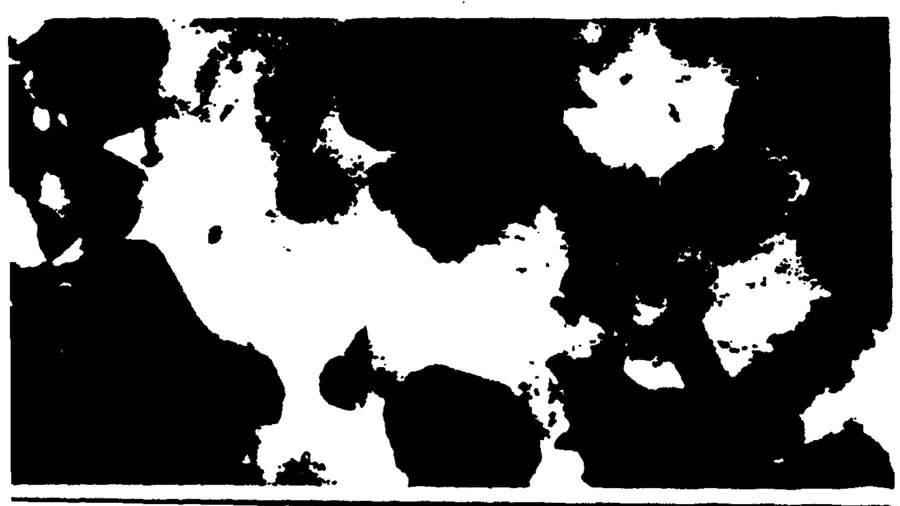

(e) 100°C

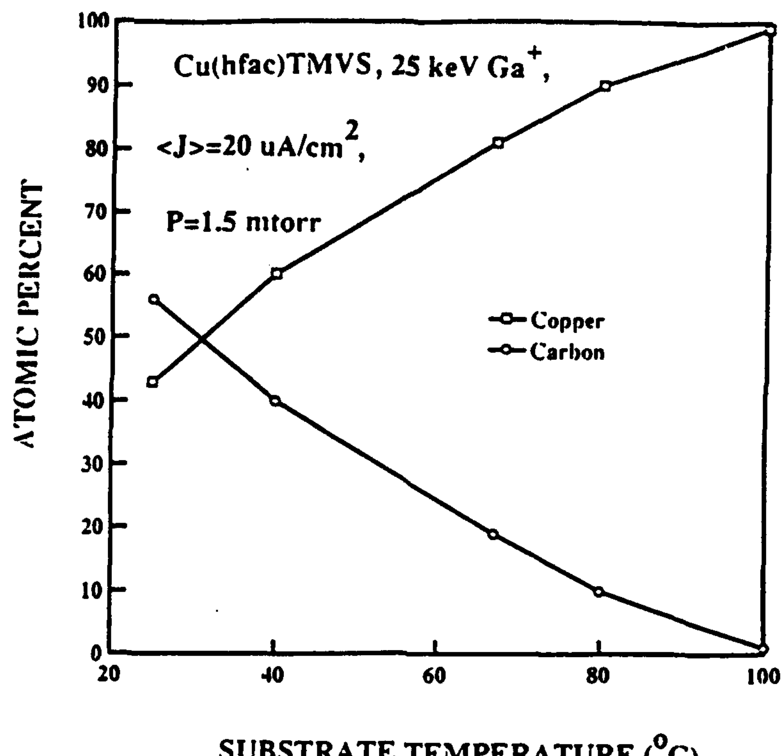

(a)

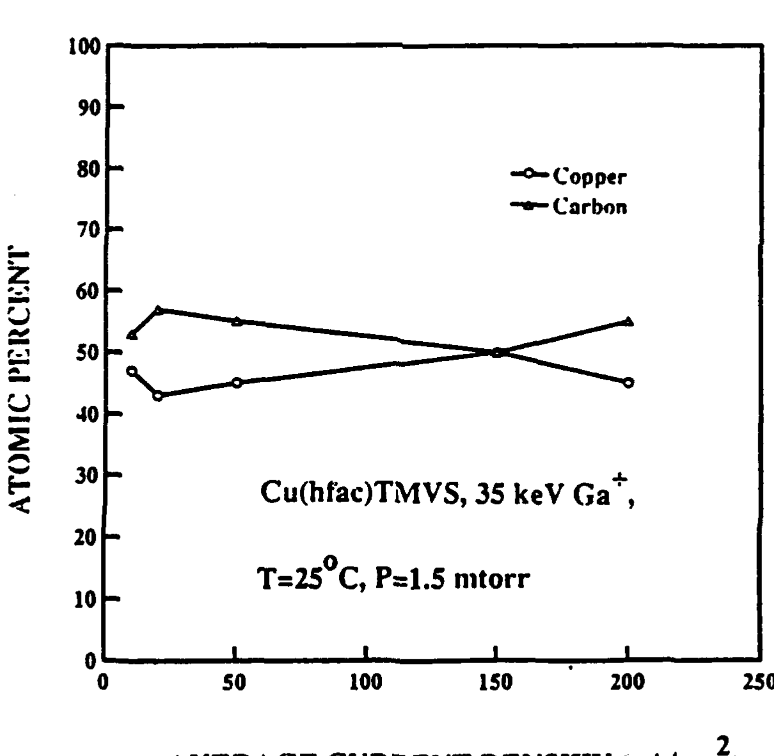

(b)

TEM--Effect of Average Current Density

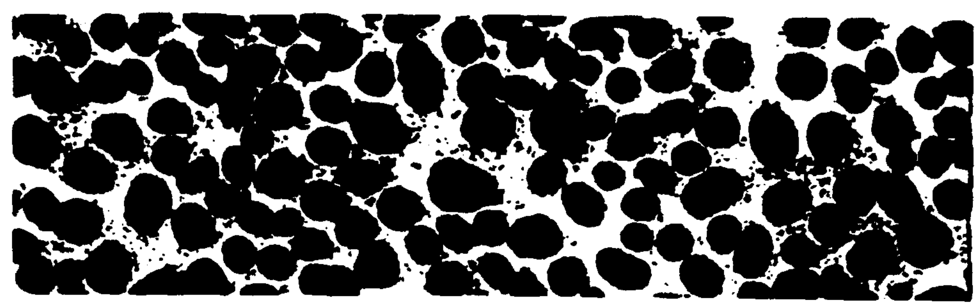

(a) 10 $\mu A/cm^2$

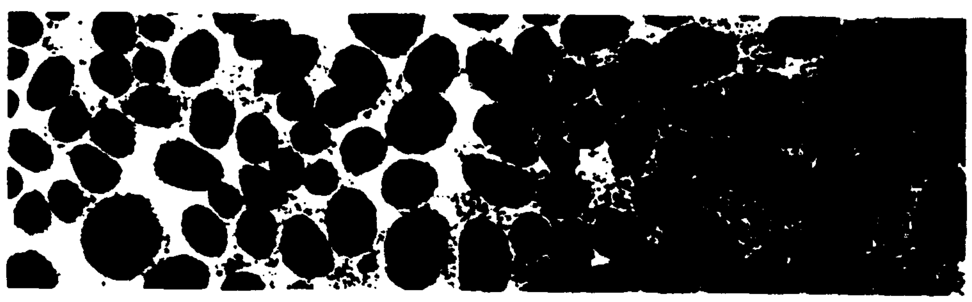

(b) 50 $\mu A/cm^2$

(c) 200 $\mu A/cm^2$

25 nm

100 nm thick, T=25°C, P=1.5 mtorr